

<sup>1</sup> Study of the multi-strange resonance  $\Xi(1530)^0$  production  
<sup>2</sup> with ALICE at the LHC energies

<sup>3</sup> Jihye Song

## **4** Contents

<b>5</b>	<b>List of Figures</b>	<b>4</b>
<b>6</b>	<b>List of Tables</b>	<b>8</b>
<b>7</b>	<b>1 The physics of relativistic heavy-ion collisions</b>	<b>9</b>
8	1.1 Standard model . . . . .	9
9	1.2 QCD and Quark-Gluon plasma . . . . .	10
10	1.3 Heavy Ion Collisions . . . . .	16
<b>11</b>	<b>2 Theoretical models</b>	<b>19</b>
12	2.1 Statistical-Thermal model . . . . .	19
13	2.1.1 Calculations . . . . .	21
14	2.1.2 Results and comparison with data . . . . .	23
15	2.2 EPOS, UrQMD . . . . .	25
<b>16</b>	<b>3 Production of hyperon resonance</b>	<b>27</b>
17	3.1 Strange quark and hyperons . . . . .	29
18	3.2 Resonance production . . . . .	31
<b>19</b>	<b>4 A Large Ion Collider Experiment at the LHC</b>	<b>33</b>
20	4.1 The Large Hadron Collider . . . . .	33
21	4.2 The ALICE project . . . . .	36
22	4.2.1 ALICE detector . . . . .	36
23	4.2.2 Data Acquisition (DAQ) and trigger system . . . . .	47
24	4.2.3 ALICE offline software frame work . . . . .	49
<b>25</b>	<b>5 Measurement of <math>\Xi(1530)^0</math> production in p-Pb and Pb-Pb</b>	<b>51</b>
26	5.1 $\Xi(1530)^0$ -reconstruction . . . . .	51
27	5.1.1 Data sample and event selection . . . . .	51
28	5.1.2 Track and topological selection . . . . .	55
29	5.1.3 Particle identification . . . . .	58
30	5.1.4 Signal extraction . . . . .	61
31	5.2 Efficiency correction . . . . .	70
32	5.3 Corrected $p_T$ -spectra . . . . .	73
33	5.4 Systematic uncertainties . . . . .	75
34	5.5 $\Xi(1530)^0$ transverse momentum spectra . . . . .	80
<b>35</b>	<b>6 Further results and discussion</b>	<b>83</b>
36	6.1 Mean transverse momentum . . . . .	83
37	6.2 Particle yield ratios . . . . .	87

38	6.2.1 Integrated yield ratios of excited to ground-state hadrons . . . . .	87
39	6.3 Integrated yield ratios to pion . . . . .	90
40	<b>References</b>	<b>93</b>

41 **List of Figures**

42 1	QCD coupling constant as a function of momentum transfer. Experimental 43 data and also theoretical prediction are presented. [1] . . . . .	13
44 2	QCD phase diagram in T as function of $\mu_B$ . The chemical freeze out points 45 are determined from thermal models fit to heavy ion data at SIS, AGS, and 46 SPS energies. ( <a href="http://na49info.web.cern.ch/na49info/Public/Press/findings.html">http://na49info.web.cern.ch/na49info/Public/Press/findings.html</a> )	15
47 3	The time evolution of a high energy heavy ion collision. [2] . . . . .	16
48 4	Hydrodynamic evolution of a heavy ion collision with and without the for- 49 mation of a QGP. . . . .	18
50 5	Grand canonical thermal fit of 0-10% central Pb-Pb collisions, with 3 models 51 (THERMUS, GSI, SHARE). . . . .	19
52 6	Ratio of baryonic and mesonic resonances over their stable partner as a 53 function of temperature. . . . .	24
54 7	Ratio of resonances over their stable partner as a function of $\sqrt(s)$ . . . . .	25
55 8	The $J^P = 1/2^+$ ground state baryon octet . . . . .	28
56 9	The $J^P = 3/2^+$ baryon decuplet . . . . .	28
57 10	Integrated yield relative to small system (pp or p-Be) as a function of the 58 mean number of participants $\langle N_{part} \rangle$ in the rapidity range $ y  < 0.5$ . The 59 results from ALICE are presented as full symbols, RHIC and SPS data 60 are shown as open symbols. Boxes on the dashed line at unity represent 61 statistical and systematic uncertainties on the pp or p-Be reference. . . . .	30
62 11	Hadronic phase . . . . .	31
63 12	The CERN accelerator complex [3] . . . . .	34
64 13	The ALICE detector . . . . .	38
65 14	Schematic view of the ITS [4] . . . . .	39
66 15	Track impact parameter resolution ( $r\phi$ ) in the transverse plane as function 67 of $p_T$ for charged particle . . . . .	40
68 16	Schematic view of the TPC . . . . .	41
69 17	Specific energy loss ( $dE/dx$ ) in the TPC as a function of momentum in Pb– 70 Pb collisions at $\sqrt{s_{NN}} = 2.76$ TeV. The lines show the parameterizations of 71 the expected mean energy loss. . . . .	42
72 18	Sketch of events collisions at (8.3 ns, 14.3 ns) is shown in left, background 73 from Beam 1 at (-14.3 ns, -8.3 ns) in in middel and background from Beam 74 2 at (14.3 ns, 8.3 ns) is in right. . . . .	43
75 19	Correlation between the sum (y-axis) and difference (x-axis) of signal times 76 in V0A and V0C. The signals in center come from beam-beam interactions, 77 the signal in left is background from Beam1 and background from Beam2 is 78 shown in right hand. . . . .	44
79 20	Sum of V0A and V0C amplitude distribution in top and V0A amplitude 80 distribution in bottom. . . . .	46

81	21	The overall architecture of the ALICE DAQ and the interface to the HLT system. . . . .	47
82	22	Schematic view of the AliRoot framework . . . . .	50
83	23	Distribution of vertex-z position from the accepted events in p–Pb collision(Left) and in Pb–Pb collisions(Right). The red dashed line indicates vertex cut . . . . .	53
84	24	Multiplicity distribution of accepted events in p–Pb collision in percentile. The each color presents the four intervals for the analysis. . . . .	53
85	25	Centrality distribution of three different trigger classes. . . . .	54
86	26	Sketch of the decay modes for $\Xi^{*0}$ and depiction of the track and topological selection criteria. . . . .	56
87	27	TPC $dE/dx$ as function of transverse momentum in p–Pb collisions for total (Left) and selected first emitted $\pi$ in $3\sigma$ (Right) . . . . .	58
88	28	TPC $dE/dx$ as function of transverse momentum in p–Pb collisions for total (Left) and selected second emitted $\pi$ in $3\sigma$ (bottom) . . . . .	58
89	29	TPC $dE/dx$ as function of transverse momentum in p–Pb collisions for total (Left) and selected last emitted $\pi$ in $3\sigma$ (bottom) . . . . .	59
90	30	TPC $dE/dx$ as function of transverse momentum in p–Pb collisions for total (Left) and selected proton in $3\sigma$ (bottom) . . . . .	59
91	31	TPC $dE/dx$ as function of transverse momentum in Pb–Pb collisions for total (Left) and selected first emitted $\pi$ in $3\sigma$ (Right) . . . . .	59
92	32	TPC $dE/dx$ as function of transverse momentum in Pb–Pb collisions for total (Left) and selected second emitted $\pi$ in $3\sigma$ (Right) . . . . .	60
93	33	TPC $dE/dx$ as function of transverse momentum in Pb–Pb collisions for total (Left) and selected last emitted $\pi$ in $3\sigma$ (Right) . . . . .	60
94	34	TPC $dE/dx$ as function of transverse momentum in Pb–Pb collisions for total (Left) and selected proton in $3\sigma$ (Right) . . . . .	61
95	35	The $\Xi^\mp\pi^\pm$ invariant mass distribution (Same-event pairs) in $1.8 < p_T < 2.2 \text{ GeV}/c$ and for the multiplicity class 20-40%. The background shape, using pairs from different events (Mixed-event background), is normalised to the counts in $1.49 < M_{\Xi\pi} < 1.51 \text{ GeV}/c^2$ and $1.56 < M_{\Xi\pi} < 1.58 \text{ GeV}/c^2$ . . . . .	62
96	36	The $\Xi^\mp\pi^\pm$ invariant mass distribution (Same-event pairs) in $3.0 < p_T < 3.5 \text{ GeV}/c$ and for the centrality class 0-10%. The background shape, using pairs from different events (Mixed-event background), is normalised to the counts in $1.49 < M_{\Xi\pi} < 1.51 \text{ GeV}/c^2$ and $1.56 < M_{\Xi\pi} < 1.58 \text{ GeV}/c^2$ . . . . .	63
97	37	The invariant mass distribution after subtraction of the mixed-event background in p–Pb collisions. The solid curve represents the combined fit, while the dashed line describes the residual background. . . . .	64
98	38	The invariant mass distribution after subtraction of the mixed-event background in Pb–Pb collisions. The solid curve is the combined fit, while the dashed line represents the residual background. . . . .	65

122	39	$\sigma$ fit parameters as a function of $p_{\text{T}}$ in MB in p–Pb collisions (top) and in Pb–Pb collisions (bottom). . . . .	67
123			
124	40	$\Xi(1530)^0$ mass distribution as a function of $p_{\text{T}}$ in each multiplicity classes in p–Pb collisions (top) and the different centrality classes in Pb–Pb (bottom). The mass values are obtained from fit of the Voigtian function. . . . .	68
125			
126	41	The raw spectra of $\Xi(1530)^0$ obtained by integrating the Voigtian fit function for different multiplicities in p–Pb collisions (top) and Pb–Pb collisions (bottom). Only the statistical error is reported. . . . .	69
127			
128	42	The geometrical acceptance and the reconstruction efficiency ( $A \times \epsilon$ ) for $\Xi(1530)^0$ in $-0.5 < y_{\text{CMS}} < 0$ . Only statistical uncertainties are shown. . . . .	70
129			
130	43	Real corrected $\Xi(1530)^0$ spectrum (black) for the minimum bias with Levy fit (black curve). Also shown are the unweighted generated (blue) and reconstructed (red) $\Xi(1530)^0$ spectra. . . . .	71
131			
132	44	Efficiency as a function of $p_{\text{T}}$ in minimum bias events in p–Pb collisions. . . . .	72
133			
134	45	Efficiency as a function of $p_{\text{T}}$ in different centrality classes in Pb–Pb collisions . . . . .	73
135			
136	46	Corrected $p_{\text{T}}$ -spectra of $\Xi(1530)^0$ in NSD and different multiplicity classes in p–Pb collisions. . . . .	74
137			
138	47	Corrected $p_{\text{T}}$ -spectra of $\Xi(1530)^0$ in different centrality classes in Pb–Pb collisions. . . . .	74
139			
140	48	Summary of the contributions to the systematic uncertainty in minimum bias events in p–Pb collisions. The dashed black line is the sum in quadrature of all the contributions. . . . .	78
141			
142	49	Systematic uncertainties for each multiplicity classes in p–Pb collisions. . . . .	78
143			
144	50	Summary of the contributions to the systematic uncertainty in minimum bias events in Pb–Pb collisions. The dashed black line is the sum in quadrature of all the contributions. . . . .	79
145			
146	51	Systematic uncertainties for each multiplicity classes. . . . .	79
147			
148	52	Corrected yields as function of $p_{\text{T}}$ in NSD events and multiplicity dependent event classes in p–Pb collision system. Statistical uncertainties are presented as bar and systematical uncertainties are plotted as boxes. . . . .	81
149			
150	53	Corrected yields as function of $p_{\text{T}}$ in different centrality classes in Pb–Pb collision system. Statistical uncertainties are presented as bar and systematical uncertainties are plotted as boxes. . . . .	82
151			
152	54	Mean transverse momenta $\langle p_{\text{T}} \rangle$ of $\Lambda$ , $\Xi^-$ , $\Sigma^{*\pm}$ , $\Xi^{*0}$ and $\Omega^-$ in p–Pb collisions at $\sqrt{s_{\text{NN}}} = 5.02$ TeV as a function of mean charged-particle multiplicity density $\langle dN_{\text{ch}}/d\eta_{\text{lab}} \rangle$ , measured in the pseudorapidity range $ \eta_{\text{lab}}  < 0.5$ . The results for $\Lambda$ , $\Xi^-$ and $\Omega^-$ are taken from [5, 6, 7]. Statistical and systematic uncertainties are represented as bars and boxes, respectively. The $\Omega^-$ and $\Xi^-$ points in the 3rd and 4th lowest multiplicity bins are slightly displaced along the abscissa to avoid superposition with the $\Xi(1530)^0$ points. . . . .	84
153			
154			
155			
156			
157			
158			
159			
160			
161			

162	55	Mass dependence of the mean transverse momenta of identified particles for the 0 – 20% V0A multiplicity class and with $-0.5 < y_{\text{CMS}} < 0$ in p– Pb collisions at $\sqrt{s_{\text{NN}}} = 5.02$ TeV [5, 7], and in minimum-bias pp collisions at $\sqrt{s} = 7$ TeV [8] with $ y_{\text{CMS}}  < 0.5$ . Additionally, $D^0$ and $J/\psi$ results are plotted. The $D^0$ and $J/\psi$ were measured in different rapidity ranges: $ y_{\text{CMS}}  < 0.5$ [9] ( $ y_{\text{CMS}}  < 0.9$ [10]) for $D^0$ ( $J/\psi$ ) in pp and $-0.96 < y_{\text{CMS}} <$ $0.04$ [9] ( $-1.37 < y_{\text{CMS}} < 0.43$ [11]) for $D^0$ ( $J/\psi$ ) in p–Pb. Note also that the results for $D^0$ and $J/\psi$ in p–Pb collisions are for the 0–100% multiplicity class. . . . .	85
171	56	Ratio of $\Xi(1530)^0$ to $\Xi^-$ measured in pp [8], p–Pb [5, 7] and Pb–Pb collisions as a function of $\langle dN_{\text{ch}}/d\eta_{\text{lab}} \rangle$ measured at midrapidity. Statistical uncer- tainties (bars) are shown as well as total systematic uncertainties (hollow boxes) and systematic uncertainties uncorrelated across multiplicity (shaded boxes). A few model predictions are also shown as lines at their appropriate abscissa. . . . .	88
177	57	Ratio of $\rho/\pi(\text{Up})$ , $K^*/K$ , $\phi/K(\text{Left bottom})$ and $\Lambda^*/\Lambda$ with system size measured at mid-rapidity. Statistical uncertainties (bars) are shown as well as total systematic uncertainties (hollow boxes) and systematic uncertainties uncorrelated across multiplicity (shaded boxes). A few model predictions are also shown as lines at their appropriate abscissa. . . . .	89
182	58	Ratio of $\Xi(1530)^0$ to $\pi^\pm$ , measured in pp [12] and p–Pb [8] collisions, as a function of the average charged particle density ( $\langle dN_{\text{ch}}/d\eta_{\text{lab}} \rangle$ ) measured at mid-rapidity. Statistical uncertainties (bars) are shown as well as total systematic uncertainties (hollow boxes) and systematic uncertainties uncor- related across multiplicity (shaded boxes). A few model predictions are also shown as lines at their appropriate abscissa. . . . .	91
188	59	Particle yield ratios to pions of strange and multi-strange hadrons normal- ized to the values measured in pp collisions, both in pp and in p–Pb colli- sions. The common systematic uncertainties cancel in the double-ratio. The empty boxes represent the remaining uncorrelated uncertainties. . . . .	92

<sup>192</sup> **List of Tables**

193	1	Components of matter in the Standard Model . . . . .	9
194	2	Fundamental forces . . . . .	10
195	3	Parameters used in the thermal-model calculations. . . . .	20
196	4	Properties of particles used in the ratio calculations. . . . .	22
197	5	Difference of mass ( $\Delta M$ ), baryon number ( $\Delta B$ ), strangeness ( $\Delta S$ ) and charge ( $\Delta Q$ ) of the ratios. . . . .	23
199	6	Quantum numbers and masses associated to the three lighter quarks: u, d and s . . . . .	27
201	7	Lifetime of hadronic resonances . . . . .	29
202	8	Number of analyzed events per multiplicity/centrality interval . . . . .	55
203	9	Track selections common to all decay daughters and primary track selections applied to the charged pions from decays of $\Xi^{*0}$ . . . . .	55
205	10	Topological and track selection criteria. . . . .	56
206	11	Summary of the systematic uncertainties on the differential yield, $d^2N/(dp_T dy)$ . Minimum and maximum values in all $p_T$ intervals and multiplicity classes in p–Pb, centrality classes in Pb–Pb are shown for each source. . . . .	80

209 **1 The physics of relativistic heavy-ion collisions**

210 The main objective of relativistic heavy ion physics is to study the nuclear matter under  
 211 extreme conditions which are high temperature and energy density. In these conditions,  
 212 the Standard Model anticipates that the nuclear matter undergo a new phase, where the  
 213 quarks and the gluons are expected to be de-confined called quark-gluon plasma (QGP)  
 214 and to freely move.

215 **1.1 Standard model**

216 If one have question "what the world is made of", our current answer to the question is  
 217 Standard Model (SM) families [13] reported in Table 1. The SM explains the way how  
 218 those basic blocks of matter interact and how they are ruled by four fundamental forces.  
 219 In this explanation, the matter consist of 12 particles, which have a spin of 1/2 (fermions)  
 220 and can be categorized in accordance with way how they interact or equivalently to what  
 221 charges they carry. The basic particles are six quarks (up, down, charm, strange, top and  
 222 bottom) that carry fractional charge of  $+\frac{2}{3}e$  or  $-\frac{1}{3}e$ , and six leptons (electron, electron  
 223 neutrino, muon, muon neutrino, tau, tau neutrino) with integer charge.

Family	Quarks				Leptons		
	Name	Charge[e]	Mass		Name	Charge[e]	Mass
1	u	2/3	$2.2^{+0.6}_{-0.4}$ MeV/c <sup>2</sup>		e <sup>-</sup>	-e	0.511 MeV/c <sup>2</sup>
	d	-1/3	$4.7^{+0.5}_{-0.4}$ MeV/c <sup>2</sup>		$\nu_e$	0	< 2 eV/c <sup>2</sup>
2	c	2/3	$1.27^{+0.03}$ GeV/c <sup>2</sup>		$\mu^-$	-e	105.66 MeV/c <sup>2</sup>
	s	-1/3	$96^{+8}_{-4}$ MeV/c <sup>2</sup>		$\nu_\mu$	-e	< 0.19 eV/c <sup>2</sup>
3	t	2/3	$173.21 \pm 1.22$ GeV/c <sup>2</sup>		$\tau^-$	-e	1.777 GeV/c <sup>2</sup>
	b	-1/3	$4.18^{+0.04}_{-0.03}$ GeV/c <sup>2</sup>		$\nu_\tau$	-e	< 18.2 MeV/c <sup>2</sup>

Table 1: Components of matter in the Standard Model

224 The interactions between elementary particles are described by the exchange of gauge  
 225 bosons(gluon, photon, Z-boson, W-boson), reported in Table 2 including with their cou-  
 226 pling strengths. The leptons are governed the weak force and the electromagnetic force.  
 227 Quarks have color property which is the character of charge in the strong force. The color  
 228 could take one out of three possible values (conventionally red, green and blue). The color  
 229 can not be appeared freely. After they are confined they come out in the form of hadron  
 230 which are colorless. Further explanaition on color is described in Section 1.2. Then, the  
 231 hadrons are grouped into baryon and mesons. Baryons are made up f three quarks,  $qqq$  or  
 232 ( $\bar{q}\bar{q}\bar{q}$ ) while mesons consist of two quarks ( $q\bar{q}$ ).

233 The models that describe these interactions are listed as follows:

234

Force	Strength	Gauge Boson(s)	Applies on
Strong force	1	8 Gluons( $g$ )	Quarks, gluons
Electromagnetic force	$\simeq 10^{-2}$	Photon ( $\gamma$ )	All charged particles
Weak force	$\simeq 10^{-7}$	$W^\pm, Z^0$	Quarks, leptons
Gravitation	$\simeq 10^{-39}$	Gravitons	All particles

Table 2: Fundamental forces

235     **Quantum Electro-Dynamics (QED)** is a quantum field theory of the electromagnetic  
 236 force and describes how light and matter interact. This is the first theory where  
 237 full agreement between quantum mechanics and special relativity is achieved. It explains  
 238 mathematically not only all interactions of light with matter but also those of charged  
 239 particles with one another.

240  
 241     **Electroweak Theory (EW)** is the unified description of two of the four known fundamental  
 242 interactions of nature: electromagnetism and the weak interaction. The first  
 243 measurement of the existence of the weak bosons  $W^+$ ,  $W^-$  and  $Z^0$  was performed in 1983,  
 244 when they were produced and directly observed in  $Spp\bar{S}$  collisions at CERN.

245  
 246     **Quantum Chromo-dynamics (QCD)** is the theory of the strong interaction (color  
 247 force), describing the interactions between quarks and gluons which make up the hadrons.  
 248 Starting from the classification of the large amount of particles discovered during the fifties,  
 249 the original idea of the quark model by Gell-Mann (Nobel Prize in 1969) has been developed  
 250 during the sixties until 1973, when David J. Gross, H. David Politzer and Frank Wilczek  
 251 discovered the asymptotic freedom property of the strong nuclear interaction.

## 252     1.2 QCD and Quark-Gluon plasma

253 As the number of known particle species became large, the idea that these could be the  
 254 elementary constituents of matter was replaced by the notion that these species could in  
 255 fact be composite objects made up of fewer, more elementary particles, in a similar way to  
 256 what had already happened to the elements of Mendeleev's Periodic Table. The original  
 257 idea by Gell-Mann (1964) was that the hadrons could be obtained as combination of the  
 258 fundamental representation of an  $SU_f(3)$  group, where three different flavors of quark ( $q$   
 259 = u, d, s) combine to build mesons ( $q\bar{q}$ ) and hadrons ( $qqq$ ). However, when cataloging  
 260 hadrons using the  $SU_f(3)$  group, there are anomalous states, such as the  $\Omega^-(sss)$  and the  
 261  $\Delta^{++}(uuu)$ , that are combinations of three quarks of the same flavor, in clear contrast  
 262 with the Pauli exclusion principle for fermions. A solution was proposed in 1965 by Moo-  
 263 Young Han with Yoichiro Nambu and Oscar W. Greenberg, who independently solved the  
 264 problem by proposing that quarks possess an additional  $SU(3)$  gauge quantum number,

265 later called color charge. This new quantum number may assume three states, represented  
 266 by the three primary colors: red, green and blue (denoted symbolically by R, G and B,  
 267 respectively). The introduction of this new quantum number also provides an explanation  
 268 to other empirical evidence, such as the fact that no  $qq$ ,  $\bar{q}q$  or the single quark have never  
 269 been observed directly. On the other hand, the existence of color charge gives rise to the  
 270 possible existence of differently colored states for each particle. Thus, we could have many  
 271 states for the proton, such as  $u_R u_G d_B$ ,  $u_R u_G d_G$ ,  $u_B u_R d_R$ , and so on. The fundamental  
 272 rule that solves such contradictions is that all the particle states observed in nature are  
 273 "colorless" or "white" (or, to be more precise, unchanged under  $SU_c(3)$  rotations). The  
 274 dynamics of the quarks and gluons are controlled by the gauge invariant QCD Lagrangian:

$$\mathcal{L}_{QCD} = \underbrace{i\delta_{ij}\bar{\Psi}_q^i\gamma^\mu\partial_\mu\Psi_q^j}_{\mathcal{L}_1} + \underbrace{g_s\bar{\Psi}_q^i\gamma^\mu t_{ij}^a A_\mu^a\Psi_q^j}_{\mathcal{L}_2} + \underbrace{m_q\bar{\Psi}_q^i\Psi_q^j}_{\mathcal{L}_3} + \underbrace{\frac{1}{4}F_{\mu\nu}^a F^{a\mu\nu}}_{\mathcal{L}_4} \quad (1)$$

275 where the coloured gluon field tensor,  $F_{\mu\nu}^a$  (with color index  $a$ ) and the squared gauge  
 276 coupling parameter,  $g_s^2$  (associated to the strong coupling constant  $\alpha_s$ ) are defined as:

$$F_{\mu\nu}^a = \partial_\mu A_\nu^a - \partial_\nu A_\mu^a + g_s f^{abc} A_\mu^b A_\nu^c \quad (2)$$

277 and

$$g_s^2 = 4\pi\alpha_s \quad (3)$$

278 where:

- 279 •  $\Psi_q^i$ : the quark field with flavor q and color index  $i \in [1;3]$ , such as  $\Psi_q = (\Psi_{qR}, \Psi_{qG},$   
 280       $\Psi_{qB})^T$  and  $A_\mu^a$  is the gluon field with color index a (adjoint representation)
- 281 •  $\gamma^\mu$ : Dirac matrices that express the vector nature of the strong interaction, with  $\mu$   
 282      being the Lorentz vector associated index
- 283 •  $m_q$ : quark mass, a priori not equal to zero (resulting from the Higgs mechanism or  
 284      equivalent)
- 285 •  $t_{ij}^a$ : generator matrices of the group  $SU_c(3)$ , proportional to the Gell-Mann matrices,  
 286      that perform revolutions in color space, representing interaction of quarks and gluons
- 287 •  $f^{abc}$ : structure constant of QCD

288 Each of the four terms of the QCD Lagrangian expresses and aspect of the interaction,  
 289 specifically:

- 290 •  $\mathcal{L}_1$ : gives the kinetic energy of the quark field  $\Psi_q^i$

- 291     •  $\mathcal{L}_2$ : gives the interaction between quarks (fermions) and gluons (the bosons of the  
292       interaction)
- 293     •  $\mathcal{L}_3$ : gives the mass of the quarks
- 294     •  $\mathcal{L}_4$ : gives the kinetic energy of the gluons

295     The terms of this equation, together with the fundamental parameters  $\alpha_s$  and  $m_q$ ,  
296     summarize in just one expression all the features of the strong interaction. The first three  
297     terms describe the free propagation of quarks and gluons and the quark-gluon interaction.  
298     The remaining two terms show the presence of three and four gluon vertices in QCD and  
299     reflect the fact that gluons themselves carry color charge. This is a consequence of the non-  
300     abelian<sup>4</sup> character of the gauge group. This peculiarity of the QCD interaction imposes the  
301     evolution of the strong coupling constant,  $\alpha_s$ . The corresponding trend has been measured  
302     experimentally, and compared in Figure 1 with predictions. A practical consequence of  
303     this behavior is that the corresponding potential has a completely different shape than the  
304     other fundamental interactions and can be expressed by the following equation:

$$V(r) = -4 \frac{\alpha_s}{3r} + kr \quad (4)$$

305     where  $r$  is the separation distance between the two quarks and  $k$  is a constant that is  
306     approximately 1 GeV/fm.

307     Three are main properties of the QCD interaction:

308     **Confinement** At large distances between quarks and gluons (i.e. small values of trans-  
309     ferred momentum  $Q$  in Figure 1) the coupling constant is large and the associated force  
310     is strong enough to keep these elementary con- stituents (usually called partons) confined  
311     in bounded states. As expressed in the Equation 4, the attractive potential increases with  
312     the increasing of the relative distance between the two partons preventing the separation  
313     of an individual quark or gluon. This explains the meaning of the term "confinement"  
314     adopted to describe this energy regime. From the theoretical point of view, the large value  
315     of  $\alpha_s$  make impossible any perturbative approach in the solution of the Hamilton equation  
316     of the system. A successful solution is to perform the study of the system on a discrete  
317     space. Such techniques are known as lattice QCD and are based on numerical Monte Carlo  
318     simulations. The challenge for the calculations is to reduce the lattice spacing in order to  
319     approach the continuum.

321     **Asymptotic freedom** Reducing the distance between quarks and gluons (i.e. increas-  
322     ing  $Q$  in Figure 1) the coupling constant  $\alpha_s$  becomes smaller. As anticipated, this is a  
323     unique feature among the forces and comes from the non-abelian nature of the QCD gauge  
324     symmetry. Such a phenomenon is also depicted by the weakening of the anti-screening  
325     effect of the surround- ing virtual gluons with decreasing distance. In this way two quarks

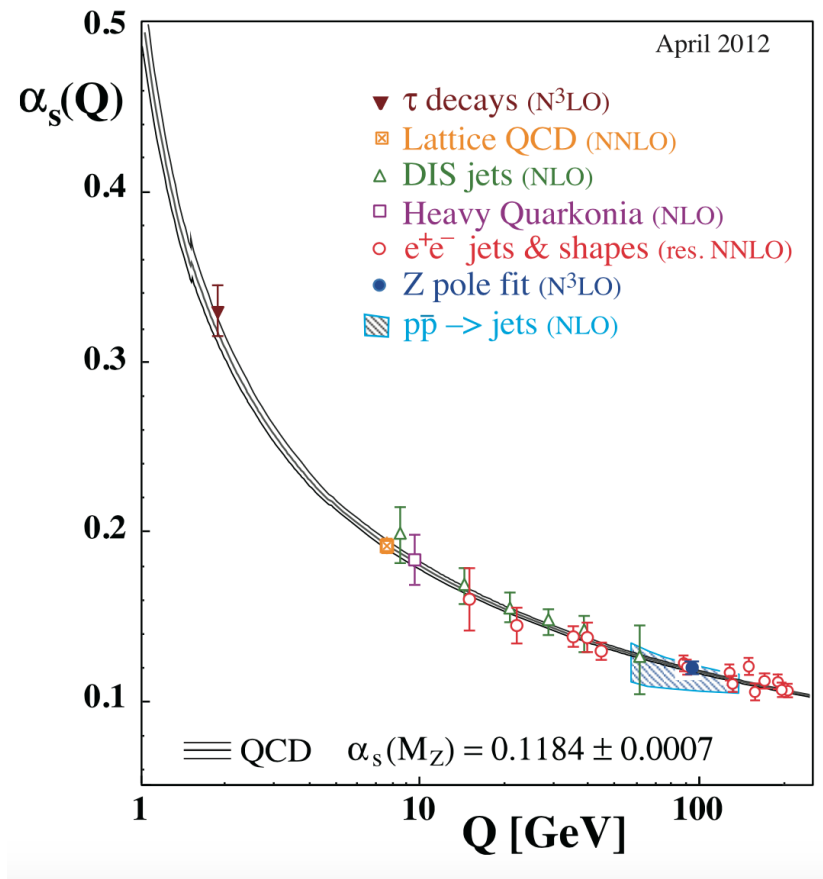


Figure 1: QCD coupling constant as a function of momentum transfer. Experimental data and also theoretical prediction are presented. [1]

327 closer and closer in space show each other a smaller and smaller color charge.

328

329 **Chiral symmetry** One further property of interest is connected to the chirality of  
330 the quark. It can be verified that the QCD lagrangian for massless quarks is invariant  
331 under a chiral rotation ( $SU_L(N_f) \times SU_R(N_f)$ ), while the operator  $\bar{q}q = \bar{q}_L q_R + \bar{q}_R q_L$  is  
332 not invariant (in the axial part), meaning that the mesons (state  $\bar{q}q$ ) should have the same  
333 mass. Experimentally this is clearly not true, and it could be shown that the axial current  
334 is conserved (PCAC and the Goldberger-Treiman relation). The solution to this puzzle  
335 is that the chiral (axial-vector) symmetry is spontaneously broken; this means that the  
336 symmetry of the Hamiltonian is not a symmetry of the corresponding ground state. It  
337 has also been shown, by G. t'Hooft, that the confinement implies a dynamical breaking  
338 of the chiral symmetry. This means that the breaking comes from the interaction between  
339 the objects in the system. From this follows that the masses of the quarks are strongly  
340 increased because of the interaction with the constituents of the system. This mechanism,  
341 known as dynamical chiral symmetry breaking justifies the mass of the hadrons, reducing  
342 the role of the Higgs mechanism in the mass explanation at least for the light hadrons.

343 The asymptotic freedom property suggests the existence of a state of matter, called  
344 Quark-Gluon Plasma (QGP), in which the constituents of the hadrons are de-confined.  
345 The hatched region in Figure 2 presents the expected phase boundary between partonic  
346 and hadronic matter from lattice QCD calculations.

347 Two relevant thermodynamical observables of the system are plotted in the figure. One  
348 is temperature  $T$  and another one is the baryonic chemical potential  $\mu_B$ . The red points  
349 have been measured from thermal models fit on data from different experiment [14] and  
350 lie along a line that represent the limit between the two phases. As one can see in Figure  
351 2, there are different ways to achieve the transition. It can be performed by changing the  
352 temperature and/or the net baryonic density ( $\mu_B$ ).

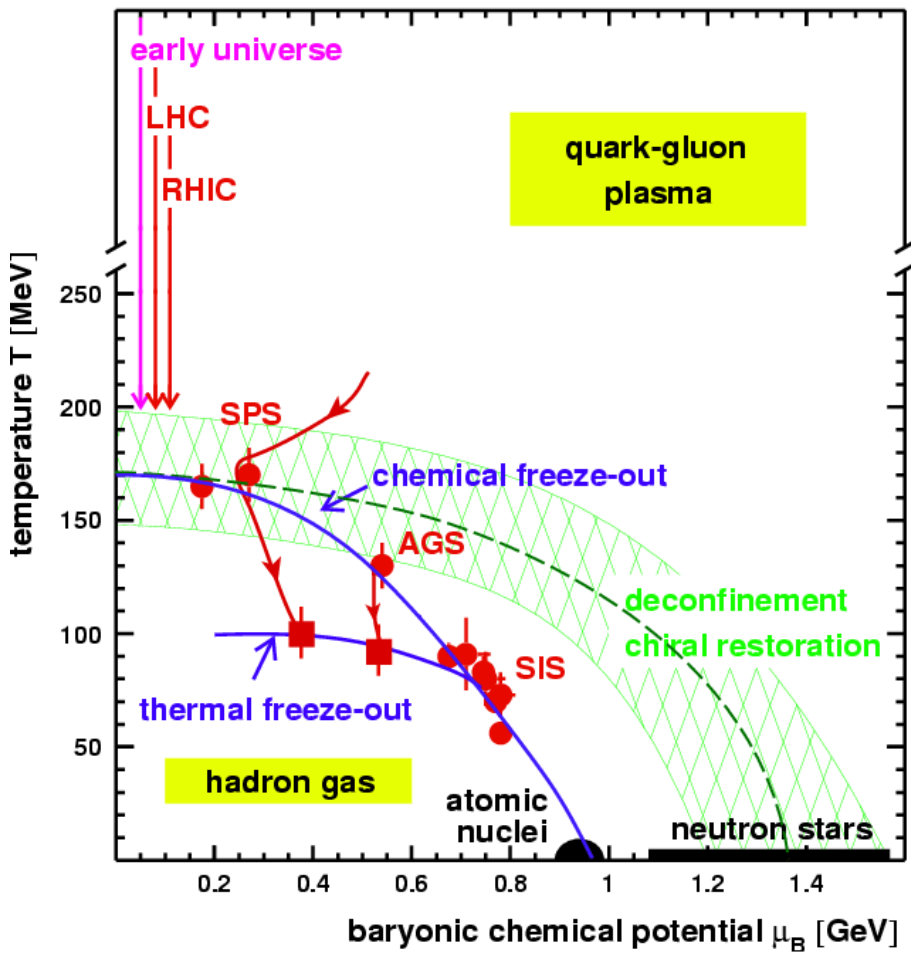


Figure 2: QCD phase diagram in  $T$  as function of  $\mu_B$ . The chemical freeze out points are determined from thermal models fit to heavy ion data at SIS, AGS, and SPS energies. (<http://na49info.web.cern.ch/na49info/Public/Press/findings.html>)

### 353 1.3 Heavy Ion Collisions

354 Knowledge of the space-time evolution of the system created in high energy heavy ion  
 355 collisions help to understand the dynamics of nuclear matter under extreme conditions.  
 356 The Figure 3 presents the schematic of the time evolution in case of collision of two Lorentz  
 357 contracted nuclei at very high energy. After the colliding, a large amount of energy can be  
 358 deposited in a small area of space and in a short duration of time. The matter produced  
 359 might have very high energy density and temperature so that it is sufficiently able to reach  
 360 to QGP that is baryon free region.

361 Just after the colliding, the medium may not be in thermal equilibrium which can be  
 362 reached after that the evolution is governed by the law of thermodynamics. As the system  
 363 expands and cools, the hadronization takes place and the freeze out comes after some  
 364 time. Different stages during the collisions can be studied by various observables, such as,  
 365 Electromagnetic probes, Quarkonia and heavy flavour, Hard probes, Electroweak probes,  
 366 global properties and Freeze-out condition as well. Most of the produced particles in the  
 367 high energy heavy-ion collisions are emitted at freeze-out. In order to estimate the energy  
 368 density, pressure, temperature and baryon chemical potential, the study of particle after  
 369 freeze-out gives crucial information. Those quantities could be derived from measurement  
 370 of multiplicity and rapidity distribution, transverse momentum ( $p_T$ ) distributions.

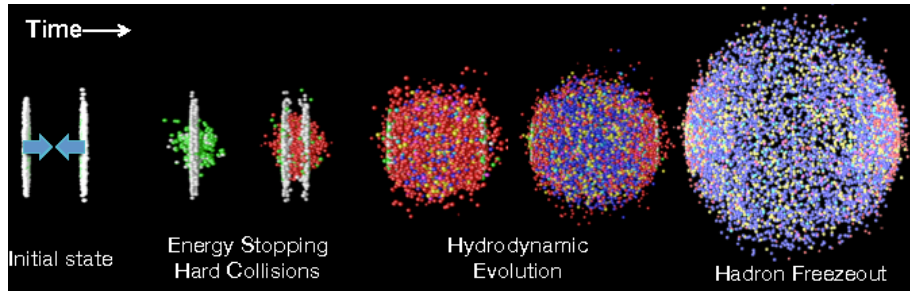


Figure 3: The time evolution of a high energy heavy ion collision. [2]

371 In the case a QGP is formed, it will eventually expand because of its internal pressure.  
 372 As the system expands it also cools. The space-time evolution of the expansion can be  
 373 seen in Figure 4 (right side). A and B represent the two incoming ion beams. After a pre-  
 374 equilibrium phase a QGP is formed. As it expands, the system will eventually reach what  
 375 is known as the critical temperature ( $T_c$ ). At this point partons begin to hadronize and this  
 376 will continue until the chemical freeze-out ( $T_{ch}$ ) takes place, when inelastic collisions cease.  
 377 At this stage the distribution of hadrons is frozen. As cooling and expansion continue the  
 378 hadrons reach what is called thermal freeze out ( $T_{fo}$ ). Here the elastic collisions stop and  
 379 the hadrons carry fixed momenta. The QGP state can not be directly observed, because of  
 380 its short lifetime. Instead, through experiment we measure the final state hadrons, which

<sup>381</sup> have a fixed momentum after  $T_{fo}$ . The observables of interest should tell us about the  
<sup>382</sup> de-confinement and the thermodynamic properties of the matter. Moreover, experimental  
<sup>383</sup> measurements include yields and  $p_T$ spectra of various particle species, azimuthal studies  
<sup>384</sup> of high  $p_T$ particles, phase space distributions, and particle correlations.

<sup>385</sup> A practical way to reach a critical condition in which a nuclear system should undergo  
<sup>386</sup> a phase transition to the QGP, at high temperature and/or matter density, is to collide  
<sup>387</sup> two nuclei at sufficiently high energy. Therefore, relativistic and ultra-relativistic heavy-ion  
<sup>388</sup> collisions are a unique tool to study nuclear matter under extreme conditions.

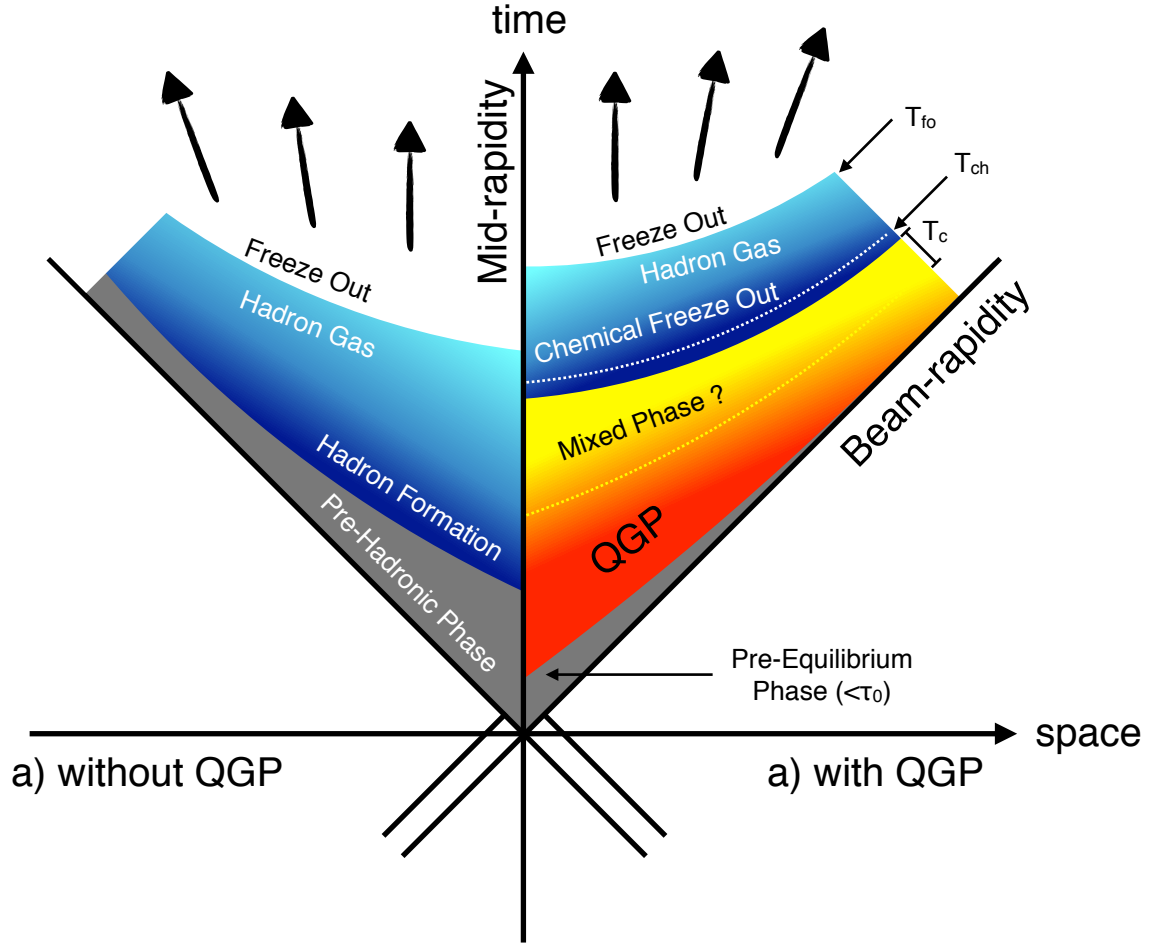


Figure 4: Hydrodynamic evolution of a heavy ion collision with and without the formation of a QGP.

## 389 2 Theoretical models

### 390 2.1 Statistical-Thermal model

391 The statistical-thermal model deal with the fireball created from high energy collisions as  
 392 an ideal gas of hadrons including resonances. These hadrons are described by local thermal  
 393 distributions at freeze-out with the parameters common to all particle species. The  
 394 model has proved successful in applications to relativistic collisions of both heavy ions and  
 395 elementary particles. The comparison between prediction and data obtained from Pb–Pb  
 396 collisions are shown in Figure 5. In light of this success, THERMUS, a thermal model  
 397 analysis package, has been developed for incorporation into the object-oriented ROOT  
 398 framework [15].

399

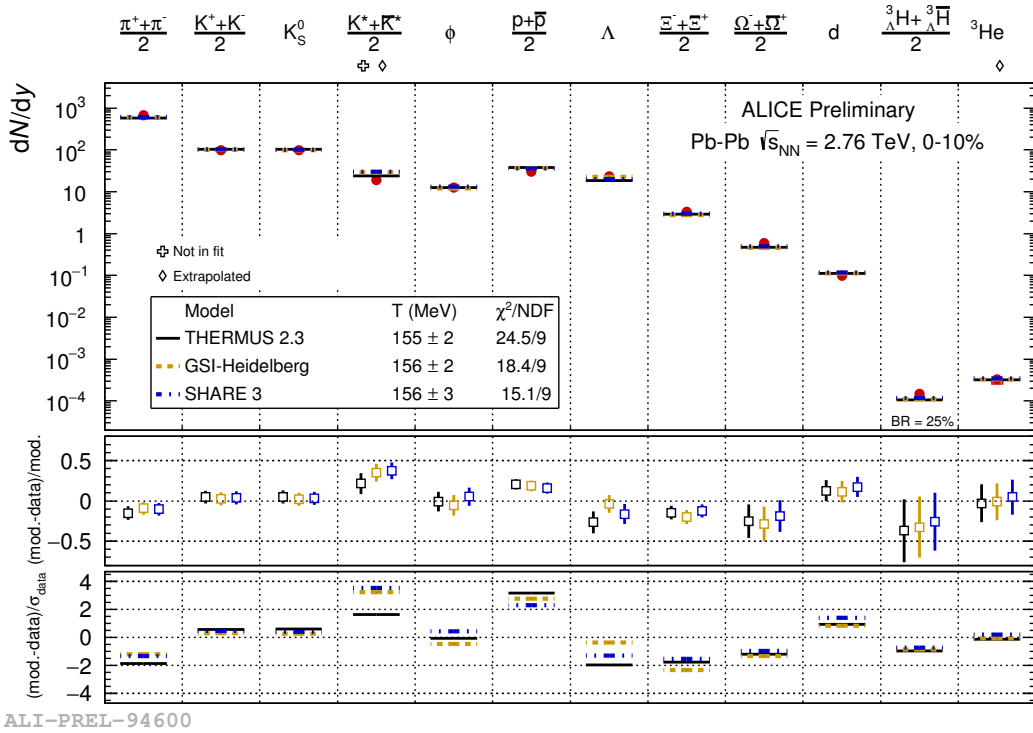


Figure 5: Grand canonical thermal fit of 0-10% central Pb-Pb collisions, with 3 models (THERMUS, GSI, SHARE).

400 There are three types of statistical-thermal models in explaining data in high energy  
 401 nuclear physics and THERMUS treats the system quantum numbers B (baryon number),

402 S (strangeness) and Q (charge) within three distinct formalisms:

- 403 1. **Grand-Canonical Ensemble:** Because the hot dense matter produced in nucleus-  
404 nucleus collisions is large enough, this ensemble is the most widely used in applica-  
405 tions to heavy-ion collisions, in which the quantum numbers or particle numbers are  
406 conserved on average through the temperature and chemical potential.
- 407 2. **Fully-Canonical Ensemble:** In which B, S and Q are exactly conserved and this  
408 ensemble used in high-energy elementary collisions such as pp, p $\bar{p}$  and e $^-$ e $^+$  collisions.
- 409 3. **Strangeness-Canonical Ensemble:** In heavy-ion collisions, the large numbers of  
410 baryons and charged particles generally allows baryon number and charge to be  
411 treated grand-canonically. However, in small systems or at low temperatures, a  
412 canonical treatment leads to a suppression of hadrons carrying non-zero quantum  
413 numbers, since these particles have to be created in pairs and the resulting low pro-  
414 duction of strange particles needs a canonical treatment of strangeness. Within this  
415 ensemble the strangeness in the system is fixed exactly by its initial value of S, while  
416 the baryon and charge content are treated grand-canonically.

417 In order to calculate the thermal properties of a system, the partition function requires to  
418 be evaluated. The form of it clearly depends on the choice of ensemble. In the present  
419 analysis the strangeness-canonical ensemble used and statistical-thermal model requires six  
420 parameters as input: the chemical freeze-out temperature  $T$ , baryon and charge chemical  
421 potentials  $\mu_B$  and  $\mu_Q$  respectively, canonical or correlation radius,  $R_C$ ; the radius inside  
422 which strangeness is exactly conserved and the fireball radius  $R$ . An additional strangeness  
423 saturation factor  $\gamma_S$  has been used as indicator of a possible departure from equilibrium  
424 and  $\gamma_S = 1.0$  corresponds to complete strangeness equilibration.

425 The volume dependence cancels out when studying the particle ratios as well as strangeness  
426 canonical equivalent to grand canonical formalism if  $\Delta S = 0$  in the ratios and  $\gamma_S$  also can-  
427 cels out. Parameters used in the analysis reported in Table 3.

Table 3: Parameters used in the thermal-model calculations.

Parameter	Value
$T$ (MeV)	varied
$\mu_B$ (MeV)	0.1
$\mu_Q$ (MeV)	0.0
$\gamma_S$	1.0

428

429 **2.1.1 Calculations**

430 *Concept:*

431 In order to calculate the particle ratios within strangeness canonical formalism of THER-  
432 MUS, temperature varied between 60 MeV to 180 MeV and particle yields extracted for  
433 each temperature value and then primary particle ratios calculated for each case.

434

435 *Feed-Down Correction:*

436 Since the particle yields measured by the detectors in collision experiments include feed-  
437 down from heavier hadrons and hadronic resonances, the primitive hadrons are allowed to  
438 decay to particles considered stable by the experiment before model predictions are com-  
439 compared with experimental data. In the analysis only  $\Lambda$  particles counted as stable (do not  
440 allowed to decay) so there is no feed-down contribution from these particles to the other  
441 ratios.

442

443 Properties of studied particles and their particle ratios listed in Table 4 and Table 5,  
444 respectively.

445

446

Table 4: Properties of particles used in the ratio calculations.

Particle	$\Delta^{++}$	$\Delta^{++}$	$p$	$K^{*0}$	$K^+$	$\Lambda^*$	$\Lambda$	$\Sigma^{*+}$	$\Sigma^+$	$\Sigma^0$	$\Xi^{*0}$	$\Xi^-$
Mass (MeV/ $c^2$ )	1232	938.27	895.92	493.67	1519.5	1115.68	1382.8	1189.37	1192.64	1531.80	1321.31	-
Width (MeV/ $c^2$ )	120	-	50.7	-	15.6	-	37.6	-	-	9.1	-	-
$c\tau$ (fm)	1.6	-	3.9	-12.6	-	5.51	-	-	21.6	-	-	-
Ang. Momentum ( $J$ )	$3/2$	$1/2$	1	0	$3/2$	$1/2$	$3/2$	$1/2$	$1/2$	$3/2$	$1/2$	$1/2$
$^{22}_N$ Isospin ( $I$ )	$3/2$	$1/2$	$1/2$	$1/2$	0	0	1	1	1	$1/2$	$1/2$	$1/2$
Parity ( $P$ )	+1	+1	-1	0	-1	+1	+1	+1	+1	+1	+1	+1
Strangeness ( $S$ )	0	0	1	1	-1	-1	-1	-1	-1	-2	-2	-2
Baryon Number ( $B$ )	1	1	0	0	1	1	1	1	1	1	1	1
Decay Channel	$p\pi^+$	-	$\pi^-$	$\mu^+\nu_\mu$	$pK^-$	$p\pi^-$	$\Lambda\pi^+$	$p\pi^0$	$\Lambda\gamma$	$\Xi^-\pi^+$	$\Lambda\pi^-$	-
Branching Ratio (%)	$\sim 100$	-	$\sim 66.7$	$\sim 63.54$	$\sim 45$	$\sim 63.9$	$\sim 87$	$\sim 51.6$	$\sim 100$	$\sim 64$	$\sim 99.9$	-
Q-Value(MeV/ $c^2$ )	154.16	-	262.68	-	87.55	37.84	127.55	111.53	76.96	70.92	70.66	-

Table 5: Difference of mass ( $\Delta M$ ), baryon number ( $\Delta B$ ), strangeness ( $\Delta S$ ) and charge ( $\Delta Q$ ) of the ratios.

Particle	$\Delta^{++}/p$	$K^*/K^+$	$\Lambda^*/\Lambda$	$\Sigma^{*+}/\Lambda$	$\Sigma^0/\Lambda$	$\Sigma^{*+}/\Sigma^+$	$\Xi^{*0}/\Xi^-$
$\Delta M$ (MeV/ $c^2$ )	293.8	402.25	403.82	267.12	76.96	193.43	210.49
$\Delta B$	0	0	0	0	0	0	0
$\Delta S$	0	0	0	0	0	0	0
$\Delta Q$	+1	-1	0	+1	0	0	-1
Slope (%) per MeV	0.19	0.76	0.98	0.25	-0.08	0.37	0.42

<sup>447</sup> **2.1.2 Results and comparison with data**

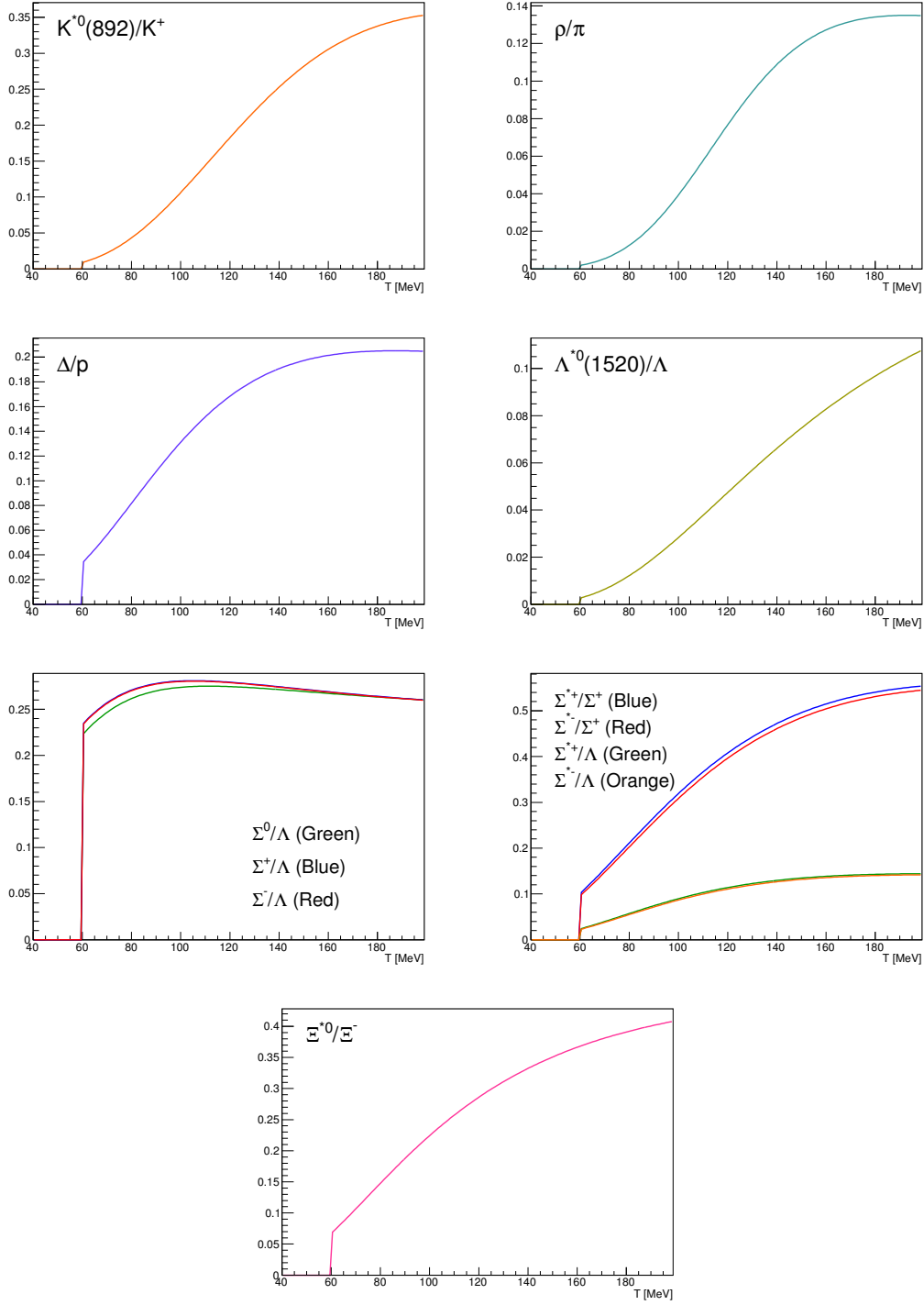


Figure 6: Ratio of baryonic and mesonic resonances over their stable partner as a function of temperature.

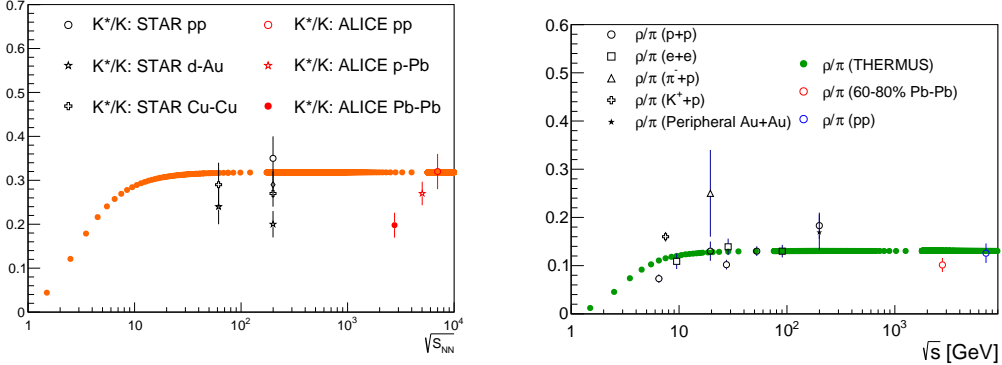


Figure 7: Ratio of resonances over their stable partner as a function of  $\sqrt{(s)}$ .

## 448 2.2 EPOS, UrQMD

449 The EPOS3 model [16, 17, 18] describes the full evolution of a heavy-ion collision. The  
 450 initial stage is treated via a multiple-scattering approach based on Pomerons and strings.  
 451 The reaction volume is divided into a core and a corona part [19]. The core is taken as  
 452 the initial condition for the QGP evolution, for which one employ viscous hydrodynamics.  
 453 The corona part is simply composed of hadrons from string decays. After hadronisation of  
 454 the fluid (core part), these hadrons and as well the corona hadrons are fed into UrQMD  
 455 [20, 21], which describes hadronic interactions in a microscopic approach. The chemical  
 456 and kinetic freeze-outs occur within this phase. The chemical freeze-out is expected to  
 457 occur shortly after the phase transition from partonic to hadronic matter and is followed  
 458 by the kinetic freeze-out.

459 As explained in [16, 17, 18, 19], EPOS3 is an event generator based on 3+1D vis-  
 460 cous hydrodynamical evolution starting from flux tube as an initial conditions, which are  
 461 produced in the Gribov-Regge multiple scattering framework. An individual scattering is  
 462 treated as a Pomeron, identified with a parton ladder, eventually showing up as flux tubes  
 463 (or strings). Each parton ladder is composed of a pQCD hard process, plus initial and final  
 464 state linear parton emission.

465 The final state partonic system (corresponding to a Pomeron) amounts to (usually two)  
 466 color flux tubes, being mainly longitudinal, with transversely moving pieces carrying the  
 467  $p_T$  of the partons from hard scatterings. One has two flux tubes based on the cylindrical  
 468 topology of the Pomerons. Each quark- antiquark pair in the parton ladder will cut a string  
 469 into two; in this sense one may have more than two flux tubes. In any case, these flux  
 470 tubes eventually constitute both bulk matter, also referred to as "core" (which thermalizes,  
 471 flows, and finally hadronizes) and jets (also referred to as "corona"), according to some

472 criteria based on the energy of the string segments and the local string density. For the  
473 core, we use a 3+1D viscous hydrodynamic approach, employing a realistic equation of  
474 state, compatible with lQCD results. We employ for all calculations in this paper a value  
475 of  $\eta/s = 0.08$ . Whenever a hadronization temperature of  $T_H$  is reached, we apply the  
476 usual Cooper-Frye freeze-out procedure, to convert the fluid into particles. We use  $T_H =$   
477 166MeV. From this point on, we apply the hadronic cascade UrQMD [20, 21], about which  
478 more details are given later. All hadrons participate in the cascade, including those from  
479 the core (after freeze- out) and the corona. The corona particles, from string decay, are only  
480 "visible" after a certain formation time (some constant of order one fm/c), multiplied by  
481 the corresponding gamma factor), so very high  $p_T$  particles have a good chance to escape.

482 The UrQMD model is a non-equilibrium transport approach. The interactions of  
483 hadrons in the current version include binary elastic and  $2 \rightarrow n$  inelastic scatterings, res-  
484 onance creations and decays, string excitations, particle + antiparticle annihilations as  
485 well as strangeness exchange reactions. The cross sections and branching ratios for the  
486 corresponding interactions are taken from experimental measurements (where available),  
487 detailed balance relations and the additive quark model. The model describes the full  
488 phase-space evolution of all hadrons, including resonances, in a heavy- ion collision based  
489 on their hadronic interactions and their decay products. Due to the short lifetime of res-  
490 onances, their decay products may interact in the hadronic phase. This is not the case  
491 for weak decays, where the system has already decoupled at the time of the decay. As  
492 discussed previously, the experimental reconstruction of resonances will be influenced by  
493 the final state interactions of the decay products. Resonance signals have been previously  
494 studied using the UrQMD model.

### 495 3 Production of hyperon resonance

496 The Quark Model, proposed independently by Murray Gell-Mann and Yuval Ne'eman in  
 497 1964 [22], enables the classification of hadrons in terms of their constituent quarks. In  
 498 this model, the lighter mesons and baryons are representations of an  $SU_f(3)$  group, whose  
 499 fundamental representation is the three dimensional vector (u, d, s). These are the three  
 500 lighter quarks whose characteristics are reported in Table reftable:quark.

Light flavor	d	u	s
Baryon number (B)	+1/3	+1/3	+1/3
Electric charge (Q)	-1/3	+2/3	-1/3
Isospin (I)	-1/2	+1/2	0
Strangeness (S)	0	0	-1
mass ( $\text{MeV}/c^2$ )	$2.3^{+0.7}_{-0.5}$	$4.8^{+0.5}_{-0.3}$	$95 \pm 5$

Table 6: Quantum numbers and masses associated to the three lighter quarks: u, d and s

501 The hadronic state are obtained from the decomposition of the following scalar prod-  
 502 ucts of the fundamental representations of the group:

503      Meson ( $q\bar{q}$ ) :  $3 \otimes \bar{3} = 1 \oplus 8$

505      Baryon ( $qqq$ ) :  $3 \otimes 3 \otimes 3 = 10_S \oplus 8_M \oplus 8_M \oplus 1_A$

507      For the baryons without *c* or *b* quark, flavor and spin may be combined in an approxi-  
 508 mate flavor-spin  $SU(6)$ , in which the six basic states are  $d \uparrow, d \downarrow, \dots, s \downarrow$  ( $\uparrow, \downarrow$  = spin up,  
 509 down). Then the baryons belong to the multiplets on the right side of

511       $6 \otimes 6 \otimes 6 = 56_S \oplus 70_M \oplus 70_M \oplus 20_A$

513      Here, the 56 representation can be decompose in an octet ( $J^P = 1/2^+$ ) and a decuplet  
 514 ( $J^P = 3/2^+$ ), as can be seen in Figure 8 and Figure 9.

516      Among these hadrons, the special family of particles that contain at least one strange  
 517 quark but not heavier quarks (like charm or bottom), are called hyperons. These are:  
 518 the  $\Lambda$ (uds), the triplet  $\Sigma^+(uus)$ ,  $\Sigma^0(uds)$ ,  $\Sigma^-(dds)$ , the doublet  $\Xi^-(dss)$ ,  $\Xi^0(uss)$  and the  
 519  $\Omega(sss)$  and the corresponding antiparticles.  $\Xi$  and  $\Omega$  are the only hyperons containing more  
 520 than one strange quark, hence they are called multi-strange baryons. Resonances shown  
 521 in Figure reffig:decuplet having \* with its name (e.g.  $X^{*\pm}$ ) are particles which have higher  
 522 mass than the corresponding ground state particle with the same quark content.

523      Different resonances having various lifetimes (Table 7) can be used as tool to explore  
 524 different stages of the fireball expansion as discussed in section 1.3. In order to have

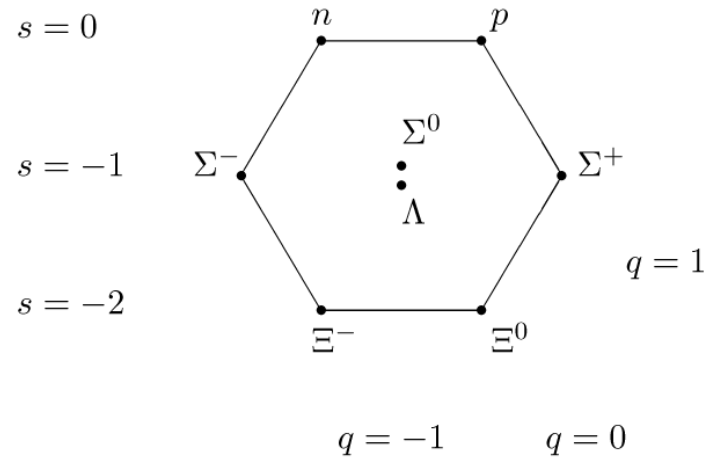


Figure 8: The  $J^P = 1/2^+$  ground state baryon octet

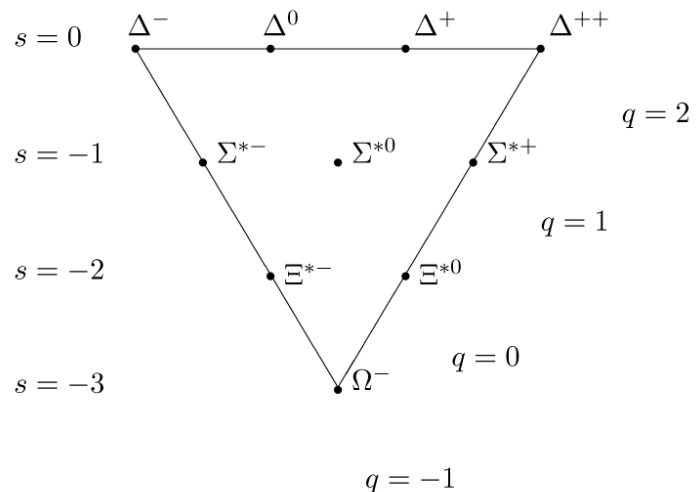


Figure 9: The  $J^P = 3/2^+$  baryon decuplet

525 insight on the role of the re-scattering effect between the freeze-out phases, it is important  
 526 to measure the ratio between resonances and stable hadrons and compare it with different  
 527 lifetimes.

Particle	$\rho(770)$	$\Delta(1232)$	$K^*(892)$	$\Sigma(1385)$	$\Lambda(1520)$	$\Xi(1530)$	$\Phi(1020)$
Lifetime[c $\tau$ ]	1.3 fm	1.7 fm	4.0 fm	5.5 fm	10.3 fm	22 fm	46 fm

Table 7: Lifetime of hadronic resonances

528 In the following, a general overview of the role of the strange quark within the QGP  
 529 studies with heavy-ion collisions is given. And importance of the measurement of resonance  
 530 is explained as probe of properties in the duration of hadronic phase from the chemical( $T_{ch}$ )  
 531 to the kinetic freeze-out( $T_{kin}$ ).

### 532 3.1 Strange quark and hyperons

533 The original interest in the strangeness in the context of the QGP comes from an idea by  
 534 Johann Rafelski and Berndt Müller. In 1982, they suggested a possible signature for the  
 535 formation of a QGP in a heavy-ion collision [23]. The key argument, at a fixed collision  
 536 energy, rests on the different production mechanism of the s quark within two different  
 537 systems:

538 **1. Hadron Gas (HG)** , where the degrees of freedom are the hadronic ones, as quark and  
 539 gluons are confined. The great abundance of pions in the HG suggests to consider the  
 540 production of strange particles from the reaction between them. Direct production  
 541 can be observed with  $\pi + \pi \rightarrow \pi + \pi + \text{strange hadron} + \text{antiparticle}$ , considering  
 542 the baryon and strange number conservation. This means that, in order to create the  
 543 strange particle and anti-particle at once, the reaction threshold (energy needed to  
 544 produce mesons or baryons) corresponds to tow times the rest mass of the hadrons.  
 545 (2230 MeV for  $\Lambda + \bar{\Lambda}$ , 2642 MeV for  $\Xi + \bar{\Xi}$ . 3344 MeV for  $\Omega + \bar{\Omega}$ )

546 **2. QGP** , where the degrees of freedom are partonic ones, with quarks and gluons free  
 547 with respect to each other. The high gluon density gives the possibility to have  
 548 new production mechanisms abreast the usual quark-pair annihilation which are the  
 549 gluon fusion processes. It becomes the dominant process of  $s\bar{s}$  pairs creation. In  
 550 these reactions the energy threshold is equal to the naked mass of the two strange  
 551 quarks  $\approx 2 \cdot 100$  MeV.

552 The quarks can not be seen directly due to the strong interaction which keeps them  
 553 confined. Once they are free, as in a QGP, the quarks recover their bare masses. (Note  
 554 that, only the part of mass of hadron comes from the mass of the constituent quarks.) It  
 555 was predicted that, if the QGP is formed, an enhancement of the strange quarks should

556 occur, because the production of  $s\bar{s}$  pairs becomes easier due to the lower energy needed as  
557 explained above. When the QGP cools down, these strange quarks eventually recombine  
558 into hadrons favoring also an enhancement of the number of strange hadrons. This effect is  
559 larger for hadrons with higher strangeness, with the following scaling for the number type:  
560 Ordering in QGP:  $N_\Omega > N_\Xi > N_\Lambda$

561 where  $N_\Omega$ ,  $N_\Xi$ ,  $N_\Lambda$  are the number of produced  $\Omega$ ,  $\Xi$  and  $\Lambda$ . A certain enhancement of  
562 strange hadrons can occur also in a hadron gas system, but the processes of hadronisation  
563 in this case are relatively easy for  $K$  and  $\Lambda$ . and progressively harder for hadrons with  
564 higher strangeness, hence the relation would be:

565 Ordering in HG:  $N_\Omega < N_\Xi < N_\Lambda$ .

566 The measurement of multi-strange hadrons in heavy-ion collisions with respect to small  
567 collisions is considered to be a signature of the formation of the QGP and it was observed  
568 at SPS, RHIC and LHC. [24]

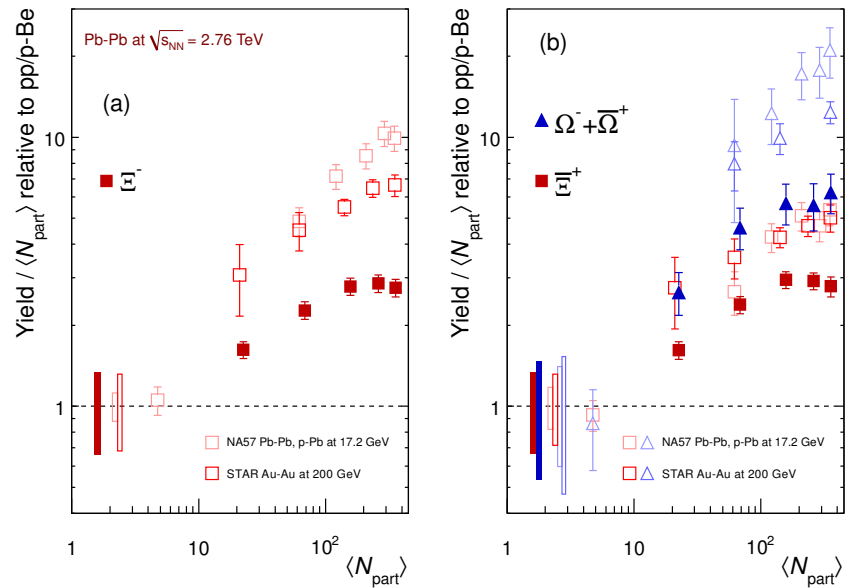


Figure 10: Integrated yield relative to small system (pp or p-Be) as a function of the mean number of participants  $\langle N_{part} \rangle$  in the rapidity range  $|y| < 0.5$ . The results from ALICE are presented as full symbols, RHIC and SPS data are shown as open symbols. Boxes on the dashed line at unity represent statistical and systematic uncertainties on the pp or p-Be reference.

569 The measured enhancement factors of baryons with increasing strangeness content are  
570 reported in Figure 10 as a function of the mean number of participants,  $\langle N_{part} \rangle$ , compared  
571 with measurements at SPS and RHIC. As shown in the Figure 10, the enhancement in-

572 creases with  $\langle N_{part} \rangle$  which is variable to be comparable to the centrality in Pb–Pb collisions  
 573 and the effect is more pronounced for particle with larger strangeness content. If one con-  
 574 sider the collision energy dependency, the comparison with measurement from the previous  
 575 experiment shows that the relative enhancements decrease with increasing energy. This  
 576 phenomena has been explained in terms of a statistical model via strangeness-canonical  
 577 ensemble discussed in Section 2.1.

578 In a large system with a large number of produced particles, the conservation law of  
 579 a quantum number, e.g., strangeness, can be implemented on the average by using the  
 580 corresponding chemical potential. This is the Grand Canonical formulation that was dis-  
 581 cussed in previous Section. In a small system, however, with small particles multiplicities,  
 582 conservation laws must be implemented locally on an event-by-event basis. The Canonical  
 583 formulation which conservation of quantum numbers reduce the possibility for strangeness  
 584 particle production.[25]. This canonical suppression factor increase with higher energy in  
 585 the center of mass of the collision and could explain the less enhancement in the results  
 586 from higher energy system.

587 **3.2 Resonance production**

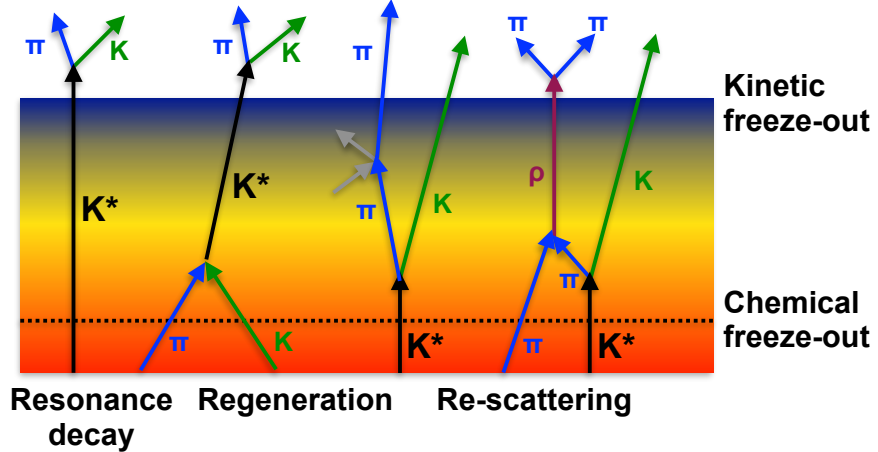


Figure 11: Hadronic phase

588 Resonances are particles with larger mass than the corresponding its ground state  
 589 particle which has the same quark content. Because of the hadronic resonances decay  
 590 strongly in the medium, it has short lifetime( $\tau$ ) in the order of few fm/c which is comparable  
 591 to the lifetime of the fireball. The natural width of resonances is  $\Gamma = \bar{h}/\tau$ , which is inverse  
 592 proportion to the lifetime. In heavy ion collisions, the hadronic resonances are created in

593 medium which is still expanding so that the particles could interact with the medium and  
594 decay while traveling it. The particles can be measured only via reconstruction of their  
595 decay products in a detector, since it decays very shortly after being produced.

596 The effects which can be happened in the hadronic phase is shown in Figure 11. In the  
597 left on the figure, as example, there is sketch of the original resonance decay of  $K^*(892)^0$   
598 ( $K^*(892)^0 \rightarrow \pi + K$ ). It is possible that resonances may be regenerated via pseudo-elastic  
599 scattering of decay products ( $\pi + K \rightarrow K^*(892)^0 \rightarrow \pi + K$ ) in the time duration between the  
600 chemical ( $T_{ch}$ ) and the kinetic freeze-out ( $T_{kin}$ ). Conversely, in case that the decay product  
601 undergo elastic scattering or pseudo-elastic scattering through a different resonance in the  
602 medium, e.g.  $\rho$  in the Figure 11, the invariant mass of the decay products can not mach  
603 that of the parent particle. As a results, yield after kinetic freeze out could be smaller than  
604 the yields originally produced.

605 These effects of re-scattering and regeneration could depend on the lifetime of the  
606 resonances and influence the their integrated yield and momentum spectrum. The yield is  
607 increase if the regeneration dominates, vice versa, it is decrease with re-scattering effect.  
608 In order to understand the properties in hadronic medium, the ratios between resonances  
609 and ground state hadrons have to be studies and the results are compared with model  
610 predictions discussed in Section 2.

## 611 4 A Large Ion Collider Experiment at the LHC

612 ALICE (A Large Ion Collider Experiment) is one of major experiment at LHC (Large  
613 Hadron Collider) in Geneva and it is dedicated experiment for the study of QCD matter  
614 created in high-energy collisions [26]. It has been accumulating data during the whole first  
615 phase of the LHC operation, from end of 2009 to the beginning of the technical shutdown  
616 2013. During that time, the beam energy was tuned to have data in pp collisions at 0.9,  
617 2.76, 7 and 8 TeV, p–Pb collisions at 5.02 TeV and Pb–Pb collisions at 2.76 TeV.

618 The section 4.1 aims to explain the LHC operation of the first phase and includes  
619 each experiments builed in LHC. Next section (4.2.1) focuses on general description of  
620 the ALICE detector and detailed explanation of sub-detectors used in this analysis will  
621 given. And then the particle identification performance is discussed. The Data Acquisition  
622 (DAQ) system and trigger system follow in Section 4.2.2. The last section account for  
623 offline software frame work.

### 624 4.1 The Large Hadron Collider

625 The Large Hadron Collider (LHC) [27] at CERN is the world’s largest particle accelerator.  
626 It provides maximum possible energies of 7 TeV for proton beam and 2.76 per nucleon  
627 for beam of lead ions, hence, providing collisions at  $\sqrt{s} = 14$  TeV and  $\sqrt{s_{NN}} = 5.5$  TeV,  
628 respectively. These energies are largest one ever achieved in particle collision experiment.

629 The LHC is a two ring superconducting hadron accelerator and collider built in the  
630 26.7 kM tunnel. In separate parallel beam pipe, there are two counter-rotating beams  
631 and the bunches of particles in each of them rotate many time up to collision energy is  
632 approached to the desired value. The accelerator keeps to bend the beam around the ring  
633 to maintain focused bunches and enlarge them to their collision energy. In the end, the size  
634 of each bunches turns into minimized to obtain high luminosity guarantee a high number  
635 of collisions per time interval at the collisions points. In order to achieve it, combination  
636 of magnetic and electric field have been performed. In spite of the high luminosity, very  
637 small portion of the particles from two bunches collides in a single bunch crossing. The  
638 others are defocused and continue to rotate the ring.

639 The CERN accelerator complex is shown in the Figure 12. The sequence of injection of  
640 bunches into the LHC is started from acceleration in the LINAC (LINEar ACcelerator )2,  
641 PS (Proton Synchrotron) booster, PS, and SPS (Super Proton Synchrotron) accelerators.  
642 The way to inject of heavy-ion bunches are different. The bunches pass the LINAC3 instead  
643 of LINAC2, LEIR (Low Energy Ion Ring), PS and SPS accelerators [28].

644 The first pp collisions at 900 GeV center of mass energy were delivered by the LHC on  
645 September 10th 2008. Nine days later, the operations were interrupted due to a failure in  
646 an electrical connection between two magnets. The machine operators spent over a year  
647 repairing and consolidating the accelerator. On November, 2009 low energy proton beams  
648 circulated again, and a few days later, by achieving the energy of 1.18 TeV per proton

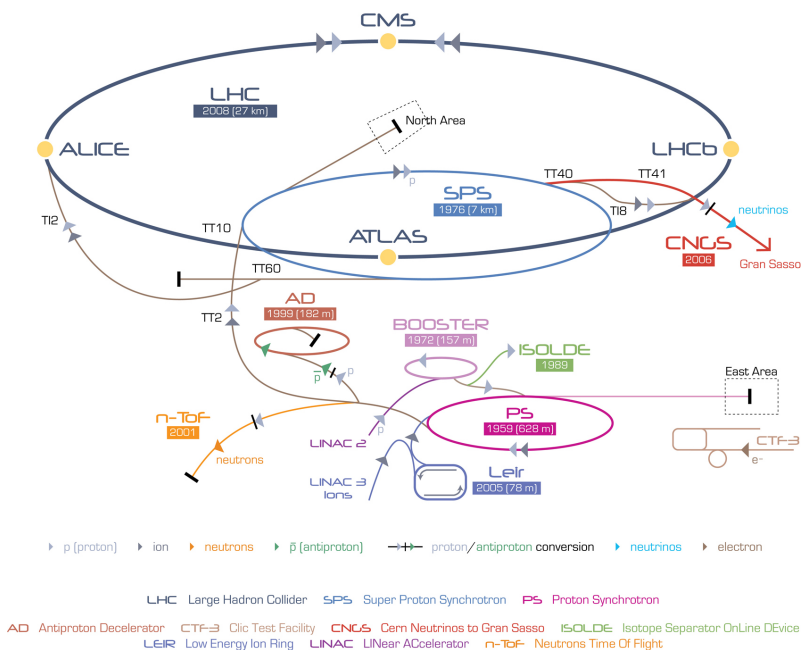


Figure 12: The CERN accelerator complex [3]

beam, LHC became the most powerful accelerator in the world. The first pp collisions at center of mass energy of 7 TeV were delivered in March 2010, and the first Pb–Pb collisions at center of mass energy of 2.76 TeV per nucleon pair in November 2010.

In 2010 the integrated luminosity delivered by the LHC was  $\sim 48 \text{ pb}^{-1}$  for pp collisions at  $\sqrt{s} = 7 \text{ TeV}$  ( $\sim 0.5 \text{ pb}^{-1}$  in ALICE) and  $\sim 10 \mu\text{b}^{-1}$  for Pb–Pb at  $\sqrt{s_{\text{NN}}} = 2.76 \text{ TeV}$  ( $\sim 9 \mu\text{b}^{-1}$  in ALICE) [26]. In 2011 the beam energy was the same as in 2010 both for pp and Pb–Pb. The performance of the LHC improved in terms of luminosity with  $\sim 5.61 \text{ fb}^{-1}$  for pp ( $\sim 4.9 \text{ pb}^{-1}$  in ALICE) and  $\sim 166 \mu\text{b}^{-1}$  for Pb–Pb collisions ( $\sim 146 \mu\text{b}^{-1}$  in ALICE). In 2012, the centre-of-mass energy for pp collisions was brought to 8 TeV and the integrated luminosity (up to December 2012, end of the pp program) was  $\sim 23.3 \text{ fb}^{-1}$  ( $\sim 10 \text{ pb}^{-1}$  in ALICE). A pilot p–Pb run operated at  $\sqrt{s_{\text{NN}}} = 5.02 \text{ TeV}$  on September 2012, followed by a long p–Pb run on February 2013 with a delivered luminosity of  $14 \text{ nb}^{-1}$ . A very short pp run at  $\sqrt{s} = 2.76 \text{ TeV}$  ended the Run1 of the LHC program, marking the start of the first long shutdown (LS1) until the end of 2014.

The LHC produces collisions in four so called Interaction Points (IPs) in correspondence of which are located six detectors of different dimensions and with different goals, all able to study the products of the interactions. These are:

**ALICE (A Large Ion Collider Experiment-IP<sub>2</sub>)** [29] is devoted heavy-ion experiment intended to investigate strongly interacting matter at very high energy density. It explores the phase transition to the QGP phase diagram and its properties. Furthermore, the ALICE study the results of pp and p–Pb collisions, as a reference for heavy-ion measurements. ALICE is able to measure identified particles by using excellent particle identification capability and its acceptance reached to very low transverse momenta.

**ATLAS (A Toroidal LHC ApparatuS-IP<sub>1</sub>) and CMS (Compact Muon Solenoid - IP<sub>5</sub>)** [30][31] are built to cover the widest possible range of physics at the LHC and they are dedicated to collect results from pp collisions. Specific topics are the beyond the Standard Model and serch for the Higgs boson.

**LHCb (The Large Hadron Collider beauty experiment-IP<sub>8</sub>)** [32] is a dedicated experiment for the study of heavy flavor physics at the LHC. In particular, the experiment focuses on the study of CP violation and rare decays of beauty and charm particles, to test the Standard Model and to search for evidence of New Physics. The LHCb physics program is complementary to the flavor physics studies and to the direct exploration for new particles performed at ATLAS and CMS.

**TOTEM (TOTal Elastic and diffractive cross-section Measurement-IP<sub>5</sub>)** [33] is dedicated to the measurement of the total pp cross-section, study of elastic and diffractive scattering. The detector is built at the same interaction point of the CMS experiment.

690 **4.2 The ALICE project**

691 The main goal of the ALICE experiment at the LHC [34] is study of matter produced  
692 extreme conditions of temperature and energy density from ultra-relativistic heavy-ion  
693 collisions. The purpose is to inspect the existence of a phase transition from the hadronic  
694 matter to the QGP which was proposed by QCD prediction. Because only ALICE is the  
695 LHC experiment specifically designed for Pb–Pb collisions, it has to be able to cope with  
696 the large multiplicities associated with these collision systems and at the same time has to  
697 cover as many QGP-related observables as possible. ALICE is also interested in the results  
698 of pp interactions, since these are the baseline for the results obtained Pb–Pb collisions. It  
699 is not only crucial for comparison with Pb–Pb but also can be used to tune Monte Carlo  
700 models.

701 In comparison with the other experiments, ALICE is able to provide an excellent Particle  
702 IDentification (PID) performance obtained by combination of different PID techniques  
703 from various detectors that are optimized in different momentum ( $p$ ) regions.

704 **4.2.1 ALICE detector**

705 ALICE is a complex of 14 detector subsystems (Figure 13) that can be categorized in three  
706 groups:

707

708 **Central detectors** are installed in a solenoid magnet which gives 0.5 T magnetic field  
709 and covered pseudo-rapidity interval is  $-0.9 < \eta < 0.9$  (corresponding to a polar accept-  
710 tance  $\pi/4 < \theta < 3\pi/4$ ). The acceptance in azimuthal angle is  $2\pi$ . The central detectors  
711 are mainly used to vertex reconstruction, tracking, particle identification and momentum  
712 measurement. From interaction region to outward region of detector, there are several  
713 detectors explained below:

- 714 • Inner Tracking System (ITS)
- 715 • Time Projection Chamber (TPC)
- 716 • Transition Radiation Detector (TRD)
- 717 • Time Of Flight (TOF)

718 Following three detectors have limited azimuthal acceptance in the mid-rapidity region:

- 719 • High Momentum Particle Identification Detector (HMPID)
- 720 • PHOton Spectrometer (POHS)
- 721 • ElectroMagnetic CALorimeter (EMCAL)

722       **Muon spectrometer** is located in the forward pseudo-rapidity region ( $-4.0 < \eta <$   
723       $-2.5$ ) and is made up of a dipole magnet and tracking and trigger chambers. It has been  
724      optimized and configured to extract single muons and to reconstruct heavy quark reso-  
725      nances (such as  $J/\Psi$  through their  $\mu^+\mu^-$  decay channel).

726

727       **Forward detectors** are placed in the high pseudo-rapidity area (small angles with  
728      respect to the beam pipe). They are used to measure global event characteristics and for  
729      triggering.

- 730       • Time Zero (T0) measures the time of events with precision of the order of tens of  
731      picoseconds, as needed by TOF.
- 732       • VZERO (V0) rejects the backgrounds coming from beam-Gas interaction and trigger  
733      minimum bias events.
- 734       • Forward Multiplicity Detector (FMD) gives multiplicity information and it covers  
735      large fraction of the solid angle ( $-3.4 < \eta < -1.7$  and  $1.7 < \eta < 5$ ).
- 736       • Photon Multiplicity Detector (PMD) measures the spatial distribution of photons on  
737      an event-by-event basis in  $2.3 < \eta < 3.7$  region.
- 738       • Zero Degree Calorimeter (ZDC) is used to measure and trigger on the impact param-  
739      eter. The ZDC consists of two calorimeters, one for neutrons (ZDC:ZN) and another  
740      one for protons (ZDC:ZP), and includes also an electromagnetic calorimeter (ZEM)

741       The ALICE global coordinate system [35] is a right-handed orthogonal Cartesian system  
742      with the origin X, Y, Z = 0 at the centre of the detector. The three Cartesian axes are  
743      defined as follows: the X axis pointing towards the center of the LHC, the Y axis pointing  
744      upward and the Z axis parallel to the local mean beam line pointing in the direction opposite  
745      to the muon spectrometer. The azimuthal angle increases counter-clockwise from the  
746      positive X axis ( $\Phi = 0$ ) to the positive Y axis ( $\Phi = \pi/2$ ) with the observer standing at  
747      positive Z and looking at negative Z; the polar angle increases from the positive Z axis ( $\theta$   
748      = 0) to the X-Y plane ( $\theta = \pi/2$ ) and to the negative Z axis ( $\theta = \pi$ ).

749       In the following Sections more specific descriptions of the detectors used in the identi-  
750      fication of the  $\Xi(1530)^0$  baryons and in the determination of the characteristics of typical  
751      collisions will be given.

752

### 753       ITS

754       The ITS [34] (Figure 14) is the barrel detector which is closest to the beam pipe. Its main  
755      purposes are:

- 756       • to contribute to the global tracking with the TPC by improving the angle and mo-  
757      mentum resolution

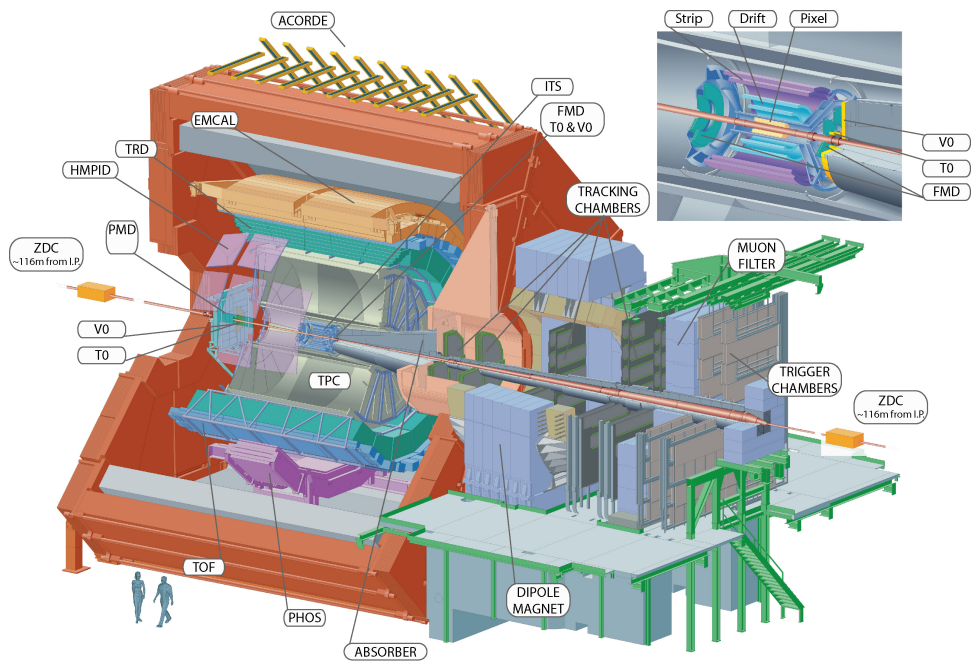


Figure 13: The ALICE detector

- 758     • to reconstruct the position of the primary interaction vertex
- 759     • to reconstruct strange particle decays and secondary vertices from decays of heavy-
- 760        flavor
- 761     • to track and identify particles with momentum below  $100 \text{ MeV}/c^2$
- 762     • to improve the momentum, impact parameter and angle resolution for the measure-
- 763        ment of high  $p_T$  particles performed with the TPC
- 764     • to reconstruct particles traversing dead regions of the TPC

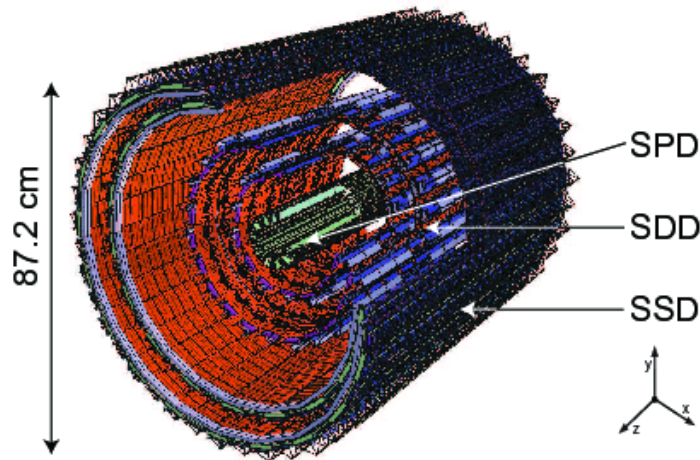


Figure 14: Schematic view of the ITS [4]

765     The ITS encircles the beam pipe which is a  $800 \mu\text{m}$  thickness cylinder shape with an  
 766     outer diameter of  $2.9 \text{ cm}$ . It consists of six layers of silicon detectors placed at radii from  $\sim 4$   
 767     cm to  $\sim 43 \text{ cm}$ . The two innermost layers are Silicon Pixel Detectors (SPD), Silicon Drift  
 768     Detectors (SDD) is placed in middle and the two outmost layers are Silicon micro-Strip  
 769     Detectors (SSD).

770     The amount of material in the detector has to be minimized because the momentum  
 771     and impact parameter resolutions for low momentum particles are dominated by multiple  
 772     scattering effects. The track impact parameter resolution as function of  $p_T$  is shown in  
 773     Figure 15. The ITS detector has a spatial resolution better than  $70 \mu\text{m}$  in the  $(r\phi)$  for  $p_T >$   
 774      $1 \text{ GeV}/c$ .

775

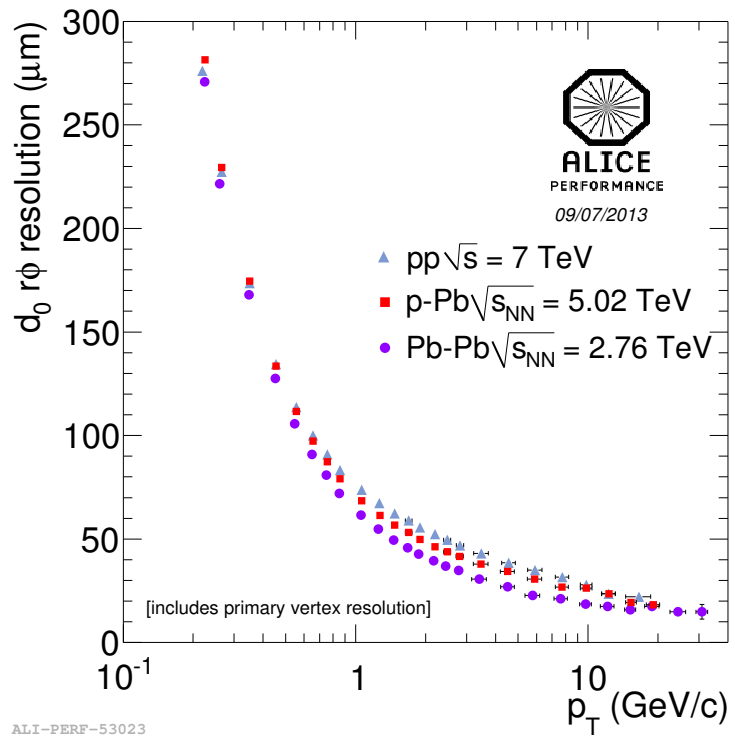


Figure 15: Track impact parameter resolution ( $r\phi$ ) in the transverse plane as function of  $p_T$  for charged particle

776      **TPC**

777

778      The TPC [36] (Figure 16) is the main tracking detector of the central barrel optimized  
779 to measure charged particle momentum with good track separation, particle identification  
780 and vertex determination. In order to get the track in high multiplicity environment of  
781 Pb–Pb collisions, the TPC was designed to have an excellent tracking performance. For  
782 such reason, it was constructed as a drift chamber in 5 m cylindrical shape. The inner  
783 radius is  $r_{in} \sim 85$  cm decided by the maximum acceptable track density and the most outer  
784 radius is  $r_{out} \sim 250$  cm to minimize track length for which  $dE/dx < 10\%$ . The volume  
785 of TPC is  $90 \text{ m}^3$  and it is filled by Ne/CO<sub>2</sub>/N<sub>2</sub>. The readout chambers are installed at  
786 the two endplates of the cylinder. Their design is based on the Multi-Wire Proportional  
787 Chamber (MWPC) technique with pad readout. The TPC has good  $dE/dx$  resolution as  
788 results it is able to identify particles with  $p_T < 1 \text{ GeV}/c$  on a track-by-track basis.

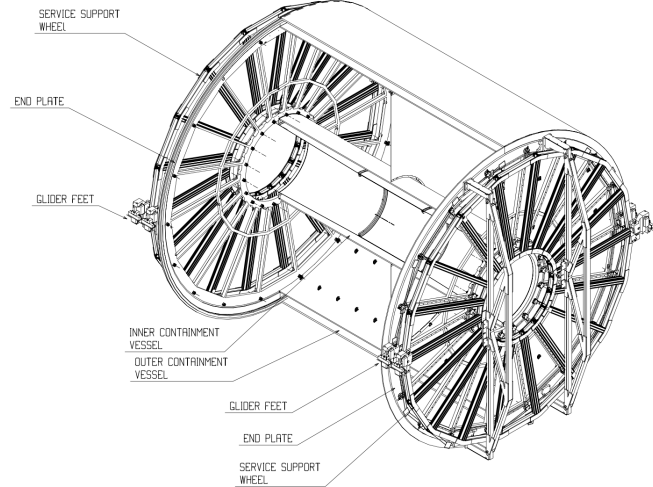


Figure 16: Schematic view of the TPC

789      The gas in the detector is ionized by charged particle traveling through the TPC. The  
790 measurement of this loss of energy is what we need to identify a particle. The physics  
791 observable in this case is the energy loss per unit length, within the matter crossed by  
792 the charged particle, which we call specific energy loss, also denoted by  $dE/dx$ . This  
793 is described by the Beth–Bloch equation, 5, that highlights the key of the identification  
794 technique: this observable depends only on the charge and on velocity ( $\beta$ ) of the particle,  
795 which, in turn, depends only on the momentum and the mass of the ionizing particle.  
796 Since momentum is already known due to track curvature and charge is unitary for most  
797 measured tracks, measuring the  $dE/dx$  allows us to indirectly determine mass and thus

798 determine the particle species. The Bethe-Bloch equation gives the mean specific energy  
 799 loss:

$$-\langle \frac{dE}{dx} \rangle = k_1 \cdot z^2 \frac{Z}{A} \cdot \frac{1}{\beta^2} \left[ \frac{1}{2} \ln(k_2 \cdot m_e c^2 \cdot \beta^2 \gamma^2) - \beta^2 + k_3 \right] \quad (5)$$

800 where  $\beta\gamma = p/Mc$  and: Z: atomic number of the ionized gas (in this case Ne/CO<sub>2</sub>/N<sub>2</sub>)  
 801 A: mass number of the ionized gas (g/mol)  
 802  $m_e$ : electron mass  
 803 z: electric charge of the ionizing particle in unit of electron charge e  
 804 M: ionizing particle mass  
 805 p: ionizing particle momentum  
 806  $\beta$ : ionizing particle velocity normalized to the light velocity c  
 807  $\gamma = 1/\sqrt{1 - \beta^2}$ , Lorentz factor  
 808 k<sub>1</sub>, k<sub>2</sub>, k<sub>3</sub>: constants depending on the ionized medium  
 809

810 For a given ionizing particle mass hypothesis, a given momentum and a given length  
 811 of the trajectory in the ionizing medium, the total charge deposited along the trajectory  
 812 is subject to statistical fluctuations. This random variable follows a Landau distribution,  
 813 that give us the opportunity to measure the mean value  $hdE/dx$ . The long tail of the  
 814 Landau distribution is usually truncated at 50%-70% of the collected signal.

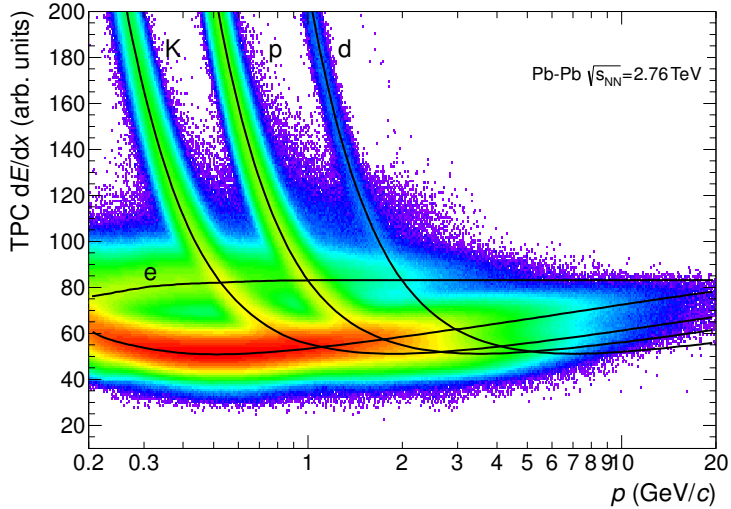


Figure 17: Specific energy loss ( $dE/dx$ ) in the TPC as a function of momentum in Pb–Pb collisions at  $\sqrt{s_{NN}} = 2.76$  TeV. The lines show the parameterizations of the expected mean energy loss.

815 The specific energy loss in the TPC as a function of momentum is shown in Figure

816 17. The different bands characteristic for  $e^\pm$ ,  $\pi^\pm$ ,  $K^\pm$ ,  $p^\pm$  are clearly visible. These  
 817 are the evidence of the statistical distribution of the measured energy loss around the  
 818 expected mean value. The expected value correspond to the prediction by a Bethe–Bloch  
 819 experimental parametrization (superimposed as black lines in the Figure). For a track  
 820 within the TPC the relevant quantity to be considered for PID is the difference between  
 821 the specific energy loss measured by detector and the corresponding predicted value, by  
 822 the Bethe-Bloch parametrization for a given measured momentum. If normalized to the  
 823 resolution of the  $dE/dx$  measurement in the TPC, this difference could be expressed in  
 824 number of  $\sigma$ (see Equation 6). In this way it is possible to estimate more quantitatively the  
 825 goodness of a mass hypothesis. This also gives us the possibility to choose the strictness  
 826 we want to adopt in the identification of a particle ( $n_\sigma$  ,  $n = 2, 3, 4$ ):

$$n_\sigma = \frac{(dE/dx)_{measured} - (dE/dx)_{Bethe-Bloch}}{\sigma_{TPC}} \quad (6)$$

## V0

827 The VZERO detector [37] consists of two segmented arrays of plastic scintillator counters,  
 828 called VZERO-A and VZERO-C, placed near the beam-pipe on each side of the interaction  
 829 point: one at  $Z = 340$  cm, covering the pseudo-rapidity range ( $2.8 < \eta < 5.1$ ), and the  
 830 other at  $Z = -90$  cm in front of the absorber, covering the pseudo-rapidity range ( $-3.7 < \eta <$   
 831  $-1.7$ ).

832 By measuring the relative time of flight, the VZERO reject background from beam-gas  
 833 collisions. (see, Figure 19) The time of flight of particles coming from the interaction point  
 834 to the VZERO-A is  $\sim 11$  ns while VZERP-C is 3 ns. If the beam-gas collision takes place  
 835 outside the region between the two arrays, particles arrive 6 ns before or after the time of a  
 836 beam-beam collisions. When the beam-gas collision takes place outside the region between  
 837 the two arrays, particles arrive 6 ns before or after the time of a beam-beam collision as  
 838 shown in Figure ???

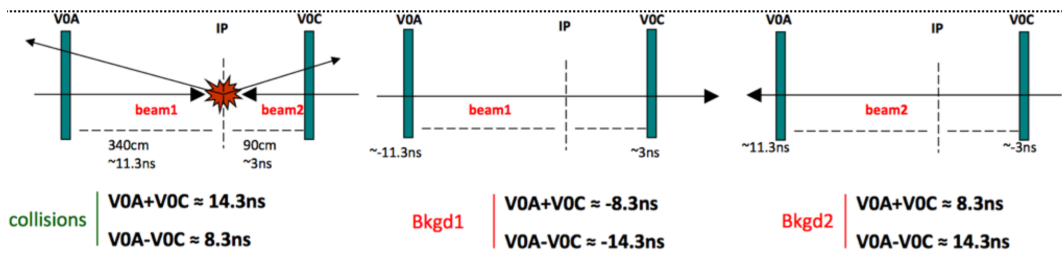


Figure 18: Sketch of events collisions at (8.3 ns, 14.3 ns) is shown in left, background from Beam 1 at (-14.3 ns, -8.3 ns) in in middel and background from Beam 2 at (14.3 ns, 8.3 ns) is in right.

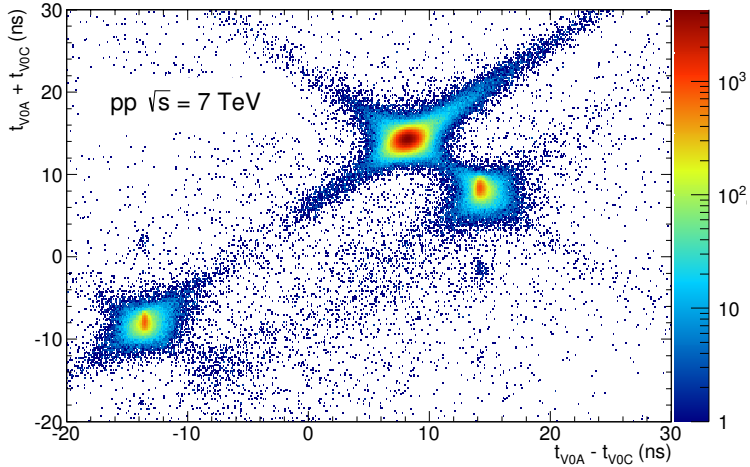


Figure 19: Correlation between the sum (y-axis) and difference (x-axis) of signal times in V0A and V0C. The signals in center come from beam-beam interactions, the signal in left is background from Beam1 and background from Beam2 is shown in right hand.

As the VZERO is a trigger detector, it will provide a minimum-bias trigger for all colliding systems to the central barrel detectors and different centrality triggers in p–Pb and Pb–Pb collisions (e.g. multiplicity, central and semi-central).

The first parameter to be determined in A–A(p–A) collisions is the centrality(multipliciy). This is defined according to the value of the impact parameter,  $b$ , and provides a geometrical scale of the overlapping region between the colliding nuclei: a collision will be defined from central to peripheral, as the impact parameter increases. The centrality of a collision is not directly available and must be deduced from a combination of experimentally measured quantities and Monte Carlo simulations.

The charged-particle multiplicity  $N_{ch}$  is observable that can be measured and used as centrality estimator and it is related to  $N_{part}$ . The variables increase significantly increasing the centrality of the collisions. Another measurable quantity to estimate the centrality is the zero-degree energy EZDC, namely the energy carried by spectator nucleons  $N_{spec} = 2A - N_{part} = E_{ZDC}/E_A$ , where  $E_A$  is the beam energy per nucleon. Typically a measured distribution of one of the previous observables is mapped to the corresponding distribution obtained from phenomenological Glauber calculations. The Glauber model [38, 39] uses a semi-classical approach: the A–A collision is assumed to be an incoherent superposition of  $N$  elementary nucleon- nucleon collisions. The main parameters of the model are the inelastic nucleon-nucleon collision cross-section  $\sigma_n$  and the nuclear density distribution  $\rho(r)$ . In practice, the simulated distribution well reproduce the measured distribution or

860 the latter is fitted with an analytical function. The experimental distribution can then  
861 be divided in classes with sharp cuts on the measured observable ( $E_{ZDC}$ ,  $E_T$  or  $N_{ch}$ ).  
862 These "centrality" classes will correspond to well defined percentage of the integral of the  
863 distribution. A given centrality class in the measured distribution, corresponds to the  
864 same class in the simulated distribution, where the main geometrical variables ( $N_{part}$ ,  $N_{coll}$   
865 and  $T_{AA}$ ) can be determined. The number of classes that can be defined depends on the  
866 resolution achievable on the selection variable. In the analysis described in this thesis  
867 the centrality(multiplicity) estimation is based on the measurement of the multiplicities  
868 from the VZERO scintillators [40][41]. This is the method that achieve the best centrality  
869 resolution: it ranges from 0.5% in central to 2% in peripheral collisions. Other methods,  
870 as the ones based on the  $E_{ZDC}$  measurement or based on the estimate of the number of  
871 tracks in the SPD or TPC, are used to asses a systematic uncertainty on the centrality  
872 determination. The distribution of the VZERO amplitudes is shown in Figure 20 where  
873 the centrality(multiplicity) percentiles are also indicated.

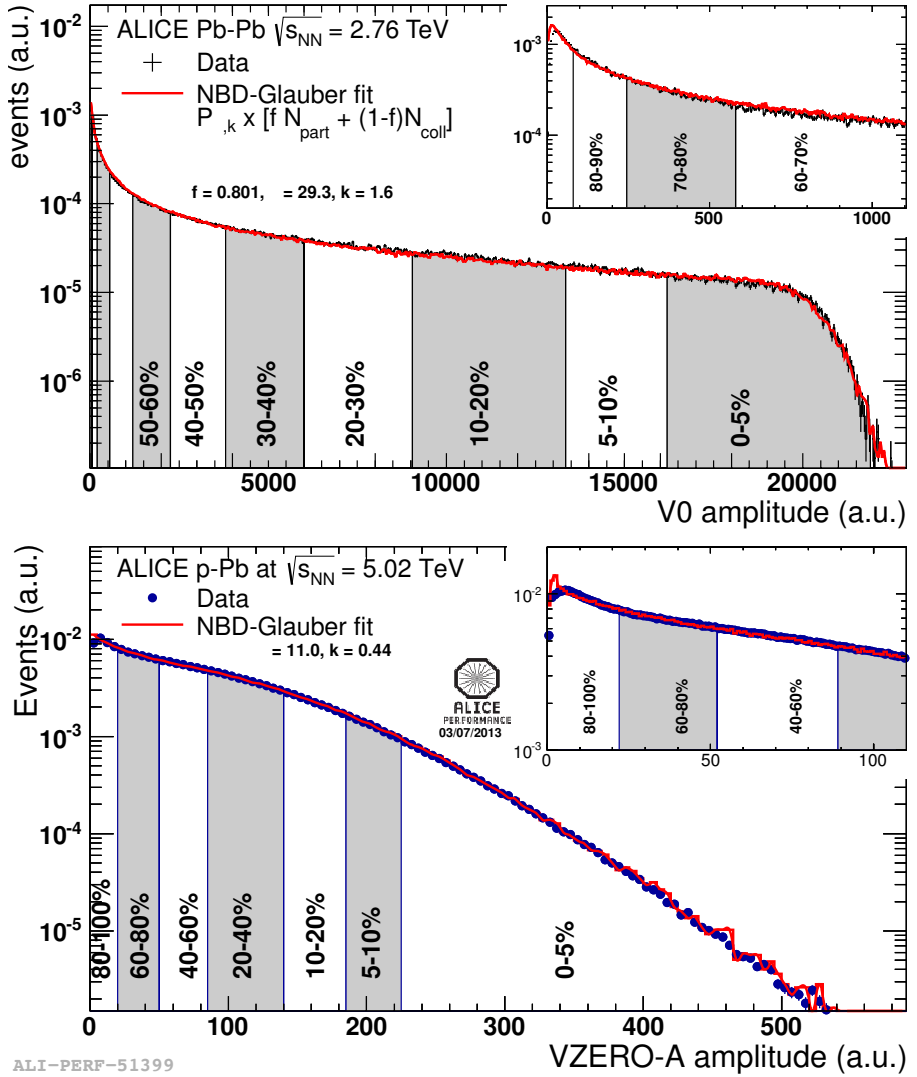


Figure 20: Sum of V0A and V0C amplitude distribution in top and V0A amplitude distribution in bottom.

874 **4.2.2 Data Acquisition (DAQ) and trigger system**

875 The architecture of data acquisition is shown in Figure 21. The tasks of the ALICE DAQ  
 876 system are the assembly of event informations from individual detectors into complete  
 877 events (event building) as well as buffering and export of assembled events to permanent  
 878 storage.

879 The DAQ is geared to accumulate a data rate up to 1.25 GB/s in heavy-ion runs. The  
 880 event is builded in several procedures. Data from each detectors is received by Detector  
 881 Data Links (DDLs) on Local Data Concentrators (LDCs). And the LDCs collect the data  
 882 into sub-events that are then shipped to Global Data Collectors (GDCs). A GDC receives  
 883 all sub-events from a given event and assembles them into a complete event. These events  
 884 are subsequently stored on a system called Transient Data Storage (TDS).

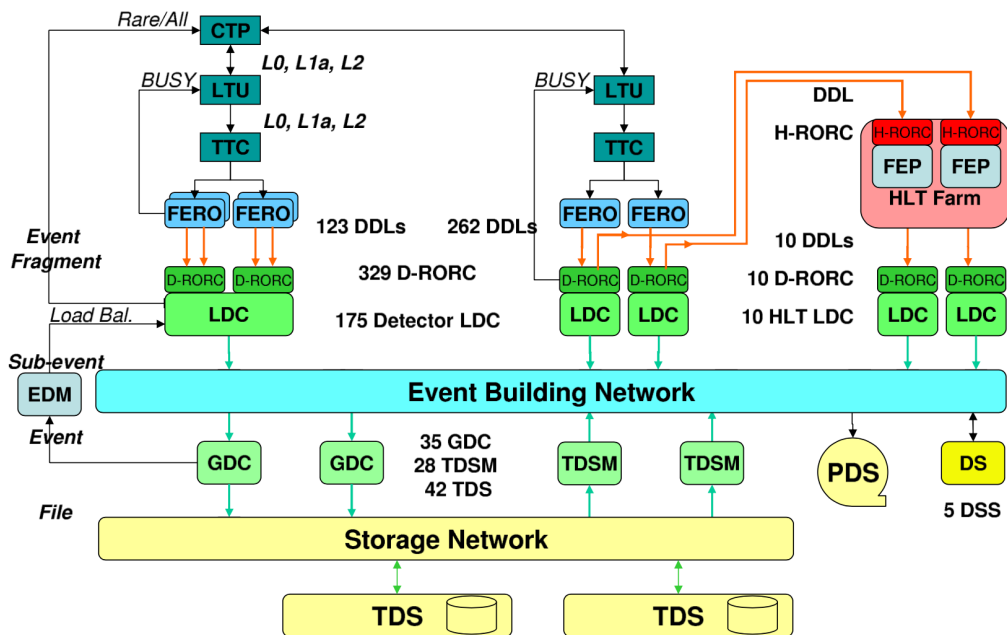


Figure 21: The overall architecture of the ALICE DAQ and the interface to the HLT system.

885 ALICE can simultaneously take data in several partitions, where a set of detectors can  
 886 store their outputs. Since a partition is a group of commonly controlled detectors, a given  
 887 detector can only be active in one partition at a time. The active detectors in a given

partition may be assigned to data taking groups called clusters, for which triggers can be defined.

ALICE has a two-layer trigger architecture [42]. The low-level trigger is a hardware trigger called Central Trigger Processor (CTP). The High-Level Trigger (HLT) is implemented as a pure software trigger. The CTP combines inputs from different trigger sources, namely the various detectors. These inputs are single signals, like a hit in the detector, or, can be the result of fast calculation performed directly in the detectors. The HLT allows the implementation of sophisticated logic for the triggering. In contrast to the CTP which governs the readout of the detectors, the HLT receives a copy of the data read out from the detectors and processes them.

The hardware trigger combines the trigger signals of the various detectors to decide if an event is accepted, that means it is read out and written to disk. Several trigger levels reduce the event rate depending on the input signals. The first level, called L0, is delivered after  $1.2 \mu\text{s}$ , while the second, called L1, after  $6.5 \mu\text{s}$ . The final trigger, L2, is delivered after  $100 \mu\text{s}$ , upon completion of the drift time in the TPC. Only after an L2 trigger the event is finally stored. The rates of different trigger classes are very different. By definition minimum-bias triggers have the highest rate; other triggers that look for rare signals are characterized by much lower rates. In order to cope with different scenarios, downscaling factors can be applied to the trigger classes individually, i.e. only every nth event fulfilling the trigger condition is read out. The total recording rate is limited by the maximum bandwidth of data that can be recorded to disk and tape. The ALICE software trigger, called HLT, is a farm of multiprocessor computers. The aim is to have about 1000 PCs processing the data in parallel allowing an online analysis of the events. A trigger decision comes from the analysis of a more comprehensive set of information than what happens for the hardware trigger, giving the possibility to apply more sophisticated triggers. Examples include triggers on high energy jets or on muon pairs. Furthermore, the HLT can significantly reduce the event size by selecting regions of interest (partial readout of detectors) and by further compression of the data. The HLT receives a copy of the raw data and performs per detector reconstruction, partly aided by hardware coprocessors. Subsequently, the trigger decision is based on the global reconstructed event. In the same step a region of interest can be selected. In the last optional step, if the trigger decision is positive, the data are compressed. The trigger decision, partial readout information, compressed data, and the re- construction output is sent to LDCs and subsequently processed by the DAQ. In terms of the overall DAQ architecture, data sent by HLT is treated like stemming from a detector.

923 **4.2.3 ALICE offline software frame work**

924 In order to reconstruct, analyze the raw data as well as the product simulated events, the  
925 computing power and resources are required. The ALICE uses decentralized computing  
926 system called Grid [43].

927 The Grid paradigm is the unification of resources of distributed computing center,  
928 especially, computing power and storage, to provide them to users all over the World. It  
929 allows to provide their resources to wider community and the makes local resources to be  
930 shared with entire collaboration. Software which is implements the Grid is called Grid  
931 middleware. ALICE has developed a Grid middleware called AliEn [44] that is set of tools  
932 and services. An ALICE user employs AliEn to connect to the ALICE Grid which is  
933 composed of a combination of general services that are provided by many Grid middleware  
934 solutions and ALICE-specific services provided by AliEn. Parts of the ALICE Grid are:  
935 i) a global file catalog that is a directory of files in storage elements distributed over the  
936 Globe, ii) the automatic matching of jobs for execution to a suitable location in one of  
937 the connected sites, iii) a shell-like user interface and iv) API9 services for the ROOT  
938 framework [45].

939 AliRoot [34] is the offline framework for simulation, alignment, calibration, reconstruction,  
940 visualization, quality assurance, and analysis of experimental and simulated data. It  
941 is based on the ROOT framework. Most of the code is written in C++ with some parts  
942 in Fortran that are wrapped inside C++ code. Re-usability and modularity are the basic  
943 features of the AliRoot framework. Modularity allows parts of the code to be replaced,  
944 with minimum or no impact on the rest (for example changing the event generator, the  
945 transport Monte Carlo or the reconstruction algorithms). This is achieved implementing  
946 abstract interfaces. In addition codes for each detector subsystem are independent modules  
947 with their specific code for simulation and reconstruction and the code can be developed  
948 concurrently with minimum interference. Re-usability is meant to maintain a maximum  
949 amount of backward compatibility as the system evolves.

950 The central module of the AliRoot framework is STEER (Figure 22) which provides  
951 several common functions such as: steering of program execution for simulation, reconstruc-  
952 tion and analysis; general run management, creation and destruction of data structures,  
953 initialization and termination of program phases; base classes for simulation, event genera-  
954 tion, reconstruction, detectors elements. For event simulation the framework provides the  
955 following functionality:

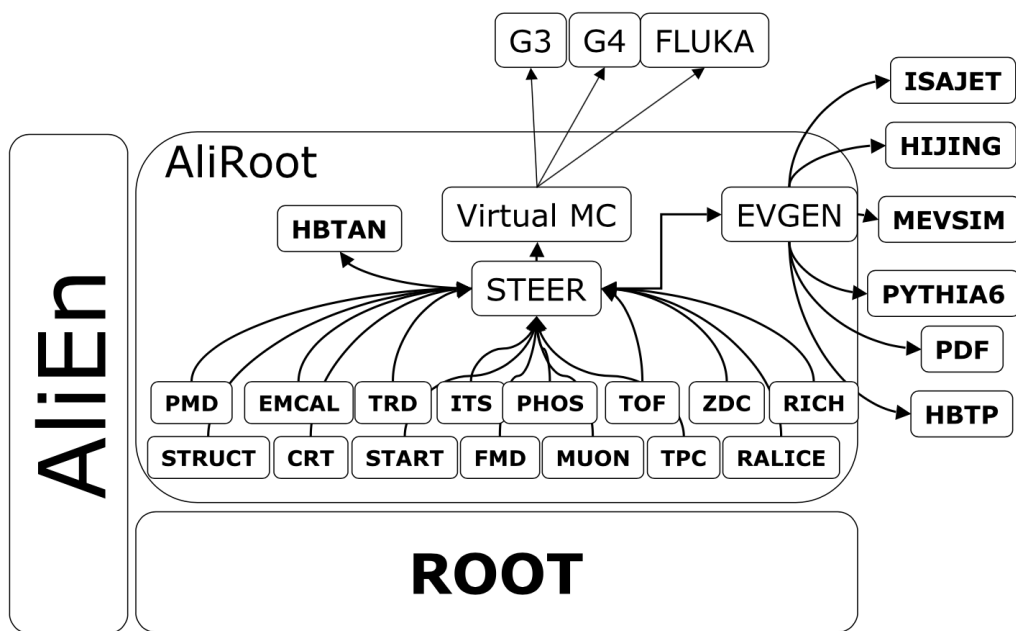


Figure 22: Schematic view of the AliRoot framework

956 **5 Measurement of  $\Xi(1530)^0$  production in p–Pb and Pb–Pb**

957 The measurement of hyperon resonance production in p–Pb collisions helps to disentangle  
958 cold nuclear matter effects from genuine hot medium effects and contribute to the study of  
959 the system size dependence of re-scattering and regeneration in the hadronic phase. And  
960 the measurement in ultra-relativistic heavy-ion collisions such as Pb–Pb collisions, allows  
961 to study the properties of hadronic medium and different stage of its evolution. In order to  
962 study the particle production mechanism in the hadronic phase between the chemical and  
963 kinetic freeze-out, the  $\Xi(1530)^0$  resonance at mid-rapidity ( $-0.5 < y_{\text{CMS}} < 0$ ) is measured  
964 in p–Pb collisions  $\sqrt{s_{\text{NN}}} = 5.02$  TeV and in Pb–Pb collisions with  $|y| < 0.5$  at  $\sqrt{s_{\text{NN}}} = 2.76$   
965 TeV with the ALICE by the reconstruction of hadronic decay into  $\Xi\pi$ .

966 **5.1  $\Xi(1530)^0$  -reconstruction**

967 The  $\Xi^{*0}$  production in p–Pb and Pb–Pb collisions at mid-rapidity has been studied in  
968 different multiplicity and centrality classes, from peripheral to central collisions including  
969 minimum bias events. The analysis is based on the invariant mass of the reconstructed  
970 pairs which might be the decay of a  $\Xi^{*0}$  baryon into charged particles. The daughter  
971 particles which are decay products are identified as oppositely charged  $\Xi$  and  $\pi$  among the  
972 tracks reconstructed in the central barrel. In section 5.1.1, the event selection and track  
973 selection applied in this analysis, and the particle identification is explained. Then, the raw  
974 yield from signal is extracted by integrating the fit on the background-subtracted invariant  
975 mass distribution of  $\Xi\pi$  in several transverse momentum. To obtain the corrected  $p_{\text{T}}$ -  
976 spectra, the raw yields are corrected for acceptance and efficiency ( $\text{Acc} \times \epsilon_{\text{rec}})(\text{pt})$  which  
977 is computed using Monte Carlo simulation. By dividing for the number of the events in  
978 each multiplicity and centrality classes, the normalization on the spectra is performed.

979 **5.1.1 Data sample and event selection**

980 A description of the ALICE detector and of its performance during the LHC Run 1 (2010–  
981 2013) can be found in [34, 26]. The data sample in the analysis from Pb–Pb collisions with  
982 energy of  $\sqrt{s_{\text{NN}}} = 2.76$  obtained during 2011 and the sample of p–Pb run at  $\sqrt{s_{\text{NN}}} = 5.02$   
983 TeV was recorded in 2013.

984 Due to the asymmetric energies of the proton (4 TeV) and lead ion (1.57 A TeV) beams,  
985 the centre-of-mass system in the nucleon-nucleon frame is shifted in rapidity by  $\Delta y_{\text{NN}} =$   
986 0.465 towards the direction of the proton beam with respect to the laboratory frame of  
987 the ALICE detector [6]. For the analysed p–Pb data set, the direction of the proton beam  
988 was towards the ALICE muon spectrometer, the so-called “C” side, standing for negative  
989 rapidities; conversely, the Pb beam circulated towards positive rapidities, labelled as “A”  
990 side in the following. The analysis in this paper was carried out at midrapidity, in the  
991 rapidity window  $-0.5 < y_{\text{CMS}} < 0$ .

992        The minimum bias trigger during the p–Pb run was configured to collect events by  
993        requiring a logical OR of signals in V0A and V0C [26], two arrays of 32 scintillator detectors  
994        covering the full azimuthal angle in the pseudo-rapidity regions  $2.8 < \eta_{\text{lab}} < 5.1$  and  
995         $-3.7 < \eta_{\text{lab}} < -1.7$ , respectively [46]. In the data analysis it was required to have a  
996        coincidence of signals in both V0A and V0C to remove the events from single-diffractive  
997        and electromagnetic interactions.

998        Out of this sample in p–Pb collision events about 109.3 million events, 93.9 million  
999        events pass the following selection criteria and have been used for the analysis.

1000        The Pb–Pb collisions data sample was selected by online centrality trigger requiring a  
1001        signal in the forward V0 detectors[41] to record enhanced data in central collision. The  
1002        data consists of 24.8 million events in most central collisions (0-10%), 21.8 million events in  
1003        semi-central collisions (10-50%) and 3.5 million events with minimum-bias trigger (0-90%).  
1004        Among 49.6 million events in total, 43.0 million events have been analyzed as passed the  
1005        criteria below.

- 1006        • Events with z-position of primary vertex ( $V_z$ ) within  $\pm 10$  cm of the center of  
1007        TPC/ITS
- 1008        • Rejection of pile-up event
- 1009        • Requiring primary tracks to have at least one hit in SPD
- 1010        • p–Pb: multiplicity ranges in percentile (V0A): 0-20%, 20-40%, 40-60%, 60-100% and  
1011        MB(0-100%)
- 1012        • Pb–Pb: centrality classes (V0A and V0C): 0-10%, 10-40%, 40-80% and MB (0-80%)

1013        The distribution of the  $V_z$  of the accepted events in p–Pb collision is reported on left  
1014        panel in Figure 23 and corresponding figure but obtained from Pb–Pb collisions is shown  
1015        on right panel in Figure. 23. Events with  $|V_z| < 10$  cm have been used to make ensure  
1016        that the tracks have been obtained from uniform acceptance in the central pseudo-rapidity  
1017        region,  $|\eta| < 0.8$ , where the analysis is performed. This cut reduces the total number of  
1018        events to 97.5 million events, that is the  $\sim 89.2\%$  of the initial sample in p–Pb collisions and  
1019        43.04 million events which is  $\sim 86.8\%$  of the initial sample in Pb–Pb collisions are survived.

1020        Fig. 24 shows the multiplicity distribution of the accepted events in p–Pb collision  
1021        divided in bins of percentile. The each color on the histogram indicate the multiplicity  
1022        ranges used in this analysis. Corresponding events for each multiplicity range are in Table  
1023        8.

1024        The distribution of centrality in each trigger used to select the events in Pb–Pb collision  
1025        is shown in Fig. 25 and the reason why the centrality has step structure is that there are  
1026        three different trigger classes classified by the amplitude threshold on VZERO detector.  
1027        Because the distribution of events as function of centrality is not a flat, this may lead to  
1028        additional bias, in particular when one needs to combine the results from different triggers.

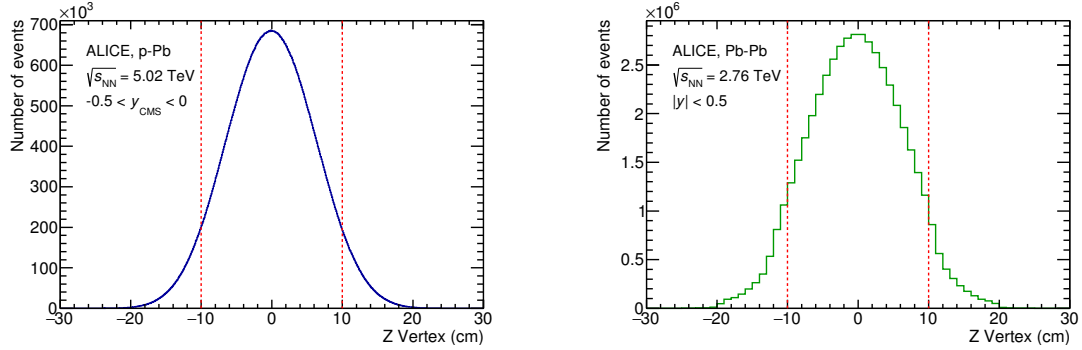


Figure 23: Distribution of vertex-z position from the accepted events in p–Pb collision(Left) and in Pb–Pb collisions(Right). The red dashed line indicates vertex cut

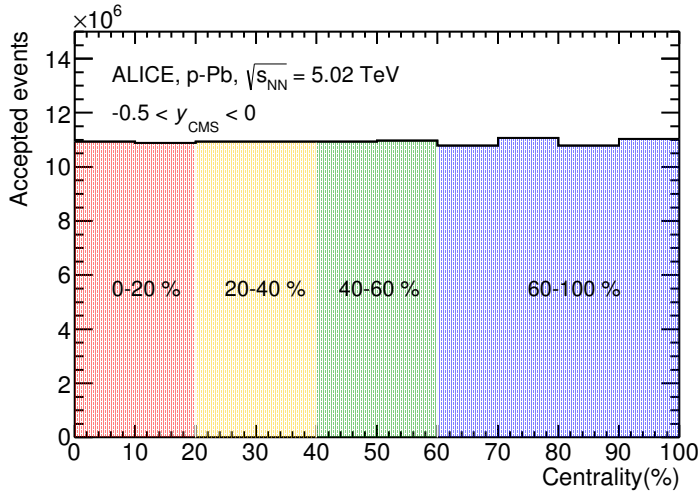


Figure 24: Multiplicity distribution of accepted events in p–Pb collision in percentile. The each color presents the four intervals for the analysis.

1029 For example, events from 40-80% centrality bin have bias with high statistics in 40-60%. In  
1030 order to avoid this effect, we have applied a flattening procedure to have flat distribution  
1031 of events as function of centrality. A brief explanation of the method is below :

- 1032 1. Histograms are obtained for the effective mass distribution in 1% centrality bins and  
1033 for the centrality distribution
- 1034 2. The effective mass distributions are scaled in each 1% centrality bin by a factor:  
1035 Factor = Nevent in 20-40% / 20 / Nevent in current 1% bin
- 1036 3. Each bin in the centrality distribution is scaled using the factor described above
- 1037 4. Histograms are added for centrality bins of interest: 0-10%, 10-40%, 40-80%, 0-80%

1038 The resulting number of events in each centrality classes is summarized in Table 8.

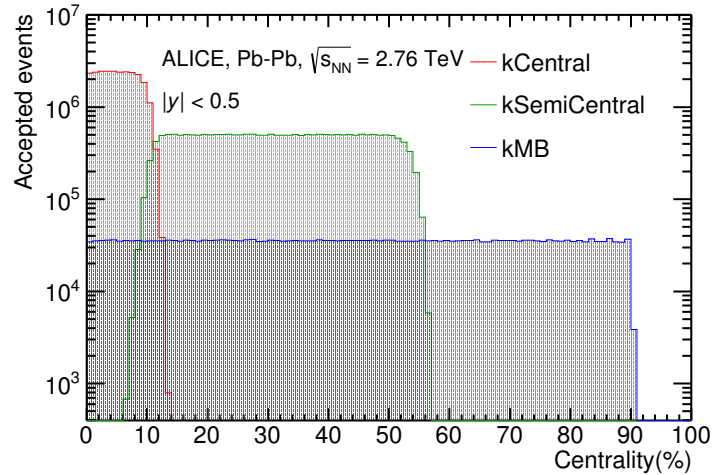


Figure 25: Centrality distribution of three different trigger classes.

Collision	Centrality	Number of events
p-Pb	0-20%	$21.82 \times 10^6$
	20-40%	$21.86 \times 10^6$
	40-60%	$21.91 \times 10^6$
	60-100%	$43.68 \times 10^6$
Pb-Pb	0-10%	$5.58 \times 10^6$
	10-40%	$16.73 \times 10^6$
	40-80%	$22.31 \times 10^6$

Table 8: Number of analyzed events per multiplicity/centrality interval

1039 **5.1.2 Track and topological selection**

1040 In comparison with the  $\Xi^{*0}$  analysis carried out in pp collisions at  $\sqrt{s} = 7$  TeV [8], track  
 1041 and topological selections were revised and adapted to the p-Pb dataset. Pions from strong  
 1042 decays of  $\Xi^{*0}$  were selected according to the criteria for primary tracks. As summarized in  
 1043 Table 9, all charged tracks were selected with  $p_T > 0.15$  GeV/c and  $|\eta_{\text{lab}}| < 0.8$ , as described  
 1044 in Ref. [26]. The primary tracks were chosen with the Distance of Closest Approach (DCA)  
 1045 to PV of less than 2 cm along the longitudinal direction ( $\text{DCA}_z$ ) and lower than  $7\sigma_r$  in  
 1046 the transverse plane ( $\text{DCA}_r$ ), where  $\sigma_r$  is the resolution of  $\text{DCA}_r$ . The  $\sigma_r$  is strongly  
 1047  $p_T$ -dependent and lower than  $100 \mu\text{m}$  for  $p_T > 0.5$  GeV/c [26]. To ensure a good track  
 1048 reconstruction quality, candidate tracks were required to have at least one hit in one of the  
 1049 two innermost layers (SPD) of the ITS and to have at least 70 reconstructed points in the  
 1050 Time Projection Chamber (TPC), out of a maximum of 159. The Particle IDentification  
 1051 (PID) criteria for all decay daughters are based on the requirement that the specific energy  
 1052 loss ( $dE/dx$ ) is measured in the TPC within three standard deviations ( $\sigma_{\text{TPC}}$ ) from the  
 expected value ( $dE/dx_{\text{exp}}$ ), computed using a Bethe-Bloch parametrization [26].

Common track selections	$ \eta_{\text{lab}} $	$< 0.8$
	$p_T$	$> 0.15$ GeV/c
	PID $ (\text{d}E/\text{d}x) - (\text{d}E/\text{d}x)_{\text{exp}} $	$< 3 \sigma_{\text{TPC}}$
Primary track selections	$\text{DCA}_z$ to PV	$< 2$ cm
	$\text{DCA}_r$ to PV	$< 7\sigma_r - 10\sigma_r$ ( $p_T$ )
	number of SPD points	$\geq 1$
	number of TPC points	$> 70$
	$\chi^2$ per cluster	$< 4$

Table 9: Track selections common to all decay daughters and primary track selections  
 applied to the charged pions from decays of  $\Xi^{*0}$ .

1053

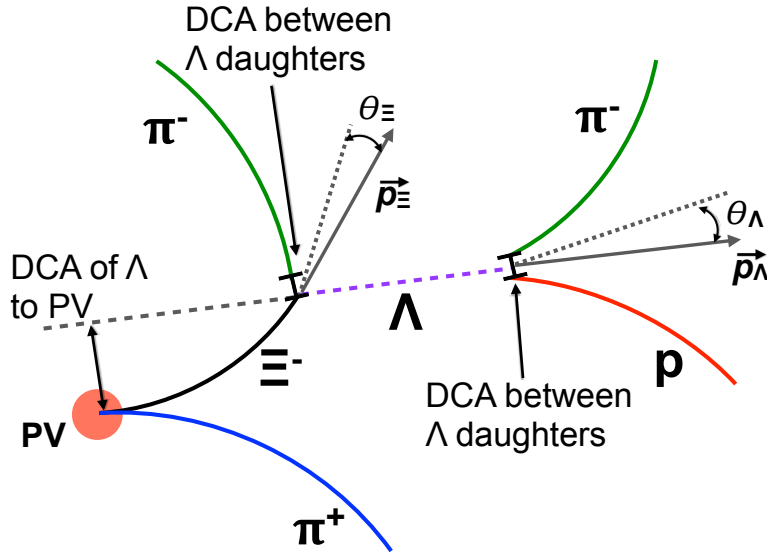


Figure 26: Sketch of the decay modes for  $\Xi^{*0}$  and depiction of the track and topological selection criteria.

1054 Since pions and protons from weak decay of  $\Lambda$  ( $c\tau = 7.89$  cm [1]) and pions from weak  
 1055 decay of  $\Xi^-$  ( $c\tau = 4.91$  cm [1]) are produced away from the PV, specific topological and  
 1056 track selection criteria, as summarized in Table 10, were applied [7, 8, 47].

Topological cuts	p-Pb	Pb-Pb
DCA <sub>r</sub> of $\Lambda$ decay products to PV	$> 0.06$ cm	$> 0.11$ cm
DCA between $\Lambda$ decay products	$< 1.4$ cm	$< 0.95$ cm
DCA of $\Lambda$ to PV	$> 0.015$ cm	$> 0.06$
$\cos\theta_\Lambda$	$> 0.875$	$> 0.998$
$r(\Lambda)$	$0.2 < r(\Lambda) < 100$ cm	$0.2 < r(\Lambda) < 100$ cm
$ M_{p\pi} - m_\Lambda $	$< 7 \text{ MeV}/c^2$	$< 7 \text{ MeV}/c^2$
DCA <sub>r</sub> of pion (from $\Xi^-$ ) to PV	$> 0.015$ cm	$> 0.035$ cm
DCA between $\Xi^-$ decay products	$< 1.9$ cm	$< 0.275$
$\cos\theta_\Xi$	$> 0.981$	$> 0.9992$
$r(\Xi^-)$	$0.2 < r(\Xi^-) < 100$ cm	$0.2 < r(\Xi^-) < 100$ cm
$ M_{\Lambda\pi} - m_\Xi $	$< 7 \text{ MeV}/c^2$	$< 7 \text{ MeV}/c^2$

Table 10: Topological and track selection criteria.

1057 In the analysis of  $\Xi^{*0}$ ,  $\Lambda$  and  $\pi$  from  $\Xi^-$  were selected with a DCA of less than 1.9 cm  
1058 and with a  $DCA_r$  to the PV greater than 0.015 cm. The  $\Lambda$  daughter particles ( $\pi$  and p)  
1059 needs to have a  $DCA_r$  to the PV greater than 0.06 cm, while the DCA between the two  
1060 particles was required to be less than 1.4 cm. The cosine of the pointing angle ( $\theta_\Lambda$ ,  $\theta_\Xi$ )  
1061 and the radius of the fiducial volume ( $r(\Lambda)$ ,  $r(\Xi)$ ) in Table 10 were applied to optimize the  
1062 balance of purity and efficiency of each particle sample.

1063 **5.1.3 Particle identification**

1064 PID selection criteria are applied for

- 1065 1.  $\pi^\pm$  (last emitted  $\pi$ ) and proton from  $\Lambda$
- 1066 2.  $\pi^\pm$  (second emitted  $\pi$ ) from  $\Xi^\pm$
- 1067 3.  $\pi^\pm$  (first emitted  $\pi$ ) from  $\Xi(1530)^0$

1068 by using TPC. On TPC dE/dx versus momentum distribution,  $3\sigma$  cuts are applied to TPC  
 1069 for selecting each of the particles. The TPC dE/dx selection allows to have better signal  
 1070 with  $\sim 20\%$  increase of significance.

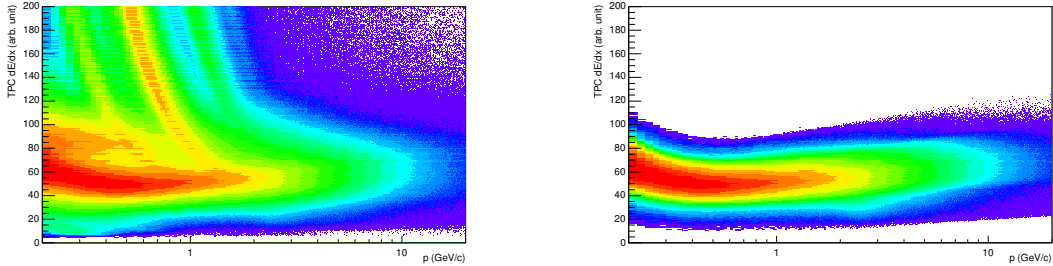


Figure 27: TPC dE/dx as function of transverse momentum in p–Pb collisions for total (Left) and selected first emitted  $\pi$  in  $3\sigma$  (Right)

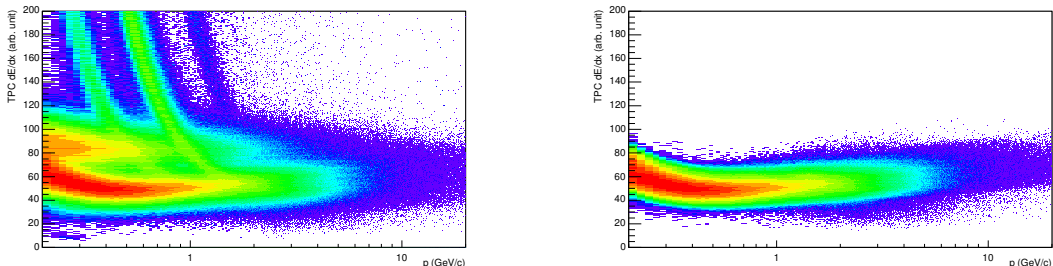


Figure 28: TPC dE/dx as function of transverse momentum in p–Pb collisions for total (Left) and selected second emitted  $\pi$  in  $3\sigma$  (bottom)

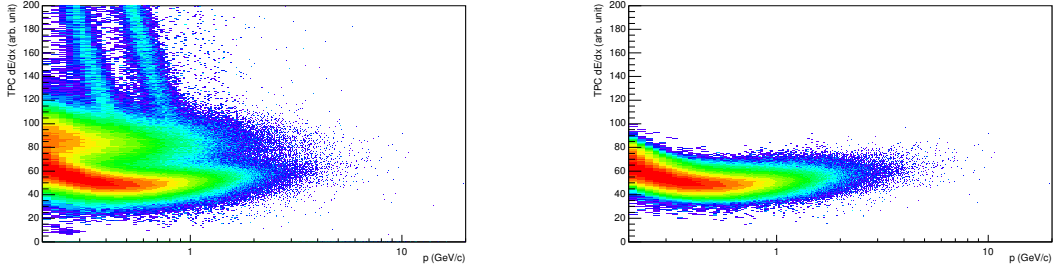


Figure 29: TPC  $dE/dx$  as function of transverse momentum in p–Pb collisions for total (Left) and selected last emitted  $\pi$  in  $3\sigma$ (bottom)

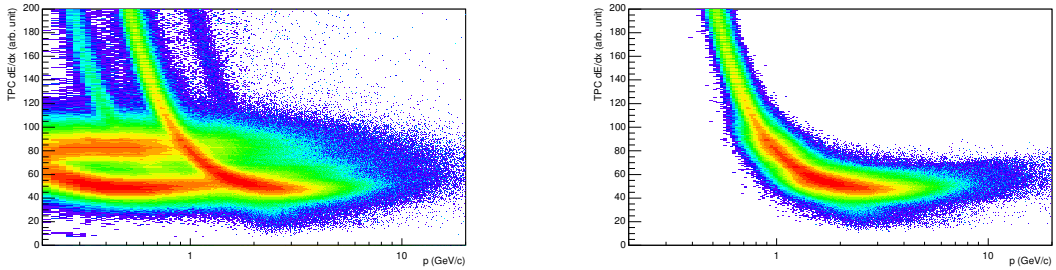


Figure 30: TPC  $dE/dx$  as function of transverse momentum in p–Pb collisions for total (Left) and selected proton in  $3\sigma$ (bottom)

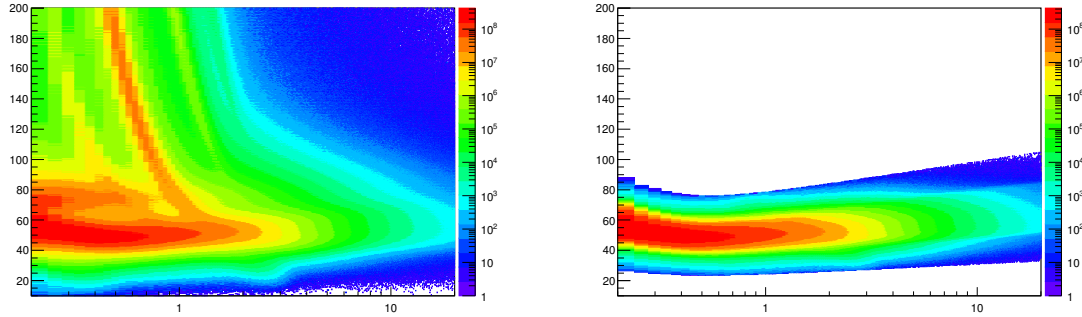


Figure 31: TPC  $dE/dx$  as function of transverse momentum in Pb–Pb collisions for total (Left) and selected first emitted  $\pi$  in  $3\sigma$  (Right)

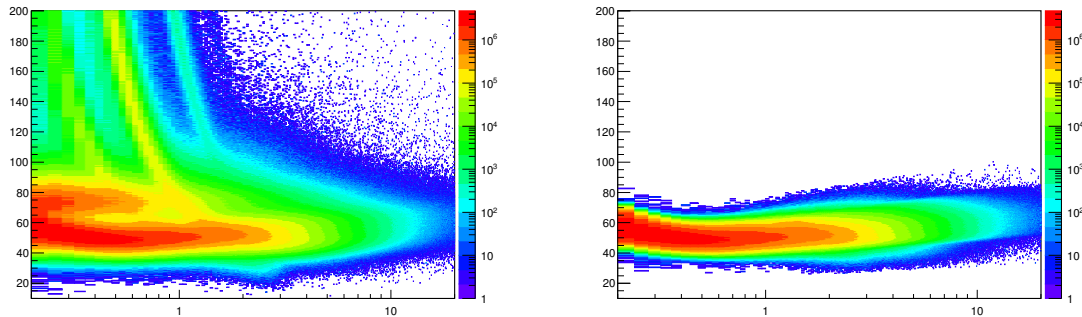


Figure 32: TPC  $dE/dx$  as function of transverse momentum in  $Pb-Pb$  collisions for total (Left) and selected second emitted  $\pi$  in  $3\sigma$  (Right)

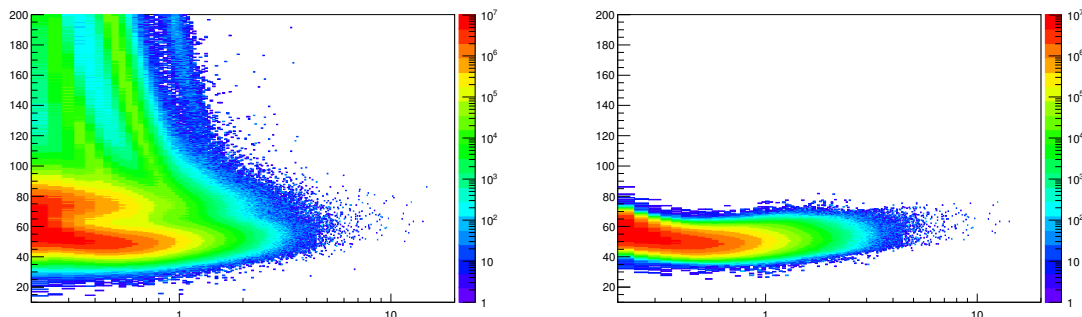


Figure 33: TPC  $dE/dx$  as function of transverse momentum in  $Pb-Pb$  collisions for total (Left) and selected last emitted  $\pi$  in  $3\sigma$  (Right)

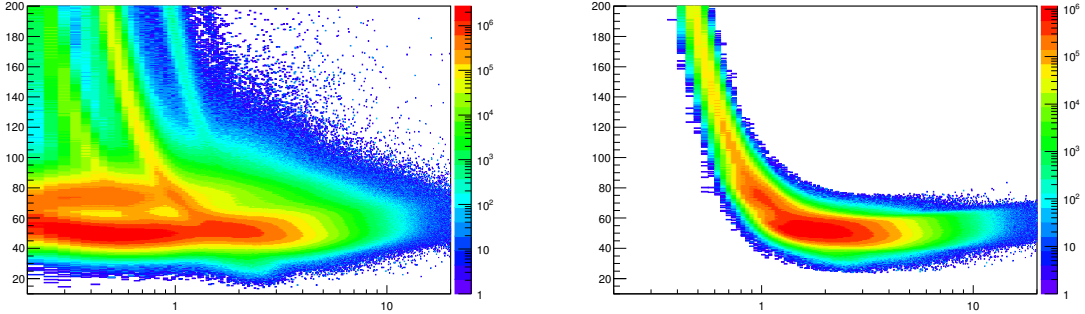


Figure 34: TPC  $dE/dx$  as function of transverse momentum in Pb–Pb collisions for total (Left) and selected proton in  $3\sigma$  (Right)

#### 1071 5.1.4 Signal extraction

1072 The  $\Xi^{*0}$  signals were reconstructed by invariant-mass analysis of candidates for the decay  
 1073 products in each transverse momentum interval of the resonance particle, and for each  
 1074 multiplicity class. The  $\Xi^-\pi^+(\Xi^+\pi^-)$  invariant mass distribution is reported in Figure 5.1.4  
 1075 for semi-central events (20–40%) in p–Pb collisions and Figure 5.1.4 for central events(0–  
 1076 10%) in Pb–Pb collisions.

1077 Since the resonance decay products come from location which is indistinguishable from  
 1078 the PV, a significant combinatorial background is present. In order to extract  $\Xi(1530)^0$   
 1079 signal, it is necessary to reduce the combinatorial background as much as possible. For the  
 1080  $\Xi(1530)^0$  analysis, event mixing (EM) technique has been applied, by combining uncorre-  
 1081 lated decay products 20 different events in p–Pb (5 different events in Pb–Pb).

1082 The events for the mixing have been chosen by applying the similar selection to minimize  
 1083 distortions due to different acceptances and to ensure a similar event structure, only tracks  
 1084 from events with similar vertex positions  $z$  ( $|\Delta z| < 1$  cm) and track multiplicities  $n$  ( $|\Delta n| <$   
 1085 10) were taken.

1086 The mixed-event background distributions were normalised to two fixed regions,  
 1087  $1.49 < M_{\Xi\pi} < 1.51 \text{ GeV}/c^2$  and  $1.56 < M_{\Xi\pi} < 1.58 \text{ GeV}/c^2$ , around the  $\Xi^{*0}$  mass  
 1088 peak (Figure 5.1.4 and 5.1.4). These regions were used for all  $p_T$  intervals and multiplicity  
 1089 classes, because the background shape is reasonably well reproduced in these regions and  
 1090 the invariant-mass resolution of the reconstructed peaks appears stable, independently of  
 1091  $p_T$ . The uncertainty on the normalization was estimated by varying the normalization  
 1092 regions and is included into the systematic uncertainty due to the signal extraction (Sec-  
 1093 tion 5.4).

1094 After the background subtraction, the resulting distribution is shown in Figure 5.1.4  
 1095 and 5.1.4. In order to obtain raw yields, a combined fit of a first-order polynomial for

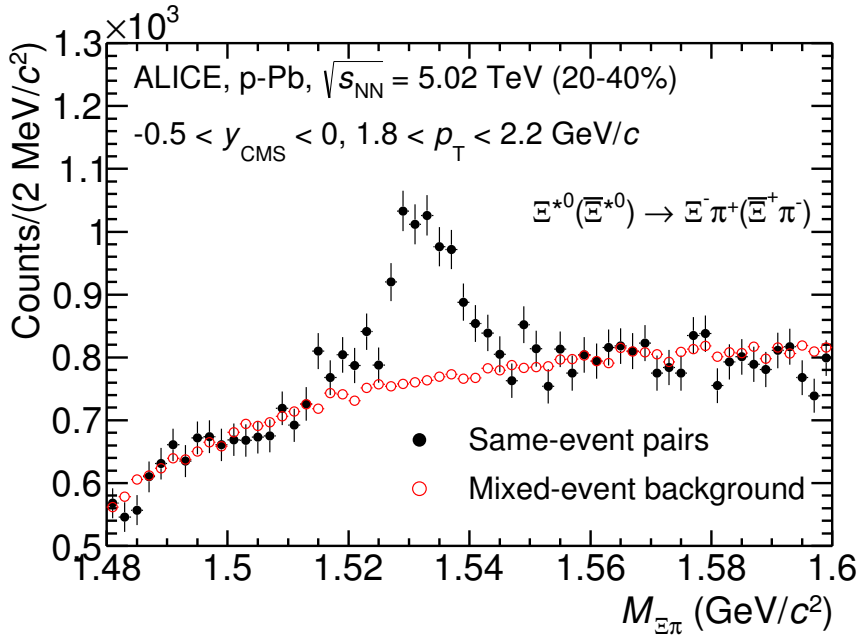


Figure 35: The  $\Xi^\pm\pi^\pm$  invariant mass distribution (Same-event pairs) in  $1.8 < p_T < 2.2 \text{ GeV}/c$  and for the multiplicity class 20-40%. The background shape, using pairs from different events (Mixed-event background), is normalised to the counts in  $1.49 < M_{\Xi\pi} < 1.51 \text{ GeV}/c^2$  and  $1.56 < M_{\Xi\pi} < 1.58 \text{ GeV}/c^2$ .

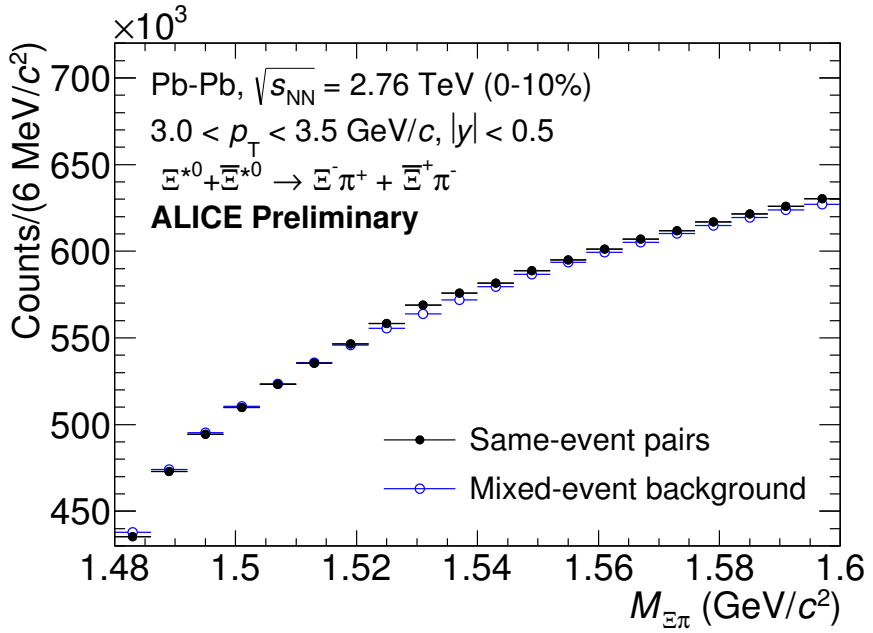


Figure 36: The  $\Xi^\pm\pi^\pm$  invariant mass distribution (Same-event pairs) in  $3.0 < p_T < 3.5$  GeV/c and for the centrality class 0-10%. The background shape, using pairs from different events (Mixed-event background), is normalised to the counts in  $1.49 < M_{\Xi\pi} < 1.51$  GeV/c<sup>2</sup> and  $1.56 < M_{\Xi\pi} < 1.58$  GeV/c<sup>2</sup>.

1096 the residual background and a Voigtian function (a convolution of a Breit-Wigner and a  
 1097 Gaussian function accounting for the detector resolution) for the signal was used. The  
 1098 mathematical form of fit function used in analysis is:

$$f(M_{\Xi\pi}) = \frac{Y}{2\pi} \frac{\Gamma_0}{(M_{\Xi\pi} - M_0)^2 + \frac{\Gamma_0^2}{4}} \frac{e^{-(M_{\Xi\pi} - M_0)/2\sigma^2}}{\sigma\sqrt{2\pi}} + bg(M_{\Xi\pi}) \quad (7)$$

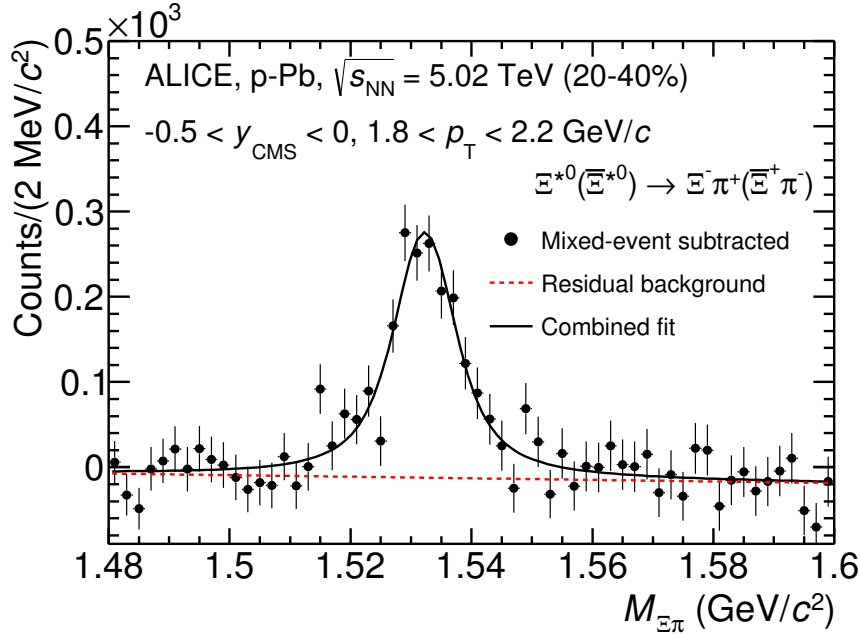


Figure 37: The invariant mass distribution after subtraction of the mixed-event background in p–Pb collisions. The solid curve represents the combined fit, while the dashed line describes the residual background.

1099 The mass parameter of the Voigtian fit ( $M_0$ ) is left free within the fit range ( $1.48 \text{ GeV}/c^2$   
 1100 and  $1.59 \text{ GeV}/c^2$ ). The overall invariant mass width of the Voigtian function is governed  
 1101 by 2 parameters:  $\sigma$  and  $\Gamma_0$ . The  $\sigma$  describes the broadening of the peak due to finite  
 1102 detector resolution while  $\Gamma$  describes the intrinsic width of the resonance itself. The  $\Gamma_0$  is  
 1103 fixed to the PDG value of  $9.1 \text{ MeV}/c$  for the  $\Xi(1530)^0$ . Because of lack of statistics, the  
 1104  $\sigma$  can be over estimated. Therefore the  $\sigma$  parameter is fixed to value derived from  $\sigma$  in  
 1105 MB events which has largest statistics. The  $\sigma$  as function of  $p_T$  distribution in MB events  
 1106 is shown in Figure. 39 and we also report invariant mass of  $\Xi(1530)^0$  as function of  $p_T$  in  
 1107 Figure. 40. The raw yields of  $\Xi(1530)^0$  have been extracted from the Voigtian fit for the 4

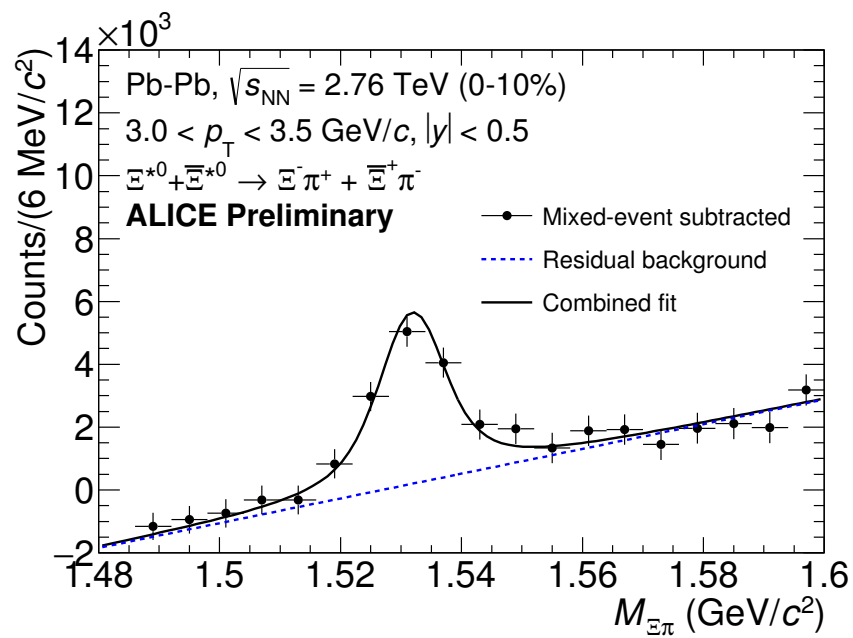


Figure 38: The invariant mass distribution after subtraction of the mixed-event background in Pb–Pb collisions. The solid curve is the combined fit, while the dashed line represents the residual background.

<sub>1108</sub> multiplicity bins (+ NSD events) in p–Pb and 3 centrality bins (+ MB events) in Pb–Pb  
<sub>1109</sub> collisions and the yields as function of  $p_T$  are shown in Figure 41.

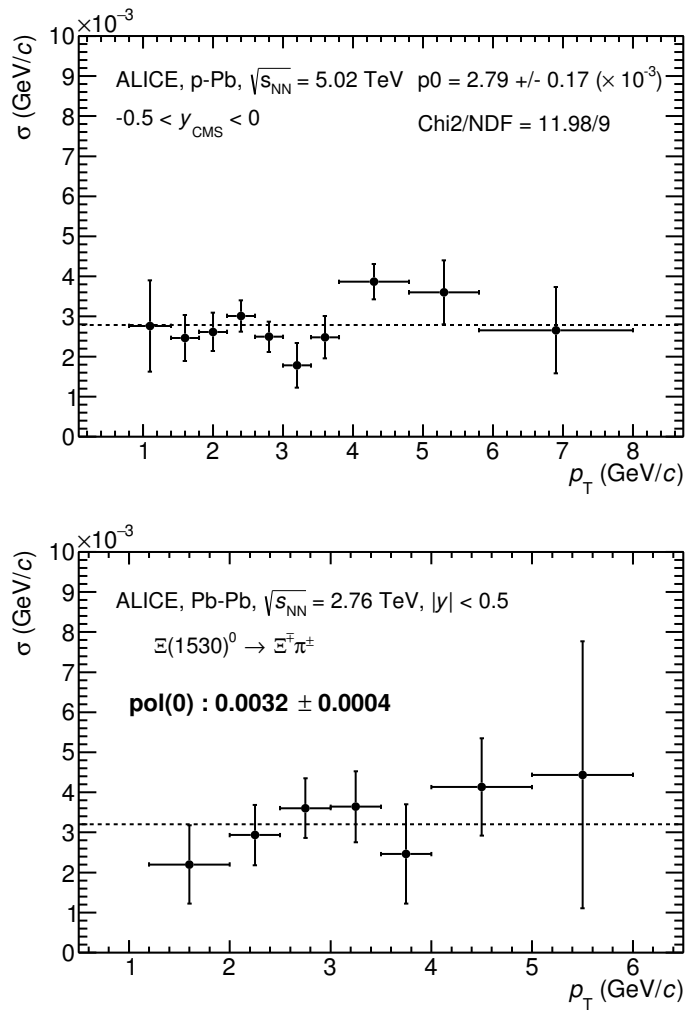


Figure 39:  $\sigma$  fit parameters as a function of  $p_T$  in MB in p–Pb collisions (top) and in Pb–Pb collisions (bottom).

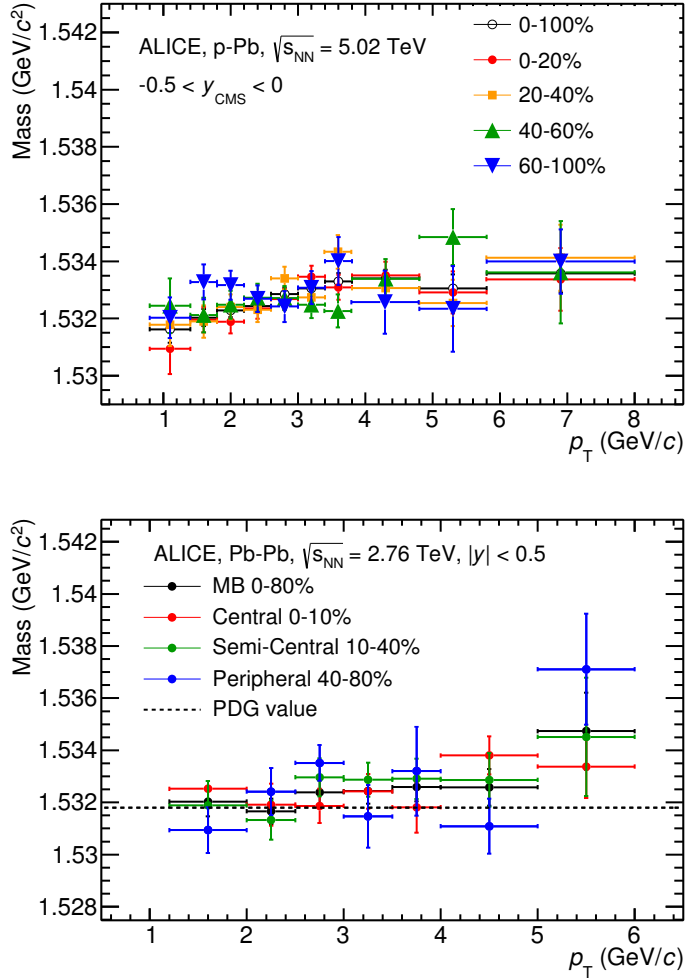


Figure 40:  $\Xi(1530)^0$  mass distribution as a function of  $p_T$  in each multiplicity classes in p–Pb collisions (top) and the different centrality classes in Pb–Pb (bottom). The mass values are obtained from fit of the Voigtian function.

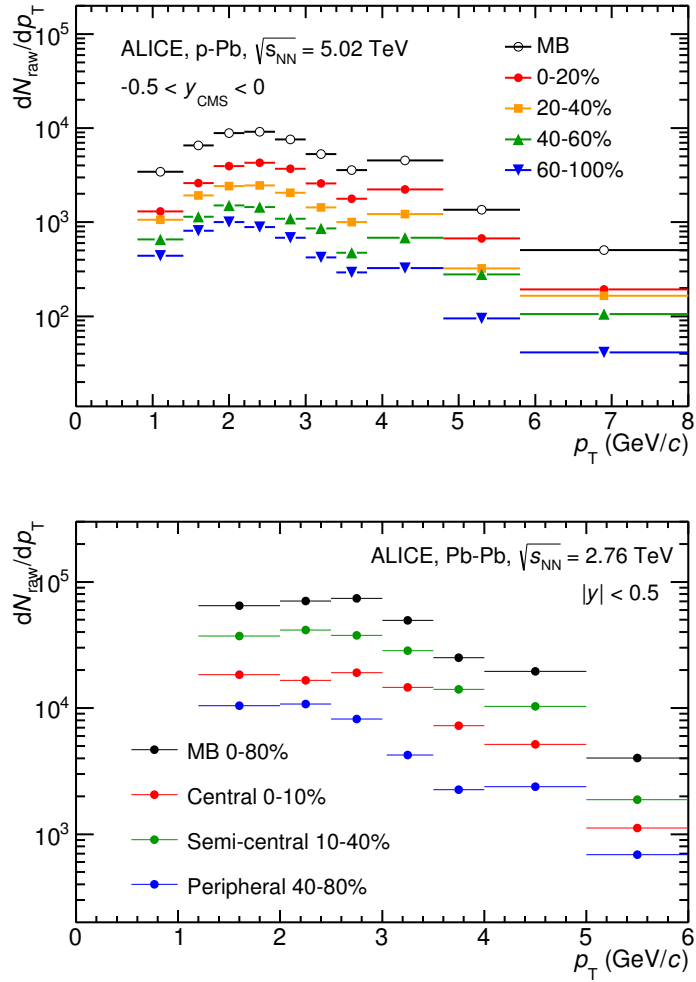


Figure 41: The raw spectra of  $\Xi(1530)^0$  obtained by integrating the Voigtian fit function for different multiplicities in p-Pb collisions (top) and Pb-Pb collisions (bottom). Only the statistical error is reported.

1110 **5.2 Efficiency correction**

1111 The raw yields were corrected for the geometrical acceptance and the reconstruction efficiency  
 1112 ( $A \times \epsilon$ ) of the detector (Figure 42). By using the DPMJET 3.05 event generator [48]  
 1113 and the GEANT 3.21 package [49], a sample of about 100 million p–Pb events was sim-  
 1114 ulated and reconstructed in order to compute the corrections. The distributions of  $A \times \epsilon$   
 1115 were obtained from the ratio between the number of reconstructed  $\Xi^{*0}$  and the number of  
 1116 generated particle in the same  $p_T$  and rapidity interval. Since the correction factors for  
 1117 different multiplicity classes are in agreement with those from MB events within statistical  
 1118 uncertainty, the latter were used for all multiplicity classes.

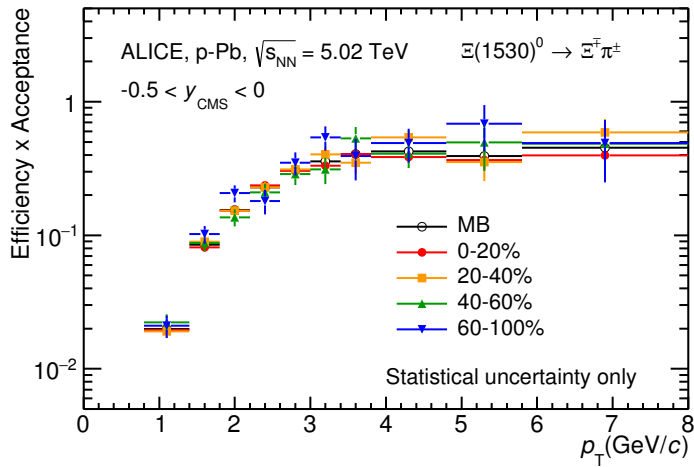


Figure 42: The geometrical acceptance and the reconstruction efficiency ( $A \times \epsilon$ ) for  $\Xi(1530)^0$  in  $-0.5 < y_{\text{CMS}} < 0$ . Only statistical uncertainties are shown.

1119 Because the generated  $\Xi(1530)^0$  spectra have different shapes than the measured  $\Xi(1530)^0$   
 1120 spectra, it is necessary to weight the generated and reconstructed  $\Xi(1530)^0$  spectra in these  
 1121 simulations. Fig. 43 shows the generated and reconstructed  $\Xi(1530)^0$  spectra plotted with  
 1122 the (corrected) measured  $\Xi(1530)^0$  spectrum for MB events and the Levy fit of that mea-  
 1123 sured spectrum. The generated and measured  $\Xi(1530)^0$  spectra have different behaviours  
 1124 for the range  $0.5 < p_T < 1$  GeV/ $c$ . The generated  $\Xi(1530)^0$  spectrum decreases with  
 1125 increasing  $p_T$  over this range, while the fit of the measured  $\Xi(1530)^0$  spectrum reaches a  
 1126 local maximum in this range. The correction  $\epsilon$  is observed to change rapidly over this  
 1127  $p_T$  range. It is therefore necessary to weight the generated spectrum so that it has the  
 1128 shape of the measured  $\Xi(1530)^0$  spectrum (and to apply corresponding weights to the re-  
 1129 constructed  $\Xi(1530)^0$  spectrum). An iterative procedure is performed to determine the  
 1130 correct weighting (and therefore the correct  $\epsilon$ ).

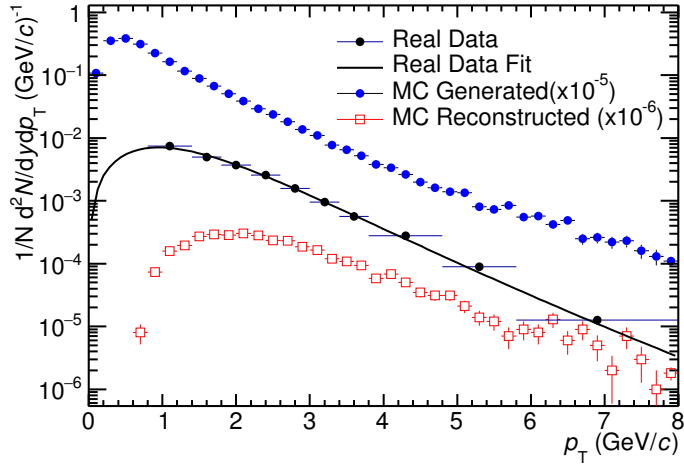


Figure 43: Real corrected  $\Xi(1530)^0$  spectrum (black) for the minimum bias with Levy fit (black curve). Also shown are the unweighted generated (blue) and reconstructed (red)  $\Xi(1530)^0$  spectra.

- 1131     1. The unweighted  $\epsilon$  is calculated.
- 1132     2. This  $\epsilon$  is used to correct the measured xis spectrum.
- 1133     3. The corrected  $\Xi(1530)^0$  spectrum is fit.
- 1134     4. This fit is used to weight the simulated xis spectra. A  $p_T$  dependent weight is applied  
1135       to the generated xis spectrum so that it follows the fit. The same weight is applied  
1136       to the reconstructed xis spectrum.
- 1137     5. The (weighted)  $\epsilon$  is calculated.
- 1138     6. Steps 2-5 are repeated (with the weighted  $\epsilon$  from step 5 used as the input for step 2)  
1139       until the  $\epsilon$  values are observed to change by < 0.1% (relative) between iterations. It  
1140       is observed that four iterations are sufficient for this procedure to converge.

1141     Finally, the re-weighted efficiency is obtained and the distribution as function of  $p_T$  is  
1142     shown in Figure 44.

1143     In order to obtain the correction factor dedicated in Pb-Pb collisions, MC events are  
1144     generated using Heavy Ion Jet Interaction Generator (HIJING). The generated events are  
1145     passed through a GEANT3 model of the ALICE experiment with a realistic description of  
1146     the detector response. Because we have observed centrality dependent efficiency, the cen-  
1147     trality dependent efficiencies have been applied to get corrected raw yield. The reweighting

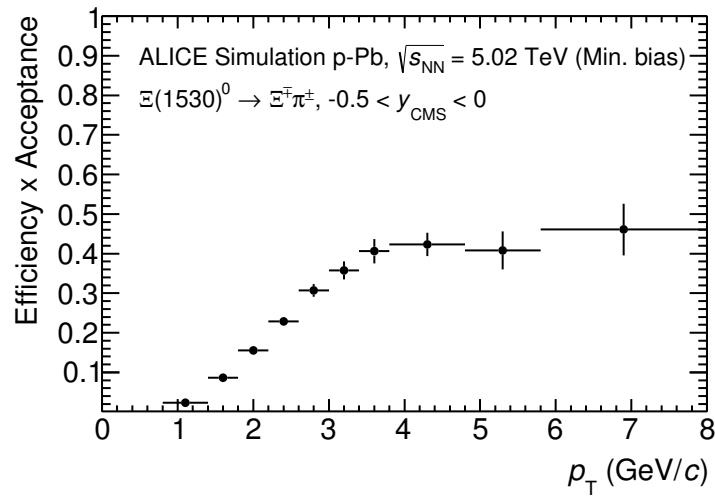


Figure 44: Efficiency as a function of  $p_T$  in minimum bias events in p–Pb collisions.

1148 approach which was used to correct the efficiency in p–Pb is also applied to the efficiency  
 1149 obtained in Pb–Pb.

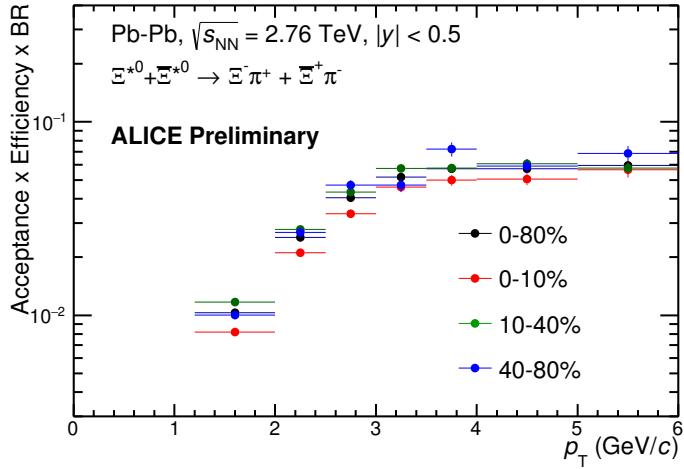


Figure 45: Efficiency as a function of  $p_T$  in different centrality classes in Pb–Pb collisions

### 1150 5.3 Corrected $p_T$ -spectra

1151 The  $p_T$  spectrum is by the number of produced particles of a given type in the desired  
 1152 interval of phase-space divided by the number of inelastic collisions. The spectrum is  
 1153 calculated as:

$$\frac{1}{N} \times \frac{d^2N}{dydp_T} = \frac{1}{N_{E,PhysSel}} \times \frac{N_{raw}}{dp_T dy} \epsilon \frac{N_{total}^{MC}}{N_{post-PVcut}^{MC}}, \quad (8)$$

1154 where  $N_E$  represent the number inelastic collisions, the  $\frac{dN}{dydp_T}$  is the yield per range of  
 1155 rapidity  $y$ , per range in  $p_T$ . On the right hand side  $N_{E,PhysSel}$  is the number of events  
 1156 counted by the physics selection trigger.  $N_{raw}$  is the raw extracted number of particle in the  
 1157 rapidity and  $p_T$  bin of width  $\Delta y = 0.5$  in p–Pb ( $\Delta y = 1.0$  in Pb–Pb) and  $\Delta p_T$ , respectively.  
 1158  $\epsilon$  is the reconstruction efficiency estimated from Monte Carlo simulations.  $\frac{N_{total}^{MC}}{N_{post-PVcut}^{MC}}$  is the  
 1159 ratio of the total number of particle from MC divided by the number of particle from MC  
 1160 after the Primary-Vertex cut is imposed. It takes into account the fraction of particle lost  
 1161 after imposing the PV cut. We notice that for minimum-bias results in p–Pb, we adopted  
 1162 a normalisation such that to provide result from non-single diffractive(NSD) cross-section.  
 1163 The normalisation factor is 0.964 [6]. The obtained spectrum at MB and the spectrums  
 1164 from different multiplicity classes in p–Pb are shown in Figure 46 and different centrality  
 1165 classes in Pb–Pb are shown in Figure 47.

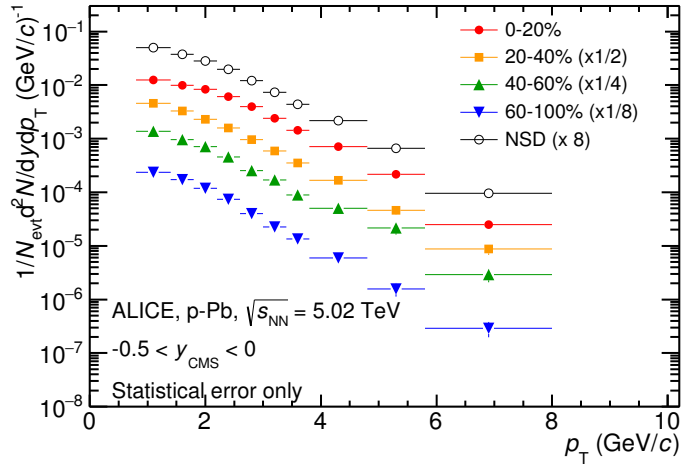


Figure 46: Corrected  $p_T$ -spectra of  $\Xi(1530)^0$  in NSD and different multiplicity classes in p-Pb collisions.

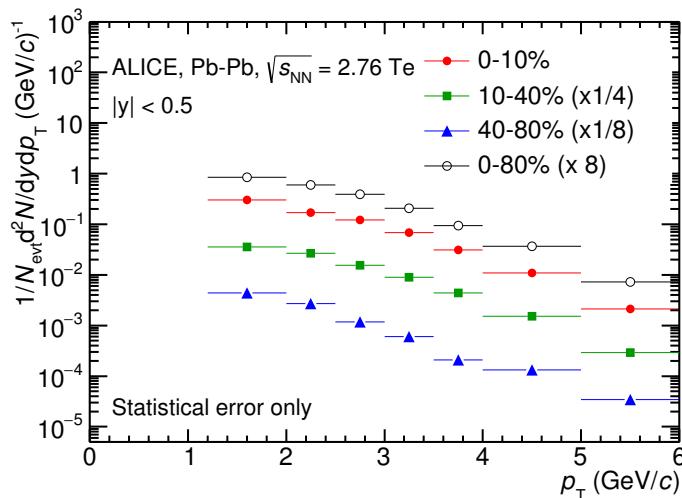


Figure 47: Corrected  $p_T$ -spectra of  $\Xi(1530)^0$  in different centrality classes in Pb-Pb collisions.

1166 **5.4 Systematic uncertainties**

1167 The systematic uncertainties are calculated in seven principle groups. The procedure to ob-  
1168 tain the systematic uncertainties is performed many times by varying the possible permuta-  
1169 tion of the analysis parameter. The general strategy for evaluating systematic uncertainties  
1170 is described as following:

- 1171 1. Choose one set of parameters for the analysis as default  
1172 2. Observe the deviation of yield when one parameter is changed  
1173 3. The systematic uncertainty is calculated for a given source as the RMS deviation of  
1174 the available sources.  
1175 4. The total systematic uncertainty, taking into account all the different sources, is the  
1176 sum in quadrature of each source.

1177 To study the systematic effect we repeat the measurement by varying one parameter at  
1178 a time. A Barlow [50] check has been performed for each measurement to verify whether it  
1179 is due to a systematic effect or a statistical fluctuation. Let each measurement be indicated  
1180 by  $(y_i \pm \sigma_i)$  and the central value (default measurement) by  $(y_c \pm \sigma_c)$ , one can define  $\Delta\sigma_i$   
1181 (Eq. 9).

$$\Delta\sigma_i = \sqrt{(|\sigma_i^2 - \sigma_c^2|)} \quad (9)$$

1182 Then we calculate  $n_i = \Delta y_i / \Delta\sigma_i$ , where  $\Delta y_i = |y_c - y_i|$ . If  $n_i \leq 1.0$  then the effects  
1183 are due to the statistical fluctuation and if  $n_i > 1.0$  we apply consistency check. Since  
1184 the alternate and default measurements are not statistically independent, an alternate  
1185 measurement which is statistically consistent with the default measurement should not be  
1186 used in calculating a systematic uncertainty. The difference between the two measurements  
1187 is  $\Delta = y_c - y_i$ . The difference in quadrature of the uncertainties is calculated by Eq. 9. It  
1188 could be possible to check if  $\Delta < \sigma$  and exclude such cases from the systematic uncertainties.  
1189 However, there can be statistical fluctuations for which  $\Delta > \sigma$ . If the variations between the  
1190 default and alternate measurements are purely statistical, the distribution of  $\Delta/\sigma$  should  
1191 be a Gaussian with a mean value that is consistent with zero and a deviation  $\sigma$  consistent  
1192 with unity. In this analysis, if the mean value is less than 0.1 and  $\sigma$  is less than 1, the  
1193 variation passes the consistency check.

1194 Only the measurements which passed the Barlow check ( $n_i > 1$ ) are used to determine  
1195 the systematic uncertainty. For measurements  $N > 2$ , the systematic uncertainty has been  
1196 determined as the RMS (eqn. 10) of the available measurements. If  $N=2$ , the absolute  
1197 difference is assigned as systematic uncertainty.

$$\delta y_{syst.} = \sqrt{\frac{1}{N} \sum_i (y_i - \bar{y})^2} \quad (10)$$

1198 Here  $N$  is the total number of available measurements including  $y_c$  and  $\bar{y}$  is the average  
1199 of value of the measurements. The measurement did not pass Barlow check, zero systematic  
1200 uncertainty has been assigned to the value.

1201 By suing the way as explained above, all the main contributions to the systematic un-  
1202 certainty of particle spectra have been studied. In particular those that comes from signal  
1203 extraction, topological and kinematical selection cuts, track quality selection and  $n\sigma$  TPC  
1204 PID variation. the meaning of each source of systematic uncertainty studied is described  
1205 in the following:

1206

### 1207     **Signal extraction**

1208 We have extracted the signal with varying the yield calculating method which contains  
1209 the method of signal extraction by integrating the Voigtian fit function and bin counting.  
1210 We also have varied the normalisation range which is related to the invariant mass region  
1211 where the mixed events distribution is scaled to subtract the combinatorial background  
1212 and different background estimator such as Like-Sign distribution and polynomial fit was  
1213 taken account into the systematic source of signal extraction. The systematic uncertainty  
1214 from signal extraction is sum in quadrature of three sources.

1215

### 1216     **Topological selection**

1217 To evaluate the stability of the chosen set of values for the topological cuts, loose and tight  
1218 cuts have beed defined in order to vary by  $\pm 10\%$  respectively. The parameters are changed  
1219 once at a time. Total systematic uncertainty from topological selection is calculated by  
1220 summation in quadrature of nine sources.

1221

### 1222     **TPC $N_{cluster}$ selection**

1223 The selection performed for the daughter tracks of the cascade is that  $N_{cluster}$  is larger  
1224 than 70 and the value has been varied to 60 and 80 in order to estimate the systematic  
1225 uncertainty due to this selection.

1226

### 1227     **TPC $dE/dx$ selection**

1228 In order to evaluate any potential effect due to the TPC  $dE/dx$  selection ( $U_{PID}$ ), the  $N_\sigma$   
1229 selection was varied with  $N = 2.5$  and  $3.5$ .

1230

### 1231      **$p_T$ shape correction**

1232 As described in Section 5.2, due to the different shape of the measured and generated  
1233  $\Xi(1530)^0$  spectra, we have applied reweighing procedure to the generated spectra to have  
1234 same shape and this correction is added into contributor of systematic uncertainty as  
1235  $p_T$  shape correction.

1236

### 1237     **Mass window range selection**

1238 In order to select  $\Xi^\pm$  which is daughter particle of  $\Xi(1530)^0$ , we apply the mass window

1239  $\pm 7$  MeV/ $c^2$  around  $\Xi(1530)^0$  mass on  $\Lambda\pi$  invariant mass distribution. The boundaries has  
1240 been varied to  $\pm 6$  MeV/ $c^2$  and  $\pm 8$  MeV/ $c^2$  to estimate systematic uncertainty.

1241

### 1242     **Vertex range selection**

1243 The distribution of vertex-z is shown in Fig.23. The cut on  $|Vz|$  was varied from the nominal  
1244  $\pm 10$ cm to  $\pm 9$ cm,  $\pm 11$ cm.

1245

### 1246     **Material Budget and hadronic cross section**

1247 A possible source of uncertainty comes from the description of the material, active (detecting area)  
1248 or dead (structure and cable), that the particles cross during their travel in the MC with respect to the real material present in the detector. Such description could  
1249 affect the reconstruction efficiency in different aspects (e.g. multiple scattering, energy  
1250 loss). The value estimated by  $\Xi$  analysis [24] has been used in this study which gives 4%  
1251 systematic uncertainty. In case of systematic uncertainty from hadronic cross section, we  
1252 have inherited the value studied in previous measurement[51] which amount is 1%.

1254

### 1255     **Tracking efficiency**

1256 Systematic uncertainties from tracking efficiency from ITS + TPC combined track were  
1257 assigned as 3% in p–Pb and 4% in Pb–Pb collision system.[51]  
1258 (<https://twiki.cern.ch/twiki/bin/view/ALICE/TrackingEfficiencyCharged>)

1259

1260 Finally, total systematic uncertainty is sum in quadrature of sources listed above. Figure  
1261 48 and Figure 49 show the total systematic uncertainty in minimum bias event and  
1262 different multiplicity classes in p–Pb collisions, respectively. Again, Figure 50 and Figure  
1263 51 present the total systematic uncertainty in minimum bias event and different centrality  
1264 classes in Pb–Pb collisions.

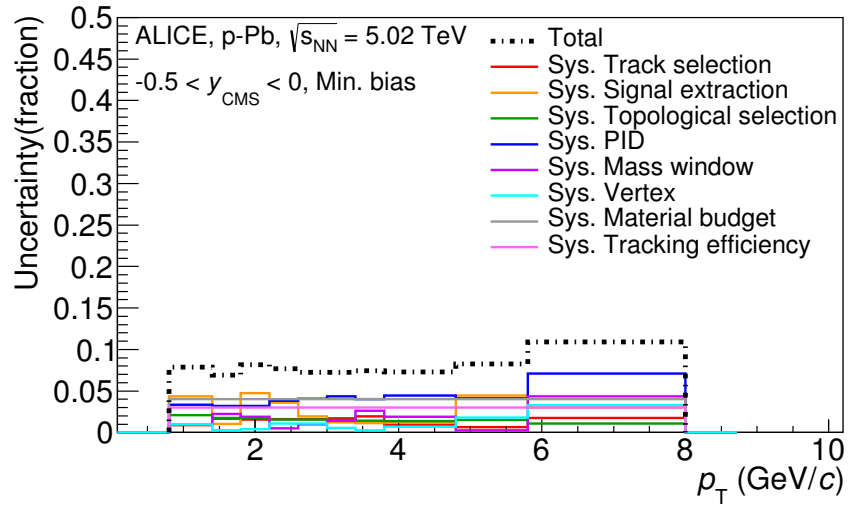


Figure 48: Summary of the contributions to the systematic uncertainty in minimum bias events in p–Pb collisions. The dashed black line is the sum in quadrature of all the contributions.

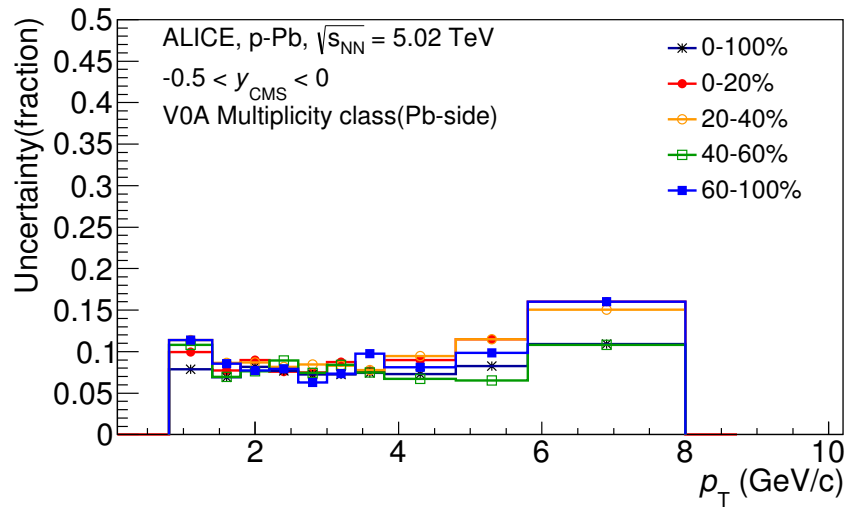


Figure 49: Systematic uncertainties for each multiplicity classes in p–Pb collisions.

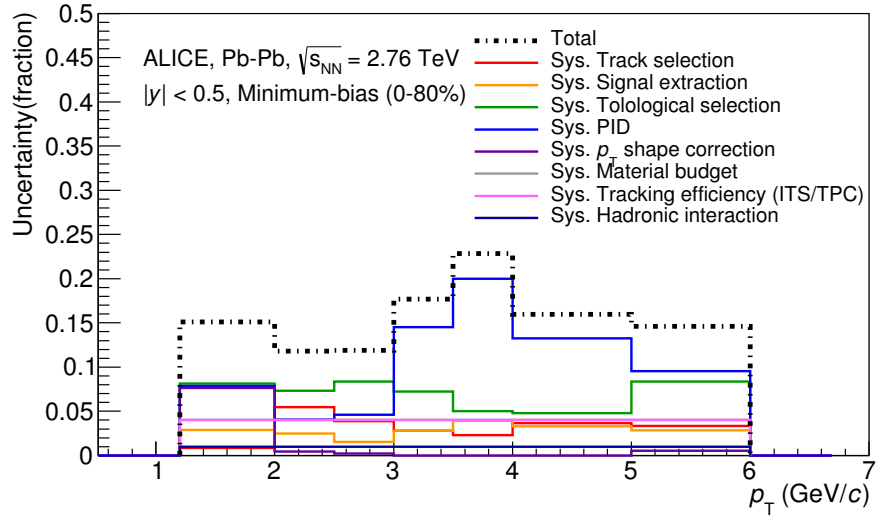


Figure 50: Summary of the contributions to the systematic uncertainty in minimum bias events in Pb–Pb collisions. The dashed black line is the sum in quadrature of all the contributions.

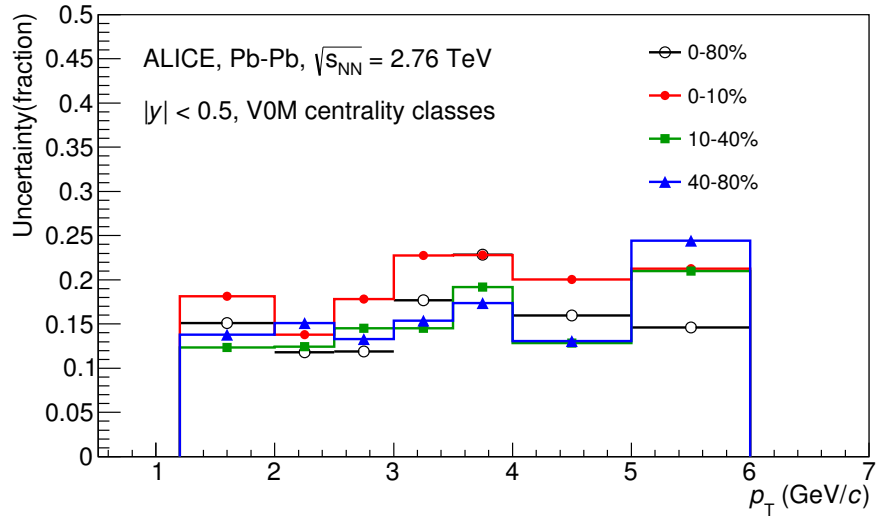


Figure 51: Systematic uncertainties for each multiplicity classes.

Source of uncertainty	p-Pb	Pb-Pb
<i>p</i> <sub>T</sub> -dependent		
Tracking efficiency	3%	4%
Tracks selection	1-2%	1-5%
Topological selection	1-2%	5-8%
PID	3-7%	4-20%
Signal extraction	1-5%	1-4%
<i>p</i> <sub>T</sub> shape correction	-	0-8%
Mass window ( $\Xi^\pm$ )	4%	-
Vertex selection	3%	-
<i>p</i> <sub>T</sub> -independent		
Hadronic interaction	-	1%
Material budget	4%	4%
Branching ratio	0.3%	0.3%
Total	8-12%	9-25 %

Table 11: Summary of the systematic uncertainties on the differential yield,  $d^2N/(dp_T dy)$ . Minimum and maximum values in all  $p_T$  intervals and multiplicity classes in p–Pb, centrality classes in Pb–Pb are shown for each source.

1265 **5.5  $\Xi(1530)^0$  transverse momentum spectra**

1266 The raw yield shown in Figure 46 and 47 have been corrected for efficiency as described  
 1267 in section 5.2. The measured spectra for  $(\Xi(1530)^0 + \bar{\Xi}(1530)^0)/2$  are reported in Figure  
 1268 52 for p–Pb collisions and Figure 53 for Pb–Pb collisions. The statistical and systematic  
 1269 uncertainties are reported respectively as the error bars and the boxes on the plot. The  
 1270 corrected yields for p–Pb collisions are measured with  $0.8 < p_T < 8.0$  GeV/c while the  
 1271 yields for Pb–Pb collisions are obtained with  $1.2 < p_T < 6.0$  GeV/c due to difficulty of  
 1272 signal extraction in low and high  $p_T$  region.

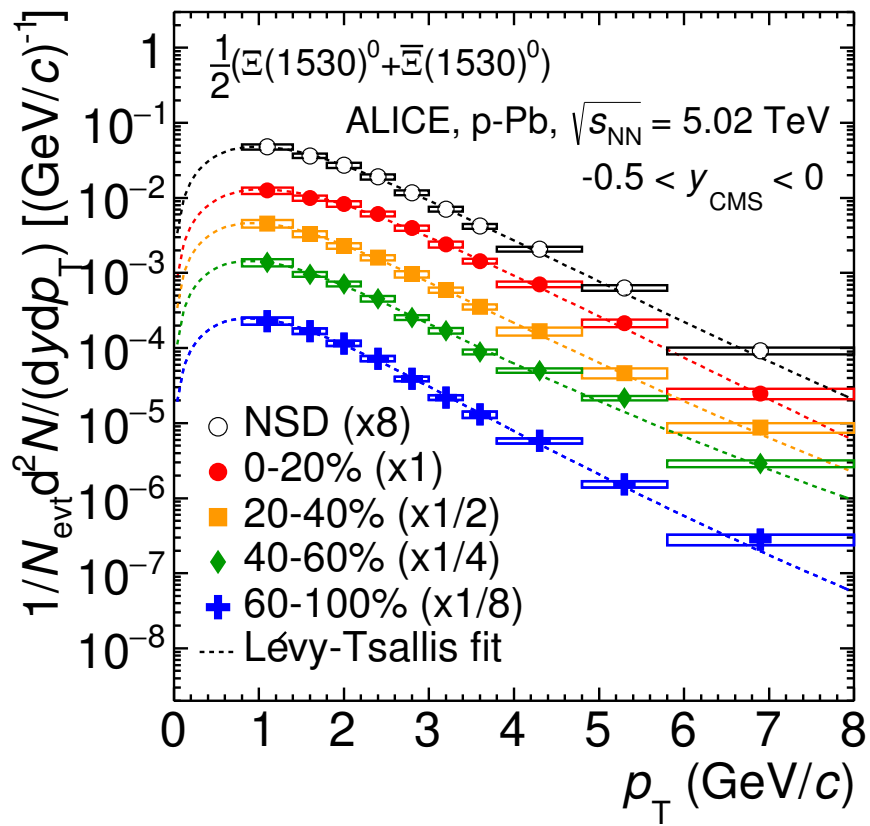


Figure 52: Corrected yields as function of  $p_T$  in NSD events and multiplicity dependent event classes in p-Pb collision system. Statistical uncertainties are presented as bar and systematical uncertainties are plotted as boxes.

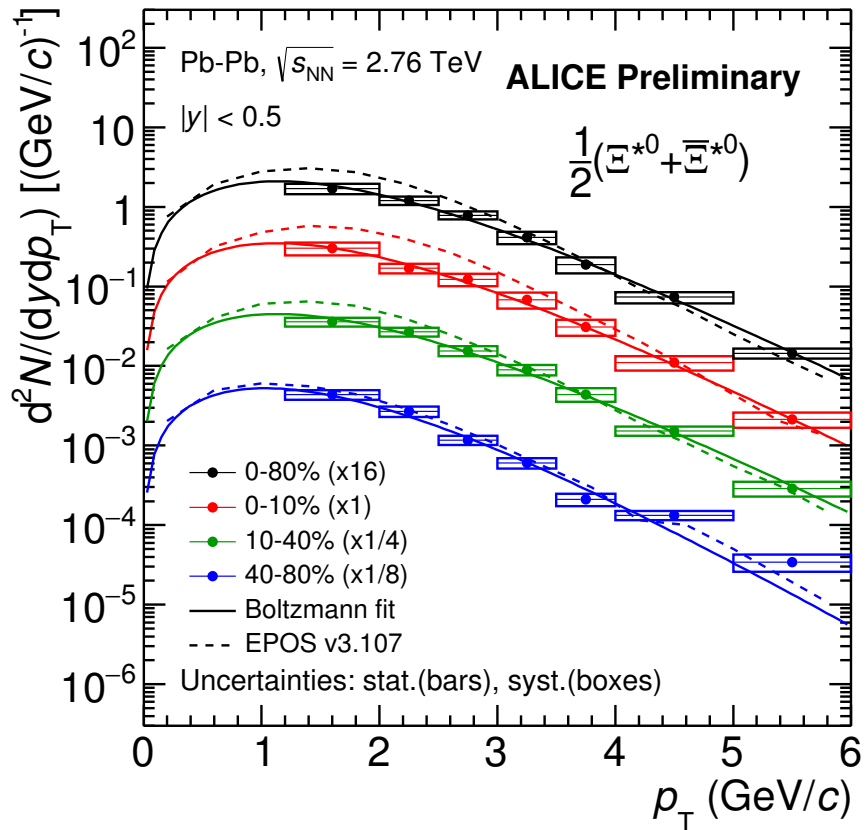


Figure 53: Corrected yields as function of  $p_T$  in different centrality classes in  $\text{Pb-Pb}$  collision system. Statistical uncertainties are presented as bar and systematical uncertainties are plotted as boxes.

## 1273 6 Further results and discussion

1274 The transverse momentum distributions of double-strange hyperon resonances,  $\Xi(1530)^0$   
1275 , produced in p–Pb collisions at  $\sqrt{s_{\text{NN}}}= 5.02$  TeV and Pb–Pb collisions at  $\sqrt{s_{\text{NN}}}= 2.76$   
1276 TeV were measured in the mid-rapidity range and they have been already presented in  
1277 Chapter 5. From the measurement, the  $\langle p_{\text{T}} \rangle$  and integrated particle yield ratios with  
1278 system size have been obtained. In the present Chapter these results are compared with  
1279 model predictions and discussed in connection with the following topics:

- 1280 • Mean transverse momentum studies
- 1281 • Study of particle production mechanism in hadronic phase
- 1282 • Study of strangeness enhancement

1283 Most of the theoretical aspects related to these topics and, in particular, the description  
1284 of the models already have been addressed in Chapter 2.

### 1285 6.1 Mean transverse momentum

1286 Figure 54 shows the mean transverse momentum  $\langle p_{\text{T}} \rangle$  as a function of mean charged-  
1287 particle multiplicity density  $\langle dN_{\text{ch}}/d\eta_{\text{lab}} \rangle$  at midrapidity. The results for  $\Xi(1530)^0$  are  
1288 compared with those for other hyperons observed in p–Pb collisions at  $\sqrt{s_{\text{NN}}}= 5.02$  TeV [5,  
1289 7].

1290 Increasing trends from low to high multiplicities are observed for all hyperons. The  
1291 mean transverse momenta increase by 20% as the mean charged-particle multiplicity in-  
1292 creases from 7.1 to 35.6. This result is similar to the one obtained for the other hyperons.  
1293 Furthermore, a similar increase has been observed also for  $K^{\pm}$ ,  $K_S^0$ ,  $K^*(892)^0$  and  $\phi$  [6],  
1294 whereas protons are subject to a larger ( $\sim 33\%$ ) increase in the given multiplicity range,  
1295 as discussed also in Ref. [5].

1296 In all multiplicity classes, the  $\langle p_{\text{T}} \rangle$  follows an approximate mass ordering:

- 1297 •  $\langle p_{\text{T}} \rangle_{\Lambda} < \langle p_{\text{T}} \rangle_{\Xi^-} \simeq \langle p_{\text{T}} \rangle_{\Sigma^{*\pm}} < \langle p_{\text{T}} \rangle_{\Xi^{*0}} < \langle p_{\text{T}} \rangle_{\Omega^-}$

1298 The  $\langle p_{\text{T}} \rangle$  of  $\Sigma^{*\pm}$  looks systematically lower than the  $\langle p_{\text{T}} \rangle$  of  $\Xi^-$ , despite the larger mass  
1299 of  $\Sigma^{*\pm}$ . The uncertainties, however, are too large to draw any conclusion on possible hints  
1300 of violation of the mass hierarchy. This hierarchy of mass-ordering, also including  $D^0$  and  
1301  $J/\psi$  in the comparison, is displayed in Figure 55. Note, however, that the  $D^0$  and  $J/\psi$   
1302 were measured in different rapidity ranges:  $|y_{\text{CMS}}| < 0.5$  [9] ( $|y_{\text{CMS}}| < 0.9$  [10]) for  $D^0$   
1303 ( $J/\psi$ ) in pp and  $-0.96 < y_{\text{CMS}} < 0.04$  [9] ( $-1.37 < y_{\text{CMS}} < 0.43$  [11]) for  $D^0$  ( $J/\psi$ ) in  
1304 p–Pb, and the results for  $D^0$  and  $J/\psi$  in p–Pb collisions are for the 0–100% multiplicity  
1305 class. This mass dependence is observed in both p–Pb and pp collisions. It was observed  
1306 also by the STAR collaboration [52] in MB pp, MB d–Au and central Au–Au collisions.

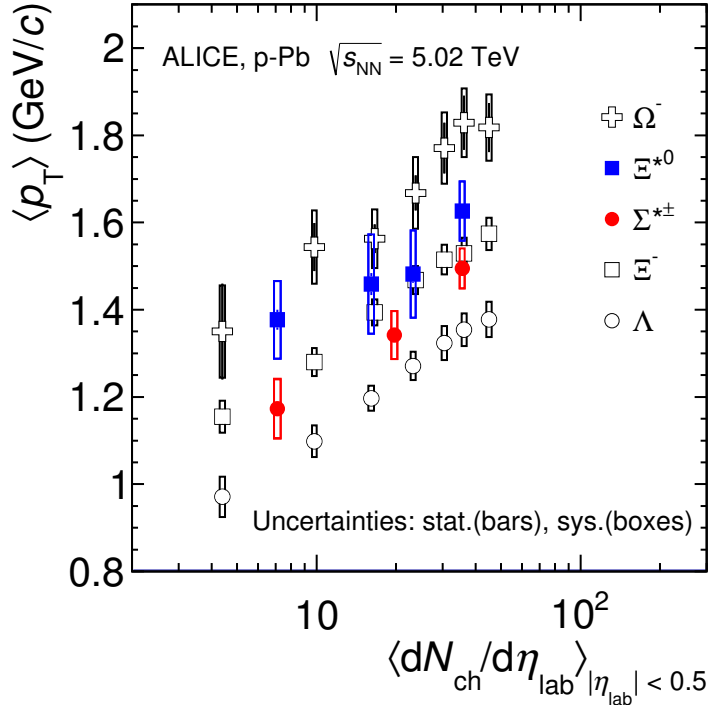


Figure 54: Mean transverse momenta  $\langle p_T \rangle$  of  $\Lambda$ ,  $\Xi^-$ ,  $\Sigma^{*\pm}$ ,  $\Xi^{*0}$  and  $\Omega^-$  in p–Pb collisions at  $\sqrt{s_{NN}}=5.02$  TeV as a function of mean charged-particle multiplicity density  $\langle dN_{ch}/d\eta_{lab} \rangle$ , measured in the pseudorapidity range  $|\eta_{lab}| < 0.5$ . The results for  $\Lambda$ ,  $\Xi^-$  and  $\Omega^-$  are taken from [5, 6, 7]. Statistical and systematic uncertainties are represented as bars and boxes, respectively. The  $\Omega^-$  and  $\Xi^-$  points in the 3rd and 4th lowest multiplicity bins are slightly displaced along the abscissa to avoid superposition with the  $\Xi(1530)^0$  points.

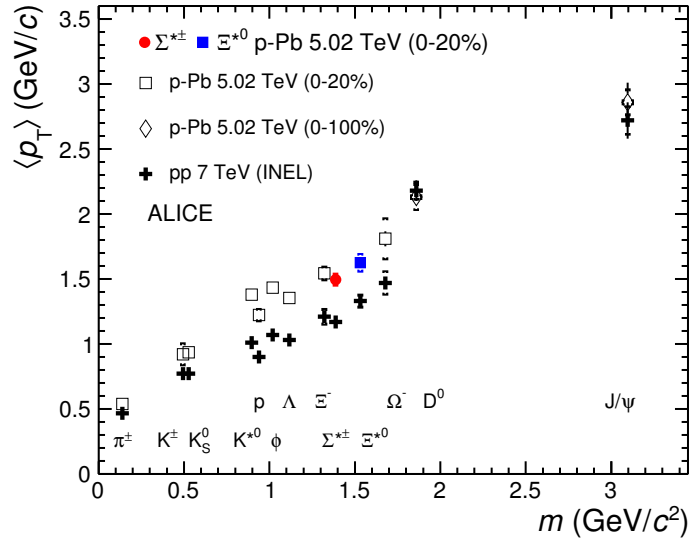


Figure 55: Mass dependence of the mean transverse momenta of identified particles for the 0 – 20% V0A multiplicity class and with  $-0.5 < |y_{\text{CMS}}| < 0$  in p–Pb collisions at  $\sqrt{s_{\text{NN}}} = 5.02$  TeV [5, 7], and in minimum-bias pp collisions at  $\sqrt{s} = 7$  TeV [8] with  $|y_{\text{CMS}}| < 0.5$ . Additionally,  $D^0$  and  $J/\psi$  results are plotted. The  $D^0$  and  $J/\psi$  were measured in different rapidity ranges:  $|y_{\text{CMS}}| < 0.5$  [9] ( $|y_{\text{CMS}}| < 0.9$  [10]) for  $D^0$  ( $J/\psi$ ) in pp and  $-0.96 < y_{\text{CMS}} < 0.04$  [9] ( $-1.37 < y_{\text{CMS}} < 0.43$  [11]) for  $D^0$  ( $J/\psi$ ) in p–Pb. Note also that the results for  $D^0$  and  $J/\psi$  in p–Pb collisions are for the 0-100% multiplicity class.

1307 Furthermore, for the light-flavour hadrons, the mean transverse momenta in p–Pb col-  
1308 lisions are observed to be consistently higher than those in pp collisions at 7 TeV. The  
1309 situation for the charm hadrons is different, where  $\langle p_T \rangle$  appears compatible between both  
1310 colliding systems. The discrepancy is likely due to different production mechanisms for  
1311 heavy and light flavours and to a harder fragmentation of charm quarks. Specifically, the  
1312 fact that  $\langle p_T \rangle$  remains similar in pp and in p–Pb is consistent with an  $R_{p\text{Pb}}$  ratio com-  
1313 patible with unity at all  $p_T$ [9] for  $D^0$ , and/or with the effects of shadowing in p–Pb which  
1314 reduces the production at low  $p_T$  and thus increasing the overall  $\langle p_T \rangle$  for  $J/\psi$  [11]; the  
1315 small  $p_T$ hardening expected in pp when going from 5.02 to 7TeV is apparently not enough  
1316 to counter-balance the situation.

1317 Because of small decrease of the  $\langle p_T \rangle$  for proton and  $\Lambda$  relative to those for  $K^{*0}$  and  
1318  $\phi$ , two different trends for mesons and baryons have been suggested [53]. Even including  
1319  $D^0$  and  $J/\psi$ , as shown in Figure 55, a different trend for mesons and baryons cannot be  
1320 convincingly established.

1321 **6.2 Particle yield ratios**

1322 **6.2.1 Integrated yield ratios of excited to ground-state hadrons**

1323 The integrated yield ratios of excited to ground-state hyperons [54, 5, 8, 7] with the same  
1324 strangeness content, for different collision systems and energies, are shown in Figure 56  
1325 as a function of system size. The ratio of  $\Xi(1530)^0$  to  $\Xi$  is flat across the system and  
1326 it complements the information derived from other resonance measurement for different  
1327 lifetime which are shown in Figure 57.

1328 The short-lived resonances( $\rho$ ,  $K^*$  and  $\Lambda^*$ ) which exhibit suppression from peripheral to  
1329 central lead-lead collisions and with respect to thermal model in central lead-lead collisions.  
1330 Currently favored explanation of is dominance of elastic re-scattering of decay daughters  
1331 over regeneration in the hadronic phase.

1332 The constant behavior of the yield ratios of excited to ground-state hyperons with same  
1333 strangeness content ( $\Xi(1530)^0$  and  $\Phi$ ) indicates that neither regeneration nor re-scattering  
1334 dominates with increasing collision system size because of its longer-lifetime.

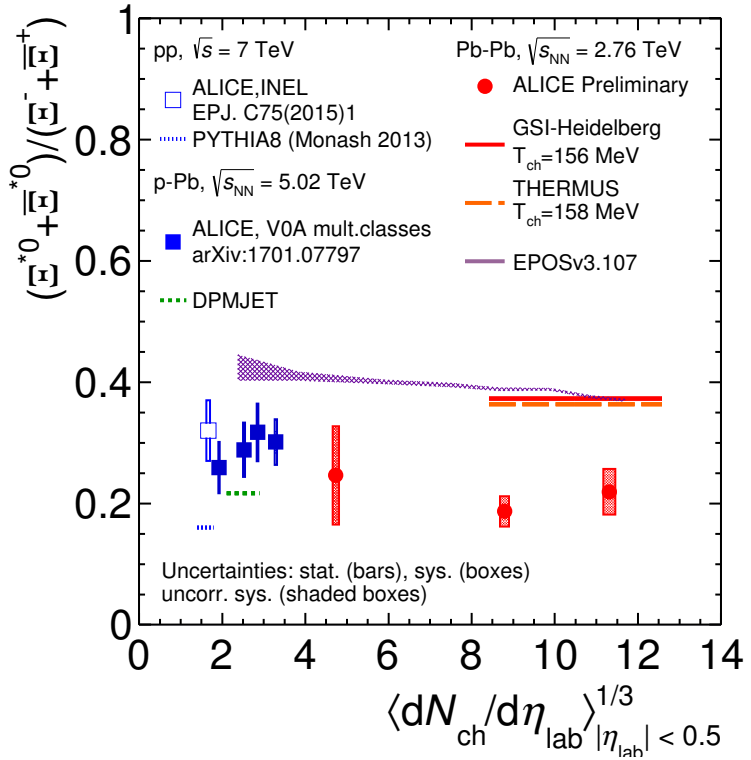


Figure 56: Ratio of  $\Xi(1530)^0$  to  $\Xi^-$  measured in pp [8], p–Pb [5, 7] and Pb–Pb collisions as a function of  $\langle dN_{ch}/d\eta_{lab} \rangle$  measured at midrapidity. Statistical uncertainties (bars) are shown as well as total systematic uncertainties (hollow boxes) and systematic uncertainties uncorrelated across multiplicity (shaded boxes). A few model predictions are also shown as lines at their appropriate abscissa.

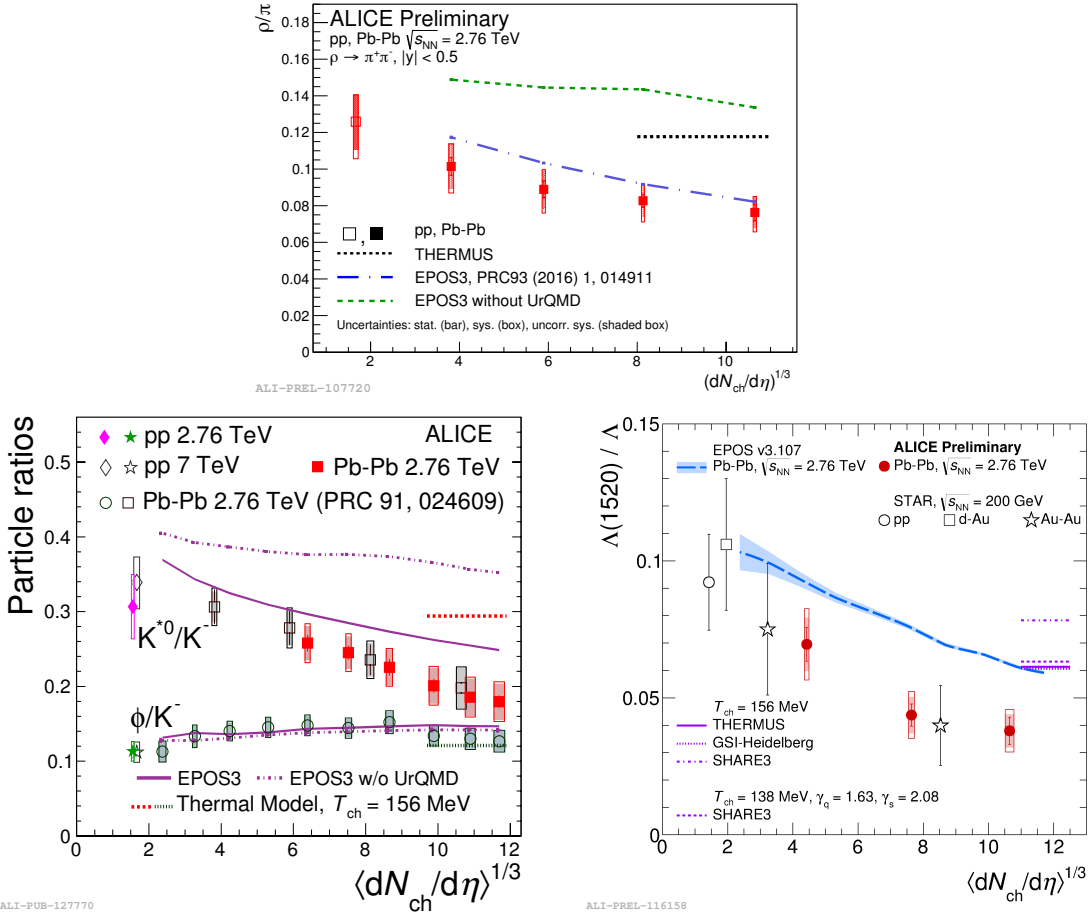


Figure 57: Ratio of  $\rho/\pi$ (Up),  $K^*/K$ ,  $\phi/K$ (Left bottom) and  $\Lambda^*/\Lambda$  with system size measured at mid-rapidity. Statistical uncertainties (bars) are shown as well as total systematic uncertainties (hollow boxes) and systematic uncertainties uncorrelated across multiplicity (shaded boxes). A few model predictions are also shown as lines at their appropriate abscissa.

1335 **6.3 Integrated yield ratios to pion**

1336 The integrated yield ratios of excited hyperons to pions are shown in Figure 58 to study  
1337 the evolution of relative strangeness production yields with increasing collision system  
1338 size. The ratio of  $\Xi(1530)^0$  to  $\Xi$  is observed to be increase from pp to p–Pb collisions  
1339 system and then, decrease from peripheral to central Pb–Pb collision. The QCD-inspired  
1340 predictions like PYTHIA for pp [55] and DPMJET for p–Pb [48] clearly underestimate  
1341 the observed yield ratios, while the statistical one seems to be comparable with results  
1342 from high multiplicity in p–Pb but the ratio in Pb–Pb is below with respect to the model.  
1343 The results in pp and p–Pb collisions are consistent with previous observation of ground-  
1344 state hyperons to pion ratios. The Figure 59 presents particle yield ratios to pions of  
1345 strange and multi-strange hadrons normalized to the values measured in pp collisions. As  
1346 shown in the Figure 59, the  $\Xi(1530)^0$  to pion ratios follow the trend of  $\Xi \pi$  as function of  
1347  $\langle dN_{ch}/d\eta_{lab} \rangle$  and indicate that the strangeness enhancement observed in p–Pb collisions  
1348 depends predominantly on the strangeness content, rather than on the hyperon mass.

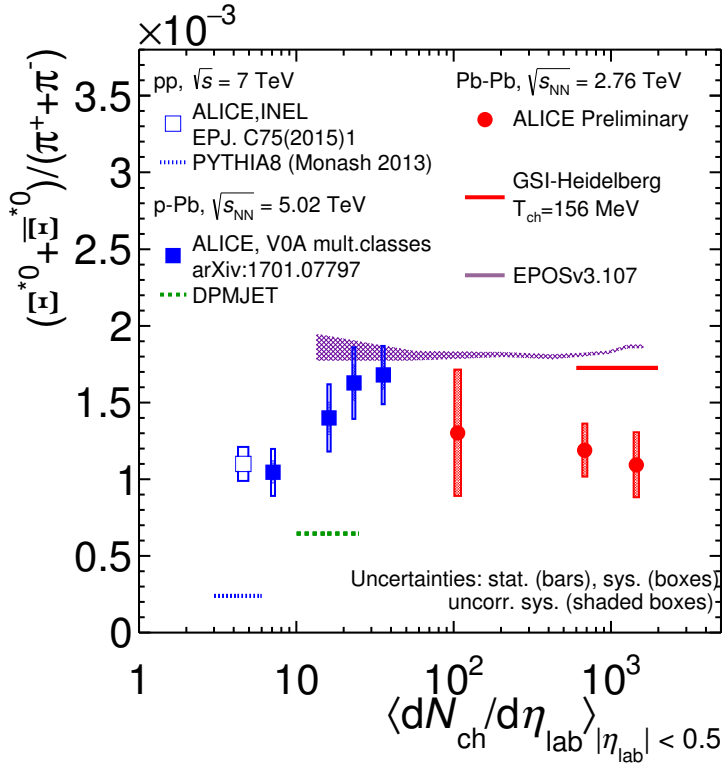


Figure 58: Ratio of  $\Xi(1530)^0$  to  $\pi^\pm$ , measured in pp [12] and p–Pb [8] collisions, as a function of the average charged particle density ( $\langle dN_{ch}/d\eta_{lab} \rangle$ ) measured at mid-rapidity. Statistical uncertainties (bars) are shown as well as total systematic uncertainties (hollow boxes) and systematic uncertainties uncorrelated across multiplicity (shaded boxes). A few model predictions are also shown as lines at their appropriate abscissa.

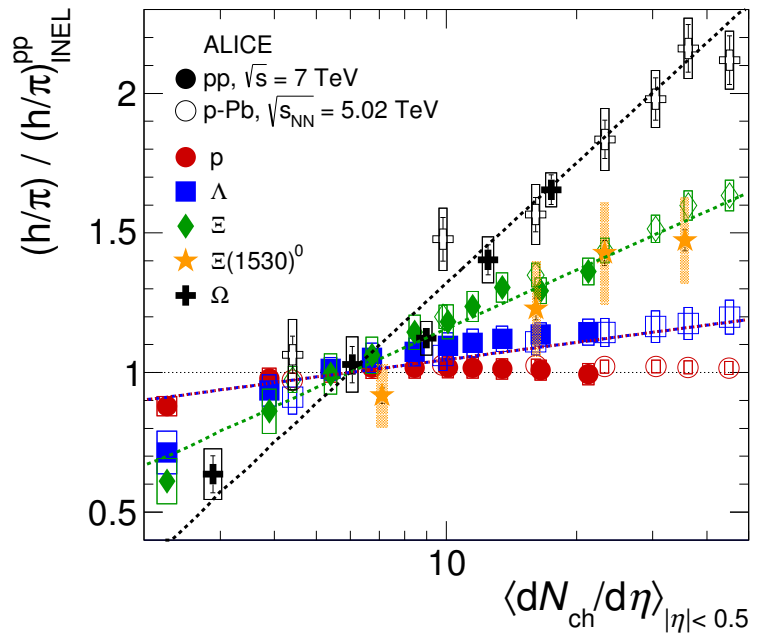


Figure 59: Particle yield ratios to pions of strange and multi-strange hadrons normalized to the values measured in pp collisions, both in pp and in p–Pb collisions. The common systematic uncertainties cancel in the double-ratio. The empty boxes represent the remaining uncorrelated uncertainties.

1349 **References**

- 1350 [1] **Particle Data Group** Collaboration, K. Olive *et al.*, “Review of Particle Physics,”  
1351 *Chin. Phys. C* **38** (2014) 090001.
- 1352 [2] K. R. Ahmed Tounsi, “Strangeness Enhancement and Canonical Suppression,” *High*  
1353 *Energy Physis A* **681** (2001) 119–123.
- 1354 [3] “TE-EPC-LPC LHC units,”.  
1355 <http://te-epc-lpc.web.cern.ch/te-epc-lpc/machines/lhc/general.stm>.
- 1356 [4] **ALICE** Collaboration, K. e. a. Aamodt, “Alignment of the ALICE Inner Tracking  
1357 System with cosmic-ray tracks,” *JINST* **5** (2010) P03003.
- 1358 [5] **ALICE** Collaboration, J. Adam *et al.*, “Multiplicity dependence of pion, kaon,  
1359 proton and lambda production in p–Pb collisions at  $\sqrt{s_{NN}} = 5.02$  TeV,” *Phys. Lett.*  
1360 **B728** (2014) 25–38, [arXiv:1307.6796 \[nucl-ex\]](https://arxiv.org/abs/1307.6796).
- 1361 [6] **ALICE** Collaboration, J. Adam *et al.*, “Production of  $K^*(892)^0$  and  $\phi(1020)$  in  
1362 p–Pb collisions at  $\sqrt{s_{NN}} = 5.02$  TeV,” *Eur. Phys. J.* **C76** (2016) 245,  
1363 [arXiv:1601.7868 \[nucl-ex\]](https://arxiv.org/abs/1601.7868).
- 1364 [7] **ALICE** Collaboration, J. Adam *et al.*, “Multi-strange baryon production in p–Pb  
1365 collisions at  $\sqrt{s_{NN}} = 5.02$  TeV,” *Phys. Lett.* **B758** (2016) 389–401,  
1366 [arXiv:1512.07227 \[nucl-ex\]](https://arxiv.org/abs/1512.07227).
- 1367 [8] **ALICE** Collaboration, B. Abelev *et al.*, “Production of  $\Sigma(1385)^{\pm}$  and  $\Xi(1530)^0$  in  
1368 proton-proton collisions at  $\sqrt{s} = 7$  TeV,” *Eur. Phys. J.* **C75** (2015) 1,  
1369 [arXiv:1406.3206 \[nucl-ex\]](https://arxiv.org/abs/1406.3206).
- 1370 [9] **ALICE** Collaboration, J. Adam *et al.*, “ $D$ -meson production in p–Pb collisions at  
1371  $\sqrt{s_{NN}} = 5.02$  TeV and in pp collisions at  $\sqrt{s} = 7$  TeV,” *Phys. Rev. C* **94** (2016)  
1372 054908, [arXiv:1605.07569 \[nucl-ex\]](https://arxiv.org/abs/1605.07569).
- 1373 [10] **ALICE** Collaboration, B. Abelev *et al.*, “Inclusive  $J/\psi$  production in pp collisions  
1374 at  $\sqrt{s} = 2.76$  TeV,” *Phys. Lett.* **B718** (2012) 295–306, [arXiv:1203.3641 \[hep-ex\]](https://arxiv.org/abs/1203.3641).
- 1375 [11] **ALICE** Collaboration, J. Adam *et al.*, “Rapidity and transverse-momentum  
1376 dependence of the inclusive  $J/\psi$  nuclear modification factor in p–Pb collisions at  
1377  $\sqrt{s_{NN}} = 5.02$  TeV,” *JHEP* **06** (2015) 55, [arXiv:1503.07179 \[nucl-ex\]](https://arxiv.org/abs/1503.07179).
- 1378 [12] **ALICE** Collaboration, J. Adam *et al.*, “Measurement of pion, kaon and proton  
1379 production in proton-proton collisions at  $\sqrt{s} = 7$  TeV,” *Eur. Phys. J.* **C75** (2015)  
1380 226, [arXiv:1504.00024 \[nucl-ex\]](https://arxiv.org/abs/1504.00024).

- 1381 [13] F. Halzen and A. Martin, “Quarks and Leptons: an introductory course in modern  
 1382 particle physics,” *By John Wiley and Sons* (1984) .
- 1383 [14] T. K. Nayak, “Heavy Ions: Results from the Large Hadron Collider,” *Pramana* **79**  
 1384 (2012) 719–735.
- 1385 [15] S. Wheaton, J. Cleymans, and M. Hauer, “THERMUS: A Thermal model package  
 1386 for ROOT,” *Comput. Phys. Commun.* **180** (2009) 84–106, [arXiv:hep-ph/0407174](#)  
 1387 [hep-ph].
- 1388 [16] S. O. T. P. K. W. H.J. Drescher, M. Hladik, “Parton-Based Gribov-Regge Theory,”  
 1389 *Phys. Rept.* **350** (2001) 93–289, [hep-ph/0007198](#).
- 1390 [17] T. P. M. B. K. M. K. Werner, Iu. Karpenko, “Event-by-event simulation of the  
 1391 three-dimensional hydrodynamic evolution from flux tube initial conditions in  
 1392 ultrarelativistic heavy ion collisions,” *Phys. Rev.* **C82** (2010) 044904.
- 1393 [18] I. K. T. P. K. Werner, B. Guiot, “Analyzing radial flow features in p-Pb and p-p  
 1394 collisions at several TeV by studying identified-particle production with the event  
 1395 generator EPOS3,” *Phys. Rev.* **C89** (2014) 064903.
- 1396 [19] K. Werner., “Analyzing radial flow features in p-Pb and p-p collisions at several TeV  
 1397 by studying identified-particle production with the event generator EPOS3,” *Phys.  
 1398 Rev. Lett.* **98** (2007) 152301.
- 1399 [20] S. B. et al., “Microscopic Models for Ultrarelativistic Heavy Ion Collisions,” *Prog.  
 1400 Part. Nucl. Phys.* **41** (1998) 255.
- 1401 [21] M. B. et al., “Relativistic Hadron-Hadron Collisions in the Ultra-Relativistic  
 1402 Quantum Molecular Dynamics Model,” *J. Phys.* **G25** (1999) 1859–1896.
- 1403 [22] M. Gell-Mann and Y. Ne’eman, “The Eightfold Way,” *By W.A. Benjamin* (1964) .
- 1404 [23] J. Rafelski and B. Mller, “Strangeness Production in the Quark-Gluon Plasma,”  
 1405 *Phys. Rev. Lett* **48** (1982) 1066–1069.
- 1406 [24] **ALICE** Collaboration, B. Abelev *et al.*, “Multi-strange baryon production at  
 1407 mid-rapidity in Pb–Pb collisions at  $\sqrt{s_{\text{NN}}} = 2.76$  TeV,” *Phys. Lett.* **B728** (2014)  
 1408 216–227, [arXiv:1307.5543](#) [nucl-ex].
- 1409 [25] P. Braun-Munziger, “Chemical equilibration and the Hadron-QGP phase  
 1410 transition.”
- 1411 [26] **ALICE** Collaboration, B. Abelev *et al.*, “Performance of the ALICE Experiment at  
 1412 the CERN LHC,” *Int. J. Mod. Phys.* **A29** (2014) 1430044, [arXiv:1402.4476](#)  
 1413 [nucl-ex].

- 1414 [27] L. Evans and P. Bryant, “LHC Machine,” *JINST* **3** (2008) S08001.
- 1415 [28] C. S. I. Service, “LHC Design Report Volume I+II+III,” *In*  
1416 *CERN-2004-003-V1(-V2)(-V3)* (2004) .
- 1417 [29] “ALICE Technical Proposal,” *In CERN-LHCC-95-71* (1995) .
- 1418 [30] “ATLAS Technical Proposal,” *In CERN-LHCC-94-43* (1994) .
- 1419 [31] “CMS Technical Proposal,” *In CERN-LHCC-94-38* (1994) .
- 1420 [32] “LHCb Technical Proposal,” *In CERN-LHCC-98-004* (1998) .
- 1421 [33] “Total Cross Section, Elastic Scattering and Diffraction Dissociation at the LHC,”  
1422 *In CERN-LHCC-99-007* (1999) .
- 1423 [34] **ALICE** Collaboration, K. Aamodt *et al.*, “The ALICE experiment at the CERN  
1424 LHC,” *JINST* **3** (2008) S08002.
- 1425 [35] **ALICE** Collaboration, L. B. et al, “Definition of the ALICE coordinate system and  
1426 basic rules for sub-detector components numbering,” *In Internal Note*  
1427 *ALICE-INT-2003-038* (2003) .
- 1428 [36] **ALICE** Collaboration, J. e. a. Alme, “The ALICE TPC, a large 3-dimensional  
1429 tracking device with fast readout for ultra-high multiplicity events,” *In Nuclear*  
1430 *Instruments and Method in Physics Research* **A622** (2010) 316–367.
- 1431 [37] “Technical Design Report on Forward Detectors: FMD, T0 and VZERO,” *In*  
1432 *CERN-LHCC-2004-025* (2004) .
- 1433 [38] R. Glauber, “Lectures in Theoretical Physics,” *By Interscience Publishers.* **1** (1959)  
1434 315.
- 1435 [39] A. S. K.C. Chung, C.S. Whang and G. Pech, “Transverse and forward energy  
1436 distributions in untra-relativistic heavy-ion collisions by an absorption model,”  
1437 *Physics Review* **C57** (1998) 847–856.
- 1438 [40] **ALICE** Collaboration, J. Adam *et al.*, “Centrality dependence of particle  
1439 production in p–Pb collisions at  $\sqrt{s_{\text{NN}}}= 5.02 \text{ TeV}$ ,” *Phys. Rev.* **C91** (2015) 064905,  
1440 [arXiv:1412.6828 \[nucl-ex\]](https://arxiv.org/abs/1412.6828).
- 1441 [41] **ALICE** Collaboration, B. Abelev *et al.*, “Centrality determination of Pb–Pb  
1442 collisions at  $\sqrt{s_{\text{NN}}}= 2.76 \text{ TeV}$  with ALICE,” *Phys. Rev.* **C88** (2013) ,  
1443 [arXiv:1303.0737 \[nucl-ex\]](https://arxiv.org/abs/1303.0737).
- 1444 [42] “ALICE Technical Design Report of the Trigger, Data Acquisition, High-Level  
1445 Trigger, Control system,” *In CERN-LHCC-2003-062.* (2003) .

- 1446 [43] “The Grid - Blueprint for a New Computing Infrastructure,” *By Morgan Kaufmann*  
 1447 *Publishers.* (1999) .
- 1448 [44] e. a. Bagnasco. S, “AliEn: ALICE Environment on the GRID,” *In Jounal of Physics: Conference Series* **119** (2008) n.062012.
- 1450 [45] R. Brun and F. Rademakers, “ROOT - An object oriented data analysis framework,”  
 1451 *In Nuclear Instrument and Methods in Physics Research Section A* **389** (1997)  
 1452 81–86.
- 1453 [46] **ALICE** Collaboration, B. Abelev *et al.*, “Pseudorapidity Density of Charged  
 1454 Particles in p–Pb Collisions at  $\sqrt{s_{\text{NN}}}= 5.02$  TeV,” *Phys. Rev. Lett.* **110** (2013)  
 1455 032301, [arXiv:1210.3615 \[nucl-ex\]](#).
- 1456 [47] **ALICE** Collaboration, K. Aamodt *et al.*, “Strange particle production in  
 1457 proton-proton collisions at  $\sqrt{s}= 0.9$  TeV with ALICE at the LHC,” *Eur. Phys. J.*  
 1458 **C71** (2011) 1594, [arXiv:1012.3257 \[nucl-ex\]](#).
- 1459 [48] S. Roesler, R. Engel, , and J. Ranft, “The Monte Carlo Event Generator  
 1460 DPMJET-III, Advanced Monte Carlo for Radiation Physics, Particle Transport  
 1461 Simulation and Applications,” *Conference Proceedings, MC2000, Lisbon, Portugal,*  
 1462 *October 23-26* (2000) 1033–1038, [hep-ph/0012252](#).
- 1463 [49] R. Brun, F. Carminati, and S. Giani, “GEANT detector description and simulation  
 1464 tool,” *CERN-W5013* (1994) .
- 1465 [50] R. Barlow, “Systematic Errors: Facts and Fictions,” *Presented at Advanced  
 1466 Statistical Techniques in HEP, Durham, March 2002* (2002) 333p,  
 1467 [hep-ex/0207026v1](#).
- 1468 [51] **ALICE** Collaboration, B. Abelev *et al.*, “Centrality dependence of  $\pi$ ,  $K$  and  $p$   
 1469 production in Pb–Pb collisions at  $\sqrt{s_{\text{NN}}}= 2.76$  TeV,” *Phys. Rev.* **C88** (2013) ,  
 1470 [arXiv:1301.4361 \[nucl-ex\]](#).
- 1471 [52] **STAR** Collaboration, B. I. Abelev *et al.*, “Hadronic resonance production in d–Au  
 1472 collisions at  $\sqrt{s_{\text{NN}}}= 200$  GeV measured at the BNL Relativistic Heavy-Ion Collider,”  
 1473 *Phys. Rev.* **C78** (2008) 044906, [arXiv:0801.0450 \[nucl-ex\]](#).
- 1474 [53] A. Velásquez, “Mean  $p_{\text{T}}$  scaling with  $m/n_q$  at the LHC: Absence of (hydro) flow in  
 1475 small systems?,” *Nucl. Phys.* **A943** (2015) 9–17, [arXiv:1506.00584 \[hep-ph\]](#).
- 1476 [54] **ALICE** Collaboration, B. Abelev *et al.*, “Multi-strange baryon production in pp  
 1477 collisions at  $\sqrt{s}= 7$  TeV with ALICE,” *Phys. Lett.* **B712** (2012) 309,  
 1478 [arXiv:1204.0282 \[nucl-ex\]](#).

- 1479 [55] T. Sjöstrand, S. Mrenna, and P. Skands, “A brief introduction to PYTHIA 8.1,”  
1480 *Comput. Phys. Comm.* **178** (2008) 852–867, arXiv:0710.3820 [hep-ph].

1481 **Acknowledgements**